PULSED PHOTOACOUSTIC TECHNIQUES AND GLUCOSE DETERMINATION IN HUMAN BLOOD AND TISSUE

ZUOMIN ZHAO

Department of Electrical Engineering and
Infotech Oulu,
University of Oulu

ZUOMIN ZHAO

PULSED PHOTOACOUSTIC TECHNIQUES AND GLUCOSE DETERMINATION IN HUMAN BLOOD AND TISSUE

Zhao, Zuomin, Pulsed photoacoustic techniques and glucose determination in human blood and tissue

Department of Electrical Engineering and Infotech Oulu, University of Oulu, P.O.Box 4500, FIN-90014 University of Oulu, Finland

Oulu, Finland

2002

Abstract

Determination of blood glucose level is a frequently occurring procedure in diabetes care. As the most common method involves collecting blood drops for chemical analysis, it is invasive and liable to afflict a degree of pain and cause a skin injury. To eliminate these disadvantages, this thesis focuses on pulsed photoacoustic techniques, which have potential ability in non-invasive blood glucose measurement.

The fundamental theory of photoacoustics in liquid and soft tissue was studied systematically. The distributions of photoacoustic sources in a near-infrared optical skin model were simulated by the Monte Carlo method. Expansion coefficient and specific heat of glucose solution were measured by thermodynamic method, while the sound velocity in it was determined by photoacoustic approach. The effect of glucose on blood optical scattering was studied by a picosecond pulsed laser together with a streak camera. A photoacoustic apparatus comprising a pulsed laser diode and a piezoelectric transducer was built and applied to measure glucose concentration in water and scattering media. Moreover, this apparatus was also used to non-invasive experiment on human fingers.

The measurements showed that the expansion coefficient, specific heat and acoustic velocity change by 1.2%, -0.6% and 0.28%, respectively, in response to a 1% change in glucose concentration. The sum effect of these parameters to photoacoustic signal was much larger than that of optical absorption of glucose in near infrared wavelengths, which provided photoacoustic technique a higher degree of sensitivity than offered by the optical absorption method. At the wavelength of 905 nm, the measured glucose detection sensitivity in a 3% milk solution, a tissue sample and whole human blood was 5.4%, 2.5% and 14%, respectively. Each figure is higher than that of glucose in water, about 2%, for a one percent change in glucose concentration. This was supported by the temporal dispersion curves of glucose in blood samples, which demonstrated that glucose decreased the optical scattering of tissues. The currently photoacoustic apparatus could detect the minimal glucose concentration of 100 mg/dl in whole blood samples. It is sensitive to physiological changes in non-invasive measurement, but insufficient for evaluating change in the physiological glucose concentration.

Current photoacoustic techniques have apparently advantages in study of scattering media and made great progress in tissue imaging and diagnosis. However, in non-invasive blood glucose measurement they met similar problems as optical approaches based on scattering effect.

Keywords: photoacoustic measurement, glucose determination, tissue optics, acoustic detection

Acknowledgements

Oulu, April 2002   Zuomin Zhao

List of symbols and abbreviations

a	radius of scattering particle
C_P	specific heat at constant pressure
C_{P0}	specific heat of water at constant pressure
c	concentration
d	thickness
E	laser pulse energy
E_a	absorbed energy
E_0	energy fluence of laser pulse
f_{ac}	acoustic frequancy
g	anisotropy factor
H	heat deposit function per unit volume and time
I	light intensity
I_a	acoustic intensity
I_c	collimated light intensity
I_i	incident acoustic intensity
I_t	transmitted acoustic intensity
I_0	radiation intensity
k	relative polarization factor
k_c	proportional constant
l	light propagation distance
l*	depth of collimated radiation to be transformed into diffuse radiation
n	refraction index
P	PA pressure amplitude
P_i	amplitude of incident acoustic pressure
P_s	PA amplitude produced by sturdy or large source
P_t	PA amplitude produced by thin or small source
P_{tr}	amplitude of transmitted acoustic pressure
P_0	initial PA amplitude
p	acoustic pressure
Q	mechanical factor
Q_E	dissipated energy on heater
Q_{Es}	dissipated energy on heater in soultion
Q_{Ew}	dissipated energy on heater in water

Q_a	total energy absorbed by apparatus
Q_e	escaped energy from the vacuum flask
Q_t	energy absorbed by sample
Q_{ts}	energy absorbed by solution
Q_{tw}	energy absorbed by water
R	measure of radius of acoustic source
R_b	measure of radius of laser beam
R_s	radius of cylindrical source
R_t	radius of spherical source
R_τ	stress relaxation factor
$R(r)$	diffuse reflectance
r	detection distance
$\mathbf{r}$	position vector
S	response of acoustic transducer
$\mathbf{s}$	directional unit vector
$\mathbf{s}'$	an another directional unit vector
T	acoustic transmittance
v	acoustic velocity
v_a	sound velocity in absorbing medium
v_t	sound velocity in transparent medium
Z	acoustic inpedance
Z_m	acoustic impedance of propagation medium
Z_t	acoustic impedance of transducer
Z_w	acoustic impedance of water
z_D	the length of near field zone (Fresnel zone)
α	optical absorption coefficient
α_{ac}	acoustic attenuation (absorption) coefficient
α_e	extinction coefficient
α_s	optical scattering coefficient
β	expansion coefficient
ΔC_p	difference of specific heat in glucose solution and water
ΔT	temperature change
ΔV	volume change
δ	optical penetration depth in medium
δC_p	change of specific heat
δh	initial expansion displacement
δP	change of PA amplitude
δR	radius change of acoustic source
δt	time different between the maximal compression and the minimal rarefaction in PA generation
δv	change of acoustic velocity
$\delta \alpha$	change of absorption coefficient
$\delta \beta$	change of expansion coefficient
$\delta \Gamma$	change of Grümeisen parameter
$\delta \mu_a$	change of absorption coefficient in scattering dominated media

Γ	Grüneisen parameter
κ_c	thermal conductivity
Λ	acoustic attenuation factor
λ	optical wavelength
λ_a	acoustic wavelength
λ_{dif}	heat diffusion length
μ_a	absorption coefficient of scattering-dominated medium
μ_e	extinction coefficient
μ_s	scattering coefficient
$\mu_s{}'$	reduced scattering coefficient
ρ	density
ρ_a	density in absorbing medium
ρ_t	density in transparent medium
τ	time measure of acoustic pulse
τ_a	acoustic transit time across the radius of acoustic source
τ_L	duration of laser pulse
τ_p	time of light pulse decreasing to 1/e intensity
ω	modulation frequency
ω'	solid angle
ω_0	albedo

CCD	charge coupling device
CW	continuous-wave
EDTA	ethylenediamine tetra-acetic acid
FET	field effect transistor
FPI	Fabry Perot interferometer
FT-IR	Fourier transform infrared
GOD	glucose oxidase
ISF	interstitial fluid
NDT	non-destructive test
NIR	near infrared
OCT	optical coherence tomography
OGTT	oral glucose tolerance test
OPO	optical parametric oscillator
PA	photoacoustic
PBS	phosphate buffer solution
PLS	partial least squares
PVDF	polyvinylidenefluoride
PZT	lead zirconium titanate
RBC	red blood cell
SEP	error of prediction
SRS	stimulated Raman scattering
TRSD	time-resolved stress detection

List of original papers

I   Zhao Z, Nissilä S, Ahola O and Myllylä R, "Production and detection theory of pulsed photoacoustic wave with maximum amplitude and minimum distortion in absorbing liquid", IEEE transactions on Instrumentation and Measurement, Vol. 47(2), pp.578-583, 1998.

II   Ahola O, Zhao Z, Tenhunen J, Nissilä S and Risto M, "Design of laser diode photoacoustic sensor for tissue measurements", Biomedical Sensors, Fibers, and Optical Delivery System, Proceedings of SPIE Vol. 3570, pp192-194, 1998.

III Zhao Z, Myllylä R and Nissilä S, "Laser-induced acoustic transmitter in tissue", Biomedical Optics (BMO´99), Proceedings of SPIE Vol. 3863, pp361-366, 1999.

IV   Zhao Z and Myllylä R, "Photoacoustic determination of glucose concentration in whole blood by a near-infrared laser diode", Biomedical Optoacoustics II, Proceedings of SPIE Vol. 4256, pp.77-83, 2001.

V   Zhao Z and Myllylä R, "The effect of optical scattering on pulsed photoacoustic measurement in weakly absorbing liquid", Measurement Science and Technology, Vol.12, pp. 2172-2177, 2001.

VI   Zhao Z and Myllylä R, "The scattering effect of glucose on near-infrared photoacoustic detection sensitivity in tissue measurement" Asian Journal of Physics, Vol. 10(4), 2001, accepted.

VII Zhao Z and Myllylä R, " Photoacoustic blood glucose and tissue measurement based on optical scattering effect" Saratov Fall Meeting, 2001, Proceedings of SPIE Vol. 4707-16, accepted.

Paper I studied the theory of photoacoustic generation and detection in absorbing liquids, focusing on the amplitude and duration of photoacoustic waves in plane, cylindrical, and spherical modes. Papers II and IV were about glucose measurements in whole human blood samples. In Paper III, a skin model was built and the photoacoustic source generated in it was simulated by the Monte Carlo method. Paper V studied the effects of optical scattering on photoacoustic sources and signals in weakly absorbing liquids by controlling the absorption and scattering coefficients of the samples. Paper VI experimentally demonstrated and analysed the increase in photoacoustic signals with increased glucose concentration in a milk solution and in tissue. Paper VII reports on the effect of glucose on optical scattering in blood. The study, employing the photoacoustic apparatus and a streak camera, included non-invasive photoacoustic experiments on a

human finger.

Onni Ahola, Lic.Tech., built the diode laser source and the driver used in the photoacoustic apparatus. The picosecond laser and streak camera system used in Paper VII was built by Dr. Sergey Vainshtein. The experimental apparatus for measuring the scattering coefficient in Paper V was made by VTT Electronics in Oulu. Papers I and VII were planned together with Prof. Risto Myllylä and Dr. Seppo Nissilä. The experiment in Paper II was carried out by Onni Ahola. The Monte Carlo simulation code used in Paper III was written by Dr. Lihong Wang and Dr. Steven Jacques. Other theoretical and experimental work was performed by the author. The manuscripts were written together with the co-authors.

Contents

Abstract
Acknowledgements
List of symbols and abbreviations
List of original papers
Contents

1 Introduction

1.1 Overview

Diabetes mellitus is a serious disease that affects not only the patient's internal organs, circulation system and eyesight, but also his entire life. There are reportedly more than 120 million diabetic people in the world at the moment, and this figure is expected to double within the next ten years [1]. The first step in diabetes care is to monitor the patient's blood glucose level 24 hours a day. Knowing the glucose level assists in determining the right diet and medical treatment.

Current methods of measuring blood glucose concentrations require the diabetic patient to puncture a finger to collect a drop of blood, whose chemical composition is then analyzed by a glucose meter. As the procedure is not totally painless and harms the skin, diabetics are often unwilling to check their glucose level as frequently as doctors would wish. During the last fifteen years, this has resulted in the proliferation of non-invasive measurements based often on optical methods. These are particularly suitable for the purpose, because they utilize non-ionizing radiation to examine the human body, they do not generally require consumable reagents and they provide fast responses. Moreover, the availability of low cost, sophisticated lasers and optical detectors add to the list of attractive characteristics.

All non-invasive optical methods utilize a beam of light to irradiate some selected part of the human body, such as a finger, the forearm, tongue, lip, thigh or abdomen and so on. Light that is transmitted through, reflected or scattered out of the skin comprises information about the composition of the illuminated tissue. This light is then received by optical detectors and analyzed to determine the concentrations of certain analytes, such as oxygen or haemoglobin. The analysis, however, is inherently complex because the received signal is often very faint and easily interfered with not only by a number of analytes in blood, but also by other factors including the variability and inhomogeneity of the human skin and the constantly changing human physiology. Other non-invasive methods take advantage of the correlation that exists between glucose content in the interstitial fluid and capillary blood. From the clinical point of view, the main flaw in these otherwise excellent methods is that they are time consuming. Furthermore, they only provide an indirect measure of glucose concentration which is, unfortunately, also

time-delayed.

The technique of laser photoacoustic (PA) spectroscopy has been used in trace detection due to the high sensitivity it offers. In this method, a high-energy laser beam is used to irradiate the matter under study. The beam produces a thermal expansion in the matter, thereby generating an acoustic wave. The characteristics of the wave are determined not only by the optical absorption coefficient of the matter, but also by such thermal physical parameters as thermal expansion, specific heat and sound velocity. In addition, the acoustic wave may also be affected by optical scattering which influences the distribution of light in the matter. Accordingly, relative to optical absorption spectroscopy, the PA technique offers an inherently higher degree of sensitivity. In the 1970s, PA spectroscopy made great progress in the trace analysis of gases and condensed matter [2][3][4][5][6][7]. Its application range quickly embraced the food industry, atmospheric inspection, semiconductor process, materials testing and in the oil industry, with a particular emphasis on the study of powders, gels, emulsions, suspensions and other highly scattering or opaque materials. The method allows a range of measurements, including *in vitro* and *in vivo* non-invasive online measurements. Unlike ordinary acoustics, sound waves produced by the PA method carry information about the material properties of the substance in which they are generated. Thus, they can be used to study both the propagation medium and the substance excited directly by the energy radiation. Since the 1990s, the pulsed PA technique has found frequent use in biomedicine, where it has achieved great progress in the non-invasive measurement of the optical properties of tissue, tissue diagnostics and imaging. However, the method faces similar difficulties as the aforementioned optical approaches in non-invasive blood glucose measurements.

This dissertation reports a set of studies involving photoacoustics, tissue optics and glucose measurements *in vitro*. The findings are also useful for certain other forms of trace detection as well. In addition, the experiences acquired during the study may also serve the future development non-invasive blood glucose determination methods.

1.2 Outline of the dissertation

Following this introduction, Chapter 2 describes the properties of glucose and common measurement techniques. The chapter opens with an analysis of the chemical properties of glucose, its molecular structure, and its concentration and locations in the human body. Then, the chapter provides an overview of the basic theory behind traditional glucose oxidation methods and their application to glucose determination, including a listing of widely used commercial blood glucose meters. Next, the chapter introduces new techniques for measuring glucose in the human interstitial fluid. Products based on these either minimally invasive or totally non-invasive techniques are just entering the market and will greatly improve the quality of life of diabetic patients. Non-invasive optical methods will be described in detail, for being completely non-invasive they provide a state-of-the-art method for determining glucose levels in blood. The characteristics and progress of one of these methods, namely, the PA method, will be described in an independent section to highlight its significance as the major research focus of this dissertation.

Chapter 3 describes the PA theory in liquid media. Six mechanisms for generating PA

waves are systemically overviewed, and thermal elastic expansion is pointed out as the most important PA effect. The second section classifies the PA technique into four styles on the basis of the modulation characteristics of the incident light source and the location of the PA generation. Additionally, the section also provides a summary of the properties and applications of the method. Section 3 describes in detail the theoretical foundation of the most important PA technique: the direct PA generation of thermal elastic waves by the pulsed excitation mode. The section includes qualitative physical explanations and a more rigorous theory for plane, cylindrical and spherical PA sources. Finally, the last section discusses the role of optical scattering on the PA amplitude.

An understanding of the properties of human tissue and blood are of paramount importance for non-invasive blood glucose measurements. Thus, Chapter 4 studies the composition and structure as well as the physical and optical parameters of skin and blood.

The emphasis in Chapter 5 is on simulating the distribution of PA source in a skin model. The chapter introduces the universal law of light transmission in turbid media, beginning with the radiative transfer equation and its approximate solutions for different cases. Then, a five-layer skin model is built at a wavelength close to 900 nm. Finally, the Monte Carlo method is applied to the simulation of PA sources in the skin model, excited by a narrow and a wide beam, respectively. The chapter also points out that the effective reception of the acoustic signal necessitates knowing the shape of the PA source.

Chapter 6 systemically studies the thermal elastic generation, relaxation, propagation, and reception of acoustic wave from the viewpoint of time-resolved stress detection (TRSD). The first section introduces the special properties of TRSD, and the requirements it poses for the exciting source and the reception scheme. The section also describes important applications of the method in biomedicine. The second section focuses on the formula of confined stress generation. The third section discusses stress relaxation and introduces the so-called relaxation factor. The following four sections centre on the diffraction and attenuation of acoustics waves, and a discussion on non-linear effects and boundary transmission. Section 8 considers the acoustic response of different transducer. Finally, Section 9 summarizes all factors that affect initial stress distribution.

Chapter 7 presents the experimental PA glucose measurements. First, the chapter explores the relative parameters of glucose, including its absorption coefficient, scattering effects, thermal expansion coefficient, specific heat and acoustic velocity. Second, the chapter provides a description of current near-infrared laser sources in PA generation. Section 3, in turn, discusses the most common piezoelectric and optical acoustic detectors and their application to glucose measurements, tissue diagnosis and imaging. Section 4 describes in detail the components of the pulsed PA apparatus based on the laser diode and PZT transducer used in the PA glucose experiments. In Section 5, glucose is studied in a water solution and in scattering samples such as milk, tissue and whole blood. Moreover, an attempt is carried out to measure the characteristics of the skin using the non-invasive PA method. The final section discusses the results of the experiment.

2 Current glucose measurement methods

2.1 Structure and physiological concentration of glucose

The molecular formula for D-glucose is $C_6H_{12}O_6$ and it has a molecular weight of 180.157. Being the most basic and common type of sugar, glucose is abundant in nature both in its free and combined form. Plants manufacture it from carbon and water through photosynthesis and it is transformed in plants and animals into different carbohydrates including monosaccharides, disaccharides and polysaccharides.

D-glucose is known to have two different kinds of cyclic structure, namely α-D glucose and β-D-glucose. As a hydrophilic molecule, glucose usually exists as a water solution. As Fig. 1 shows, an equilibrated monosaccharide solution contains five anomeric forms of D-glucose: β-D-pyranose-glucose (62.6%), α-D-pyranose-glucose (37.3%) and β-D-furanose-glucose (0.1%), in addition to very low concentrations of α-D-furanose-glucose and acyclic D-glucose [8]. Thus, if a pure anomer of glucose is dissolved in water, it will undergo mutarotation until a state of equilibrium is established between the anomers. This mutarotation is evident in the time-dependent infrared spectra of the solution [9].

In the human body, food is converted into sugar and provides energy to all tissues and organs through blood circulation. In terms of its chemical composition, human blood sugar consists of D-glucose that exists mainly in the water base of blood plasma [10]. In blood, the physiological glucose concentration is in the region of 18 ~ 450 mg/dl. Arterial and capillary blood taken from the fingertip have an identical glucose content, while the glucose level of venous blood is lower than the corresponding arterial value (1 ~ 17 mg/dl in healthy subjects and up to 30 mg/dl in diabetic patients). Besides blood, glucose also exists in other biofluids such as intracellular fluid, interstitial fluid, humour, saliva, sweet and urine. Researchers have established that, in the steady state condition, the glucose level in the intracellular and interstitial fluid is identical with the concentration of glucose in the blood. It is also known that the glucose level in humour correlates strongly with the glucose content of blood, while the glucose level in saliva, sweet and urine does not.
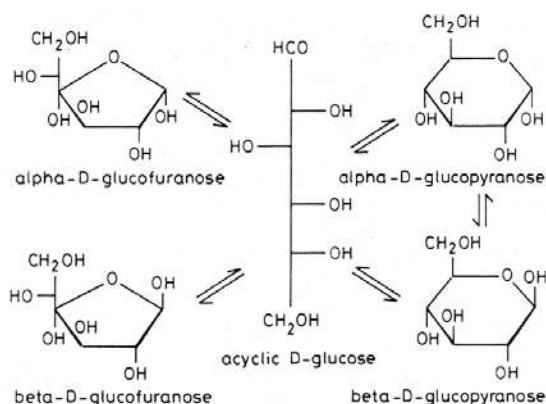
Fig. 1. Anomers of D-glucose in an aqueous solution [8].

2.2 Glucose oxidation methods

2.2.1 Theory

Traditional glucose determination is based on the glucose oxidation reaction, catalyzed by glucose oxidase (GOD). It may be described by

$$glucose + O_2 + H_2O \xrightarrow{\text{glucose oxidase}} gluconic\ acid + H_2O_2\ .$$
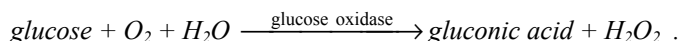
Glucose oxidase catalyzes the oxidation of β-D-glucose to D-gluconic acid and hydrogen peroxide. It is highly specific for β-D-glucose and does not act on α-D-glucose. Its major use is in the determination of free glucose in body fluids [11,12,]. Although specific for β-D-glucose, glucose oxidase can be used to measure the total amount of glucose. This is because, following the consumption of β-glucose, α-glucose at equilibrium is converted to the β-form by mutarotation. The consumed oxygen or the ensuing production of gluconic acid or hydrogen peroxide (H_2O_2) is in direct proportion to the glucose content. The glucose oxidase method is characterized by high sensitivity, accuracy and reliability.

Traditional electrochemical methods such as potentiometry or amperometry can be used to determine the glucose content during the glucose oxidation reaction. These methods are summarized in reference [13].

2.2.2 Blood sample measurements — invasive methods

Diverse enzymatic sensors based on glucose oxidation have been developed since the 1960s. The earliest blood glucose sensors were mainly used in the clinical environment or

at the bedside for the continuous detection of human glucose level. These devices include implantable sensors in the form of intravenous implants, needle-like probes whose sensor tip penetrates into the subcutaneous tissue and fully implanted subcutaneous devices requiring no communication across the skin. Shults et al. [14] describe a representative fully implanted sensor consisting of glucose oxidase laminated on a membrane, a sensing electrode system and a radio-telemetry transmission unit, with a total system weight of about 27 g. Powered by a tiny lithium battery with a predicted life-span of 1.5 years, the sensor transmits signals to an external computer. Although implanted sensors may be built economically using microchip technology, they are invasive and require contact with blood. This raises concerns about their long-term stability. In addition, the head of an implanted sensor should be non-toxic and non-reactive in blood or tissue.

In the late 1960s, blood glucose measurements were introduced for home use. They enable diabetic persons to inspect their blood sugar level visual colour changes on a chemical test strip or by displaying a reading on a glucose meter obtained from a drop of blood. The measuring principle is based on glucose oxidation and electrochemical methods. Usually, a few micro-litres of blood is taken by means of a finger stick or an arm stick. The blood is immediately placed on a test chip that is already inserted in a glucose meter. The meter displays the glucose concentration reading in a few tens of seconds. The main disadvantage of glucose meters is that they require patients to prick their skin, causing slight physical pain and harming the skin and the capillaries. Table 1 summarizes the main properties of some typical commercial blood glucose meters sold in the US:

Table 1. Some commercial glucose meters and their properties.

	Exac-Tech RSG	Precision Q.I.D.	Amira AtLast	Glucometer Dex	Fast Take	Accu-Check Advantage	FreeStyle
Manufac turer	Abbott Labs.	Abbott Labs.	Amira Medical	Bayer	LifeScan	Roche/ Boerhinger	Thera-Sense
Reference	Blood	Plasma	Plasma	Plasma	Plasma	Blood	Plasma
Sample (min) (µl)	10	3.5	2	3	1.5	4	0.3
Test time (sec)	30	20	15 ~ 30	30	15	40	15
Test range (mg/dl)	40 ~ 450	20 ~ 600	40 ~ 400	10 ~ 600	20 ~ 600	10 ~ 600	20 ~ 500
Test Position	Finger	Finger	Arm Thigh	Finger	Arm	Finger	Anywhere

It should be noted, however, that a new silicon micro-needle technique has been developed by Kumetrix Inc.. In this technique, taking a blood sample is like being bitten by a mosquito. Normally, humans are quite unaware of mosquito bites, they only feel a little itch and experience some swelling at the location of the bite, caused by enzymes that the insect uses to stop blood from coagulating. Although lacking these chemical agents, the silicon micro-needle is able to penetrate the skin and draw a blood sample painlessly, because it has a diameter that is smaller than that of a human hair. The current

system consists of a hand-held, battery-powered, electronic monitor that accepts a cartridge loaded with up to 10 disposable sampling devices. The heart of the device is a silicon chip that consists of a micro-needle and a receptacle into which the blood sample is drawn. To take a measurement, the cartridge is loaded into the monitor and pressed against the skin, causing the micro-needle to penetrate the skin to draw a very small volume of blood (one-hundredth the size of a blood drop or 100 nano-liters) into the receptacle. Chemicals inside the receptacle react with the glucose to produce a colour. The more intense the colour is, the higher the blood glucose level is. The monitor analyzes the colour by lasers and then displays the blood glucose concentration.

2.2.3 Permeance measurements in ISF—minimally- or non-invasive methods

Interstitial fluid (ISF) is an extracellular fluid through which chemicals (like glucose) and proteins pass on their way from the capillaries to cells. As a consequence, the glucose concentration of ISF exhibits a degree of correlation with the glucose concentration in the capillaries. Some researchers claim that the glucose concentration of ISF is practically identical to that of blood [15], whereas other investigators maintain that the equivalence is only about 75% [16]. The difference is probably attributable to the speed of the blood flow: as the glucose concentration increases, the time delay between observed changes in blood glucose and ISF glucose is 12 minutes. At any rate, glucose concentration in the ISF can be used to provide an indicator of the person's blood glucose value. ISF resides just under the skin, but the low permeability of the epidermal keratinised layer blocks the permiation of the fluid through the skin. During the past few years, however, some techniques have been developed for drawing glucose from the skin.

Iontophoresis is a process in which a weak electric current is employed to transport charged molecules through intact skin. The method also enables an increased transport of polar, as yet uncharged, species. The moving, charged molecules carry glucose and other chemical molecules found in the ISF through intact skin (reverse iontophoresis) [17]. Once the fluid is extracted from the skin, it can be collected and its glucose concentration determined by glucose oxidation methods. Hence, the measurement can be performed continuously without puncturing the skin. However, the slow transit time of the fluid through the skin produces a 20-minute lag in the blood glucose reading. In addition, the glucose concentration in the fluid is much lower than in the blood. While the size of the glucose sample varies with time and the current applied, the concentration is generally in the micromolar range, while that of blood glucose is in the millimolar range. Another drawback is that the test requires periodic calibration with blood testing. As a result, reverse iontophoresis is not a truly non-invasive method. Moreover, the accuracy of the measurement can be dramatically affected by the presence of sweat, and the low electric current passing through the skin may cause irritation.

The most successful iontophoresis-based glucose monitor is the GlucoWatch® Biographe, a wristwatch-type device developed by Cygnus Inc. in Redwood City, California [18]. The device collects glucose molecules in gel collection discs that are part of a single-use AutoSensor® containing the enzyme glucose oxidase. As glucose enters the discs, it reacts with the glucose oxidase in the gel to form hydrogen peroxide. A

biosensor in contact with each gel collection disc detects the hydrogen peroxide, and generates an electronic signal. The monitor uses a calibration value entered previously by the patient to convert the signal into a glucose measurement, which is displayed on the monitor and then stored in memory. The sensor is designed to take three measurements every hour and must be replaced every 12 hours. The patient is required to perform a routing blood-based calibration every day. To avoid the sweat effect, the GlucoWatch monitor measures skin conductance, which increases with sweat. If the skin conductance exceeds a predetermined threshold, the measurement is skipped. In December 1999, Cygnus received CE certification permitting the GlucoWatch Biographer to be sold in the European Union.

SpectRx Inc. in Norcross, Georgia, has also developed a smart method for accessing ISF in the skin. The method applies a low-cost, low-energy laser to create micropores in the stratum corneum. The depth of these micropores is only about 20 micrometers, just the thickness of stratum corneum, the layer of dead, nonviable epidermal cells forming the outer skin surface. The micropores' diameter is approximately equal to that of a human hair. The method offers several advantages. Firstly, the procedure is completely painless. Secondly, it allows an analysis of the actual ISF, not just partial compositions thereof, thereby enabling a direct glucose concentration measurement by conventional glucose assay techniques such as the glucose oxidase method. The continuous monitoring system is usable for three days at a time. The test patch can be placed on almost anywhere (arms, abdomen and legs) on the human body with no loss of accuracy. Finally, and most importantly, the procedure does not require calibration from a finger stick blood measurement. Clinical tests involving 20 diabetic patients show that the correlation between SpectRx ISF measurements and blood glucose levels is as high as 0.90 in the 60-400 mg/dl glucose range.

Another, relatively similar method has also been reported [19,20]. In this method, the stratum corneum is first stripped, whereafter effusion ISF is sampled by suction and its glucose concentration is measured by an ionsensitive FET.

Ultrasound, especially low frequency ultrasound, can induce cavitation in and around the skin. The oscillation and collapse of cavitation bubbles disorder the lipid bilayers of the skin, resulting in enhanced skin permeability. The process is known as sonophoresis. It was first used to enhance the transdermal delivery of drugs, but its application range was soon extended to include the transdermal monitoring of glucose and other analytes [21,22]. Accomplishing a transdermal glucose flux through the skin involves two steps. First, the skin is pre-treated by a low frequency ultrasound (20 kHz, for instance). Second, glucose is extracted using passive diffusion, low intensity ultrasound or a vacuum. Without ultrasonic pre-treatment, the permeability of glucose through a rat's skin is less than 0.0004 ± 0.0003 cm/hr. Ultrasonic pre-treatment and extraction increase this permeability to 0.026 ± 0.011 cm/hr (or 0.034 ± 0.025 cm/hr for vacuum extraction), representing 100-fold enhancement. Clinical data shows that the skin retains a high level of permeability for about 15 hours after the ultrasonic treatment. The correlation coefficient between monitored transdermal glucose level and venous glucose level is about 0.9. The time delay between these glucose levels is about 12 minutes. Patients report no pain during the ultrasound and the technique leaves no visible effects on the skin.

Other minimally invasive techniques for monitoring glucose concentration include a painless, hollow lancet used for collecting tiny drops of ISF (Integ), a microdialysis probe

[16], an inserted sensor (MiniMed Technologies) and a fluorescent sensor (Sensor For Medicine). Nevertheless, all these techniques harm the skin, albeit slightly.

2.3 Non-invasive optical methods

As all methods based on glucose oxidase require a direct contact between glucose and some chemical reagents, they necessitate the extraction of glucose from the body. As a result, many research groups and companies over the world have tried to develop non-invasive glucose measurements based on optical methods, in which an optical beam interacts with glucose within the human body. The thus generated signals are then analyzed and the results displayed. Since optical methods do not require the extraction of glucose from the body, they are highly suitable for the continuous, non-invasive monitoring of glucose. Good overviews over non-invasive optical techniques are provided by references [23,24,25,26,27].

Non-invasive optical techniques are based on near-infrared light, i.e. light at wavelengths between 600 ~ 2300 nm, which is capable of penetrating from a few hundreds of micrometers to several millimeters into human tissue or fluid. The light is modified by the tissue after transmission through the target area such as a finger tip, forearm, abdomen, thigh, ear lobe, lip, anterior chamber of the eye and so on. The diffuse light that escapes from the tissue it has penetrated produces an optical signature or fingerprint of the tissue's content. The proportion of light that is absorbed and scattered depends on the structure of the tissue (thickness, location, layers, tissue fluid, blood vessel distribution) and on its chemical components (melanin, water, haemoglobin, fat, glucose). The glucose concentration of the tissue can be determined by analyzing changes in the intensity, polarization or wavelength of the optical signal, which correlates with ISF, intracellular fluid and capillary blood in the illuminated volume.

However, the ratio of body fluids (intracellular, interstitial, plasma) are affected by factors such as activity level, diet or hormone fluctuations, but also by blood circulation, body temperature shift, metabolic activity and medication. All these factors are capable of influencing the optical parameters and, consequently, impacting the blood glucose measurement. Moreover, day-to-day changes in vasculature and tissue texture as well as the ageing process may affect the long-term stability of glucose monitoring.

2.3.1 Near-infrared transmission and reflectance

When near-infrared light illuminates a spot on the skin, the light is partially absorbed and scattered as a result of its interaction with chemical components in the illuminated tissue. Light that is not absorbed will be reflected out of the tissue or transmitted through it, before being received by optical detectors. An analysis of changes in the intensity of the light combined with the application of multivariate calibration techniques [28,29,30] permits the extraction of the tissue's chemical components, including glucose.

Robinson [31] used NIR transmission spectroscopy and the multivariate calibration method to measure blood/tissue glucose concentrations in diabetic subjects. He

investigated several conventional spectrometer configurations using transmission sampling in the 600 ~ 1300 nm range. The reported average prediction errors varied from 19.8 to 37.8 mg/dl in oral glucose tolerance tests (OGTT) conducted on three subjects. Burmeister and Arnold [32], in turn, employed near-infrared transmission spectroscopy to study noninvasive blood glucose sensing in different measurement sites (the cheek, lip, nasal septum, tongue and webbing tissue). The results showed that the tongue, containing the least amount of fat, provided spectra with the highest signal-to-noise ratio. They collected the transmission spectra of the tongue in the 1400 ~ 2000 nm ranges. Their findings showed a standard error of prediction (SEP) in excess of 54 mg/dl for all diabetic subjects [33]. Hiese and Marbach [34,35,36] have reported a series of studies on glucose determination in the oral mucosa membrane in the 1111 ~ 1835 nm spectral range through a diffuse reflectance measurement. The best SEP was 43 mg/dl from a 2-day single-person OGTT. Jagemann, Fischbacher, Danzer and Muller [37,38,39] used a fibre optic probe to study diffuse reflectance over the 800 ~ 1350 nm range on the middle finger of the right hand. The blood glucose concentrations of the test persons were perturbed using carbohydrate loading. The results were evaluated using the partial least-squares regression method (PLS) and radial basis function neural networks. In these tests, the mean root square prediction error was 36 mg/dl.

2.3.2 Spatially-resolved diffuse reflectance measurements

The spatially resolved diffuse reflectance technique applies a narrow beam of light to illuminate a restricted area on the surface of a body part and to measure the ensuing diffuse reflectance at several distances from the illuminated area. The intensity of this reflectance depends on both the scattering coefficient and the absorption coefficient of the tissue. Reflectance measured in the immediate vicinity of the illuminated point is mainly influenced by scattering off the skin, while reflectance farther away from the light source is affected by both scattering and the absorption properties of skin. Then, the recorded light intensity profiles are used to calculate the absorption coefficient μ_a and the reduced scattering coefficient μ_s' of the tissue based on the diffusion theory of light propagation in tissue [40,41]. Because μ_s' and glucose concentration are correlated, the latter can be extracted by observing changes in the former [42,43].

Bruulsema et al [44] carried out a glucose clamp experiment to measure the diffuse reflectance. An optical probe was fixed on the patient's abdomen. The clamping protocol consisted of a series of step changes in blood glucose concentration from the normal level of 5 mM to 15 mM and back to 5 mM. Three different clamping experiments were done on the body of diabetic volunteers at wavelength of 650 nm. The corresponding changes in μ_s' were estimated to be about -0.20%/mM, -0.34%/mM and -0.11%/mM, respectively. A qualitative correlation between the estimated change in μ_s' and the change in blood glucose concentration was observed in 30 out of 41 diabetic volunteers. Heinemann [45] obtained a similar result (-1.0%/ 5.5 mM) in their glucose clamp experiments. However, under normal conditions, blood glucose concentration does not change as rapidly as the clamping experiments suggest. Hence, OGTT was applied in the measurement of diffuse reflectance in reference [46] at the wavelength of 800 nm. The results indicated a mean relative change in μ_s' of about -0.5 %/mM and 0.3%/mM for healthy persons and type II

diabetic patients, respectively. The acceptable correlation between blood glucose concentration and μ_s' was 75% (27 out of 36 measurements).

2.3.3 Frequency-domain reflectance technique

The optical system used in frequency-domain reflectance measurements is similar to that in above diffuse reflectance measurements, except that the light source and the detector are modulated at a high frequency [47,48,49]. Then, the phase and intensity of the photon-density wave generated by the source are measured. Combining these measurements with linear transport theory enables the deduction of μ_a/n and $n\mu_s'$, where n is the mean refractive index of the tissue. Maier et al [42] applied the frequency-domain tissue spectrometer to do an OGTT for a non-diabetic male. The optical source had a wavelength of 850 nm and the measurement location was muscle tissue in the subject's thigh. The experimental results showed that the relative change of μ_s' with blood glucose concentration was -2.5%/3.6mM, which is identical with the results obtained by Heinemann [46].

2.3.4 Polarimetry

The polarimetric glucose measurement is based on the observation that glucose molecules in aqueous solutions rotate the polarization plane of linearly polarized light. The rotation angle is proportional to the glucose concentration in the sample. At the physiological glucose concentration of 100 mg/dl and with a path length of 1 cm, the optical rotation angle is about 5 millidegrees [27]. However, the skin is a highly scattering medium that depolarizes up to 95% of the light, when light in the red wavelength range passes through 4 mm of tissue thickness [24]. As a consequence, the best measurement location for a noninvasive polarimetric measurement is the anterior chamber of the eye where optical scattering is very small compared to other tissues.

March et al performed in vivo measurements on a rabbit's eye using an amplitude-based polarimeter [50], and Coté later developed a phase measurement polarimeter in order to increase the signal-to-noise ratio [51]. The steady-state glucose concentration in the aqueous humour was about 70% of that in the human whole blood [52], and the measurement contained a time lag of about 30 minutes [53]. Although there are a lot of published papers related to the polarimetric glucose measurement in vitro [51,53,54,55], there are as yet no human clinical data.

2.3.5 Raman spectroscopy

When incident light is scattered inelastically, the scattered photons lose (Stokes shift) or gain (anti-Stokes shift) energy, owing to transitions between rotational and vibrational energy states within the scattering molecules. The resulting optical frequency shifts can

be measured to collect specific information about the chemical structure of the sample. Compared with near-infrared spectroscopy, Raman spectroscopy monitors fundamental vibrations, which are sharper and exhibit less overlap. Moreover, water has a low Raman cross-section, although its infrared absorption capacity is high. However, scattering effects and the re-absorption of light in bio-tissues make the detection of Raman signals a difficult task. Protein molecules, for example, produce a background fluorescence signal that is often equal to or larger than the Raman signal itself. For these reasons, the anterior chamber of the eye and aqueous humour are the best sites for noninvasive Raman measurements. Unfortunately, these are sensitive parts of the body, and the signal level has to be low such that the power of incident irradiation is confined to a safe dose.

A number of references discuss Raman spectroscopy in *in vitro* glucose measurements, in which the lowest limit of detection is in the physiological glucose concentration range [56,57,58,59,60,61]. Tarr and Steffes [60] have conducted noninvasive studies on the ocular aqueous humour using stimulated Raman spectroscopy and predicted a potential glucose measurement level of 0.01% over a 1 cm path length. However, no *in vivo* or clinical results have been published so far.

2.3.6 Optical coherence tomography

The optical coherence tomography (OCT) is a relatively new, high-resolution tissue imaging technology (10 μm or less). The apparatus consists of a low-coherence light source such as a superluminescent diode and an interferometer, which is employed to determine the depth of the backscattering feature by measuring the delay correlation between backscattering light in the sample arm and reflected light in the reference arm. A cross-section image is formed by collecting interference data at various points on the sample's surface. A good overview over the topic is provided by an excellent article by Schmitt [62].

OCT was originally designed by Huang and Fujimoto to provide images of the human eye [63], but in 2000, Larin and Larina [64] applied it to the noninvasive monitoring of glucose concentration. In their technique, two-dimensional intensity distributions from an OCT skin image were averaged into a single curve to obtain a one-dimensional distribution of light in the depth dimension. Then, the 1-D distribution was plotted in the logarithmic scale as a function of depth, and finally, the slopes of the obtained OCT signals were calculated and shown to correlate with the glucose concentration of the skin. The results demonstrated that at 1300 nm the slope of the OCT signal fell more than 40% as the blood glucose concentration increased from 4 mM to 28.5 mM (-1.65% per 1 mM of glucose) in glucose clamping experiments on animals. The drop was caused by a change in the scattering properties of the skin layer at the depth of 150 ~ 500 μm. The result is indicative of a considerably higher detection sensitivity than can be obtained by other noninvasive optical techniques.

OCT has the apparent advantage of being able to measure and analyze coherently scattered light from a specific skin layer. This may greatly decrease interference caused by other factors that affect scattering, such as physiological changes at deeper skin depths or moisture up-take on the skin's surface. Hence, OCT offers high sensitivity, accuracy and specificity in noninvasive glucose determination. Moreover, it eliminates the use of

complicated multivariate calibration. OCT is a brand new technique, but it holds a great promise for noninvasive glucose determination in the future.

2.3.7 Other methods

Infrared emission spectroscopy is based on measuring black body radiation at the skin. This radiation is absorbed by the fundamental absorption bands of glucose at 9.1 ~ 10.5 μm. As the surface cools, glucose near the surface begins to absorb more than it emits. This produces a reasonably good glucose absorption spectrum which can be super-imposed on the usually smooth blackbody spectrum, to get an indication of the skin's glucose concentration. Klonoff [65] used the method to study a few type I diabetic cases *in vivo*. His clinical calibration data revealed a linear relationship between the detected glucose and the actual blood glucose concentration. The multiple least squares fit provided the correlation coefficient of 0.94 and a standard error of 24.7 mg/dl.

Using broadband light illumination, broadband overlapping filters and multiple detectors, kromoscopy, developed by Optix Corp., has presumably great potential for noninvasive glucose determination [66,67,68]. It is claimed to have superior sensitivity compared with spectroscopic methods. Additionally, the method is reportedly based on the ability of the eye to determine slight changes in colour. The reports, however, fail to discuss the effects of light scattering.

Fluorescence-based glucose determination techniques are not non-invasive, despite claims to the contrary in the literature. These techniques fall into two categories; they employ either glucose-oxidase based or affinity-binding sensors. Sensors in the former category use GOD to induce the electro-enzymatic oxidation of glucose to generate an optically detectable glucose-dependent signal [69,70,71], as described in Section 2.2.1. Sensors in the latter category utilize competitive binding between glucose and a suitably labelled fluorescent compound at a common receptor site [72,73]. In general, fluorescence-based techniques have high specificity to glucose thereby minimizing potential interference. The drawback, however, is that they involve the injection of chemicals into the body and are susceptible to degradation over time.

2.4 Photoacoustic methods

Compared with optical absorption techniques, the photoacoustic methods offer the advantage of higher detection sensitivity, as the PA signal is influenced not only by the optical absorption coefficient, but also by other physical parameters including thermal expansion, specific heat and acoustic velocity. This has been demonstrated in the determination of traces and oils in liquids. The basic principle behind the PA mechanism is that an energy source (a pulsed laser, for example) irradiates some absorbing material, causing a fast thermal expansion in the illuminated volume. The energy of the expansion is released as an acoustic wave. A detailed description of the PA mechanisms and techniques will be provided in Chapter 3.

A research group led by H.A.Mackenzie in UK first applied a pulsed PA method to

the measurement of blood glucose. The group employed near-infrared PA spectroscopy to the study of glucose aqueous solutions and blood components [74]. To demonstrate the possibility of non-invasive detection of glucose in the human body, Quan et al. [75] carried out an experiment using a gelatine-based tissue phantom and a circulation system containing a glucose solution. The reported detection sensitivity at 1.064 μm was 0.071% per mmol/l. At the same time, Christison [76] applied a hybrid pulsed TEA CO_2 laser to the detection of physiological glucose concentrations (18 ~ 450 mg/dl) in human whole blood. The achieved sensitivity was declared to be comparable to that of the existing commercial enzyme-based diagnostic systems presently used in clinical chemistry environments at hospitals. In 1995, the research group built a portable non-invasive blood glucose monitor based on the PA method, comprising one or more laser diodes emitting at the 904 nm wavelength. Having tested the apparatus, the group reported a correlation coefficient of 0.967 in observed blood glucose concentrations between the PA response and hospital tests on a venous blood sample [77]. In Germany, a research team headed by Spanner also used PA and optical techniques to investigate haemoglobin and glucose in the human body [78]. It is worth noting that they used a special modulating array of laser diodes. Recently, the correlation between glucose concentration and the reduced scattering coefficient of tissue has been put forward and confirmed. A research group lead by Oraevsky established that 1 mmol/l increase in glucose concentration resulted in a 3% decrease in the optical attenuation of a rabbit's sclera *in vivo*. The result was obtained by measuring a laser-induced acoustic profile using the time-resolved PA technique at 355 nm [79]. This sensitivity far exceeds any values achieved in previous *in vivo* glucose measurements.

2.5 Summary

Glucose measurements based on glucose oxidation are capable of producing an exact glucose concentration value, due to their ability to detect glucose molecules directly – a capacity which traditional glucose sensors and most commercial glucose meters on the market utilize. Unfortunately, these methods usually require implanting a sensor into the body or drawing body fluid from the skin. This may result in biocompatibility problems, infections, physical pain or slight harm on the skin (although some permeance methods may reduce these problems to a minimum). On the other hand, most of the optical approaches listed in Section 2.3 eliminate all such disadvantages. Moreover, sophisticated, inexpensive optical and electrical devices may greatly decrease the cost of continuous glucose monitoring. However, until recently, non-invasive optical methods have not been widely applied in the clinical environment, mainly because the optical absorption of glucose is very weak in the near infrared "human tissue window", compared to that of other chemicals in the skin and in subcutaneous tissues. The result of absorption method is a low detection sensitivity and easy susceptibility. Although detection sensitivity may be improved by spatially diffuse reflectance techniques, based on evaluating changes in scattering produced by light that is reflected from the skin, the problem is, however, that it is very difficult to distinguish changes in scattering produced by glucose concentration changes from those produced by other physiological drifts in the skin and complicated subcutaneous tissues. In contrast with spatially diffuse

reflectance, OCT is capable of selecting a specific skin layer for analysis, thereby greatly decreasing interference from other skin layers. The method is expected to produce satisfactory clinical results in the near future. Methods based on polarimetry and Raman scattering are capable of producing more specific information of glucose molecules, but depolarisation effects and the background fluorescence of skin tissue limit their application to the anterior chamber of the eye, as far as non-invasive measurements are concerned. No clinical result however has been reported. Finally, PA techniques, based on light-induced ultrasonic waves, suffer from similar problems as the optical absorption and diffuse reflectance method. They do, however, offer the benefit of higher detection sensitivity and a much simpler apparatus. In addition, they do not require complicated multivariate calibration.

3 Conventional photoacoustic theory in liquid

3.1 The mechanisms of PA generation

All modulated energy beams, such as those comprised of electromagnetic radiation, x-rays, electrons, protons, ions and other particles, are capable of generating an acoustic sound when they interact with matter. However, the most popular method of producing PA waves, is modulated light energy. Light consists of non-ionising radiation, which is not harmful to the human body, and there is an unlimited supply of diversified, convenient, cheap and effective optical sources and devices.

In liquids, the generation of PA waves is generally the result of two different mechanisms: optical absorption followed by thermal de-excitation, as in thermal expansion and liquid boiling, or non-thermal de-excitation, as in the case of photochemical processes and breakdown. In addition, optical non-absorption, such as electrostriction and radiative pressure, may also produce acoustic waves. The thermal elastic expansion mechanism is an interesting choice for material characterization and medical diagnosis for a variety of reasons. Firstly, it does not break or change the properties of the object under study. Secondly, it has a linear or a definite relationship with many of the physical parameters of diverse materials. Thirdly, it is non-destructive or non-invasive in application such as materials test and medial diagnosis. Fig. 2 provides a summary of the various methods capable of generating PA waves.

Thermal elastic expansion — When a modulated light source, such as laser, irradiates an absorbing medium, the ion specific absorption in the illuminated region produces heat due to non-radiative relaxation. This heat causes the region to expand. If the pulse duration of the laser is short enough or its modulated frequency rapid enough, the thermal expansion will be exceedingly fast. Such modulated thermal expansion causes the illuminated region to extend and compress, owing to inertial effects within the medium. As a result of this action, an acoustic wave is generated and propagated outside. This wave is subsequently detected by an acoustic transducer. The amplitude of the acoustic wave is linearly proportional to the absorbed energy density, while the shape of the wave is dependent on the absorption distribution, laser parameters and boundary condition. Although the conversion efficiency of optical energy in the thermal expansion mechanism is below 10^{-4} in liquid media, the process offers sufficiently high sensitivity

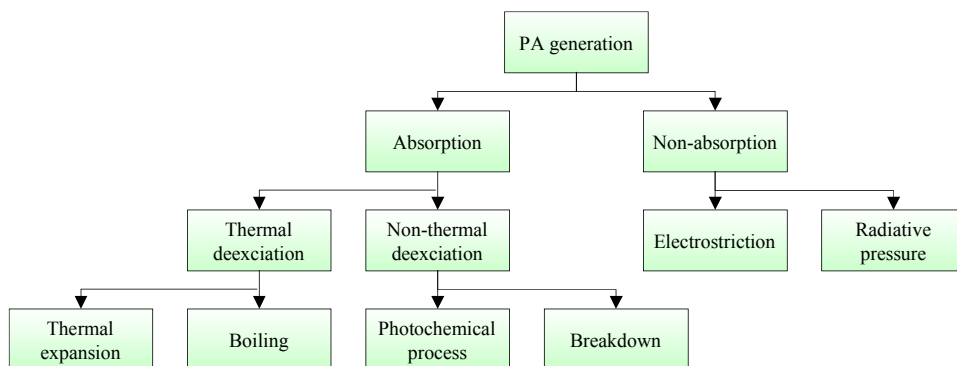for physical parameter measurements, PA diagnosis and PA imaging.

Fig. 2. Mechanisms for generating photoacoustic waves.

Vaporization and boiling — If the absorbed laser energy density within the absorbing region of a medium exceeds a certain threshold determined by the optical and thermal properties of the medium, the generated heat may cause the temperature to rise. If the medium gets hot enough, the result will be vaporization and internal boiling. For water, the threshold is 2.24 kJ/cm^3 [80]. This process involves a momentum exchange between the ejected molecules or particles and the liquid sample, which, consequently, produces shock waves with pressure amplitudes in the kilobar range [81]. In hard biological tissues, these shock waves may be used to destroy sick tissue as in laser-induced lithotripsy. In this case, the conversion efficiency can reach 1% [82], which is much higher than the corresponding figure for thermal expansion. The peak acoustic pressure, with a mono-pulse shape, is proportional to the laser power [83]. In weakly absorbing media, it may be impossible to induce observable vaporization and boiling up to the breakdown point.

Dielectric breakdown — Dielectric breakdown is caused by the interaction of a medium and an optical beam with a very high optical intensity. References [84, 85] investigate the effects of this phenomenon in liquids both experimentally and theoretically. In a pure medium, the threshold can be as high as 10^{10} W/cm^2 [82]. Dielectric breakdown may generate a strong acoustic wave (> 50 MPa in water) [86]. As its conversion efficiency may reach 30% in liquids [82], this mechanism is the most efficient process for converting optical energy into acoustic energy. Dielectric breakdown can be realized even in transparent media, where acoustic generation caused by ordinary absorption does not occur. If the medium includes some discrete impurity centres, the dielectric breakdown threshold may be decreased. Reference [83], for example, reports that a CO_2 laser with an intensity of 10^8 W/cm^2 can produce dielectric breakdown and a series of spherical shock waves in CS_2 liquid. Similar experiments have been carried out using water.

Photochemical process — Some mechanisms based on photochemical effects are capable of generating acoustic emission [87]. They include complementarity in photo-synthesis, energetics in the purple menbrane of the *Halobacterium halobrium*, gas

evolution or consumption, and photochemical chain reactions. It should be noted, however, that gas evolution or consumption may produce a larger PA signal than the thermal expansion mechanism, and that a photochemical chain reaction may cause an extremely large and prolonged PA emission.

Electrostriction — The electrostriction effect can be explained by the electric polarizability of molecules which causes them to move within the illuminated region such that a density gradient is produced in the medium. If the irradiated optical energy is fast modulated, a change in the density gradient will form an acoustic wave. As a mechanism for generating acoustic waves, electrostriction has a rather restricted role, being limited to transparent or very weakly absorbing media subjected to an electric field with high field strength ($> 10^7$ V/cm). This can be observed by studying the wave amplitude ratio generated by electrostriction and thermal elastic expansion. The amplitude ratio is equal to about $10^{-5}/\alpha$ for a cylindrical source in water [87], where α (cm^{-1}) is the optical absorption coefficient of the medium and the optical pulse duration is 1 microsecond. Hence, electrostriction can be neglected in many biomedical applications.

Radiative pressure — When light irradiates the surface of a medium, the maximum radiative pressure caused by the change in the momentum of the light beam on reflection is equal to *2I/c*, where *I* is the intensity and *c* the velocity of light in the medium. Fast-modulated light produces a modulated pressure change and emits an acoustic wave. Nevertheless, the thus generated acoustic wave is considerably smaller than that produced by other PA mechanisms.

3.2 General PA techniques

According to the generating location of acoustic wave, PA techniques can be classified as either direct of indirect. In direct scheme, provided that the optical absorption of a sample is not too high, a portion of an incident light will penetrate into the sample and generate an acoustic wave within it. This enables the study of the internal composition and structure of the sample. The sample does not need to be enclosed in a volume, which is an important consideration for a number of practical applications, including industrial online measurements and *in vivo* determination and imaging in biomedicine. The most common method of direct PA generation is the piezoelectric PA technique, which offers a very high sensitivity for the measurement of the absorption coefficient (as low as 10^{-7} cm^{-1} for same cases)[88]. As a consequence, modern PA techniques are usually based on direct PA generation, which will be studied in detail in Section 3.3.

In the indirect PA method, an acoustic wave is produced in a coupling medium adjacent to the sample, usually by means of heat leakage and transmission from the sample. As the coupling medium is typically a gas or a liquid, this technique usually needs an enclosed PA cell, especially in the case of gas coupling and microphone detection. Applications include conventional PA spectroscopy, which has a proven track record in the study of gases. However, this approach suffers from certain crucial limitations in the case of condensed matter, such as the narrow bandwidth of microphone responses, the relatively complex nature of the heat transfer process from the condensed matter to gas and the inability to perform experiments at low pressures. Despite these limitations and its low detection sensitivity in condensed matter, the indirect PA method

is a valuable tool in the study of opaque and such strongly absorbing samples that disallow the passage of light. A summary of the theory can be found in reference [87].

PA techniques can also be classified as continuous-wave (CW) modulation mode and pulsed mode. In CW mode, the duty cycle of the modulated beam is close to 50%. As a duty cycle of such size may produce spurious effects, such as heating of the sample and convection currents, the boundary conditions of the acoustic cell are important for the generation of the PA signal. The acoustic resonance of the cell may be used to maximize the PA response. Signal analysis is often performed in the frequency domain. Because of its boundary condition dependence, the CW mode is usually not suitable for online or *in vivo* measurements. Moreover, the CW mode suffers from apparent thermal diffusion in the generation of the PA response, thereby lowering its PA efficiency and sensitivity. Furthermore, the CW mode is inapplicable to biomedical PA imaging and diagnosis. As a result, almost all modern PA techniques utilize the pulsed excitation mode.

The so-called pulsed mode uses a high power, low duty cycle optical source to excite a PA wave. Because optical energy is deposited in the sample in a relatively short time (usually in the region of 5 ns to 1 μs), thermal diffusion effects can largely be ignored and the PA efficiency is greatly improved. This eliminates the effects of sample heating and convection currents that usually occur in the CW excitation mode, due to the low average power of the pulsed source. Combined with the time gating technique, which can only be employed in association with the pulsed mode, the PA signal produced in the target region is capable of discriminating against other spurious PA signals produced by window absorption or light scattering, for instance. As a result, the detection sensitivity is greatly improved, compared with the CW excitation mode. During one excitation pulse, the typical acoustic propagation distance is 1.5 mm or smaller in aqueous samples, which is much smaller than the ordinary sample scale. Hence, the boundary condition of the acoustic cell or sample is usually unimportant for the PA signal generated within it. Furthermore, it should be noted that only the pulsed mode can be used in time-resolved PA tomography.

3.3 Thermal-elastic direct PA generation by pulsed excitation mode

As described in Section 3.1, several mechanisms can produce PA effects, but in terms of liquid analysis, thermal elastic expansion is of particular relevance. Compared with radiation pressure and electrostriction, the thermal elastic mechanism produces a large PA response. In addition, unlike dielectric breakdown, evaporation and the photo-chemical process, it does not break or change the properties of the sample. Moreover, the thermal elastic PA process exhibits a simple proportional relationship between the signal amplitude and optical absorption or thermal physical parameters (such as thermal expansion coefficient, sound velocity and specific heat). For the high sensitivity and convenience it offers for practical applications, the generation of PA waves by the thermal elastic method in the pulsed excitation mode is undoubtedly the most important in PA techniques. Paper I related some useful results, while this section provides further details.

3.3.1 Qualitative theory

Using the simple thermodynamic principle, we may deduce the relationship between the amplitude of the PA response and the parameters of the sample and the light source. Although the deduction is qualitative, the results are in good agreement with those provided by a rigorous theory. This study discusses PA sources with a regular geometrical shape, namely, cylindrical, plate and spherical models. In practice, the acoustic source either can be approximated or consist of such models.

3.3.1.1 Plane source

If the absorption coefficient of a liquid is so large that the optical penetration depth δ is much smaller than the radius of the light beam, the shape of the sound source is like a plane, as shown in Fig. 3. If all of the absorbed energy is converted into thermal energy to heat the liquid, it causes a temperature rise ΔT in the illuminated region. According to the law of thermodynamics, it has

$$\Delta T = \frac{E_a}{C_P \rho V} \; , \tag{1}$$

where E_a is the absorbed pulse energy, V is the optical absorbed volume, and C_P and ρ are the specific heat and density of the liquid, respectively.

There are two special cases where the laser pulse width τ_L is longer or shorter than the light penetration depth δ divided by the acoustic velocity v, shown in Fig. 3:
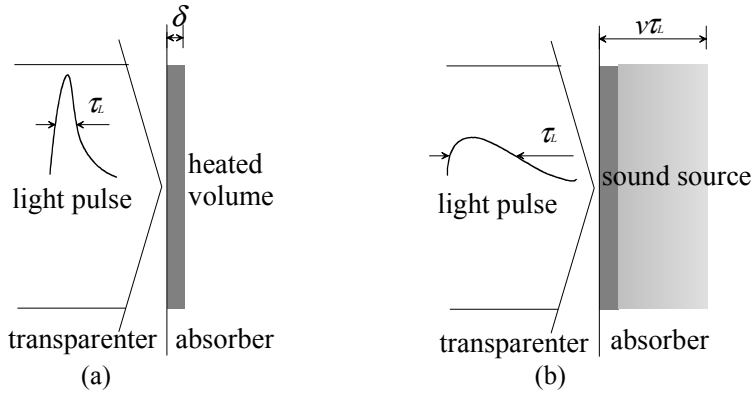

Fig. 3. Plane photoacoustic sources produced by short and long pulsed lights.

Short light pulse ($v\tau_L \ll \delta$): In Fig. 3a, the short laser pulse does not allow the heated volume enough time for isobaric expansion. This results in a pressure increase

produced at the edge of the illuminated plane just after laser pulse. Bearing in mind that the pressure P and the strain $\beta\Delta T$ are related by the bulk modulus ρv^2 of the liquid, i.e.

$$P = \rho v^2 \beta\Delta T , \tag{2}$$

where β is the thermal expansion coefficient. Substituting the temperature rise in Eq. (1) and the volume of the source

$$V = \pi R_b{}^2 \delta , \tag{3}$$

into Eq. (2), the pressure amplitude becomes

$$P_t = \frac{E_0 \alpha \beta v^2}{C_P} , \tag{4}$$

where E_0 is the energy fluence of the laser pulse and equals $E/\pi R_b{}^2$. E is the laser pulse energy and it can be assumed to equal E_a in the case of strong absorbing media. R_b is a measure of the radius of the optical beam. δ is the penetration depth and is equal to the inverse of the absorption coefficient α^{-1}.

Long light pulse ($v\tau_L \gg \delta$): In Fig. 3b, immediately after the laser pulse, the active source thickness is not δ anymore, but $v\tau_L$ because of acoustic propagation. We get the initial displacement δh due to thermal expansion from

$$\pi R_b{}^2 (v\tau_L + \delta h) - \pi R_b{}^2 v\tau_L = \beta\pi R_b{}^2 v\tau_L \Delta T . \tag{5}$$

In this case, the source volume is equal to

$$V = \pi R_b{}^2 v\tau_L . \tag{6}$$

Substituting Eqs. (1) and (6) into Eq. (5), we have

$$\delta h = \frac{E_0 \beta}{\rho C_P} . \tag{7}$$

The peak acoustic pressure of long light pulse is related to the expansion displacement as

$$P_s \approx v\rho\delta h / \tau_L . \tag{8}$$

Substituting Eq. (7) into Eq. (8), we have

$$P_s \approx \frac{E_0 \beta v}{C_P \tau_L} . \tag{9}$$

It is worth noting that the pressure amplitude has no relationship with the optical absorption coefficient in the case of a plane source irradiated by a long light pulse. The ratio of Eqs. (4) and (9) is

$$\frac{P_s}{P_t} = \frac{\delta}{v\tau_L} = \frac{1}{\alpha v\tau_L} \ll 1 . \tag{10}$$

This means that, all other conditions being identical, a short light pulse will produce larger pressure amplitude than a long pulse.

3.3.1.2 Cylindrical source

When the absorption coefficient of the illuminated liquid is so small that the light penetration depth is much larger than the diameter of the light beam, the PA source can be regarded as cylindrical in shape. Patel and Tam give a description of this case in reference [88]. Tam modified these parameters by considering the real dimensions of an acoustic source [87]. Here, the amplitudes of the PA pressure are written out directly by

$$\left| P_t \right| = \frac{E\alpha\beta}{C_P \tau_L^{3/2}} \left(\frac{v}{r} \right)^{1/2} , \tag{11}$$

for a long pulse source ($\tau_L \gg \tau_a$) or a thin cylindrical source, and by

$$\left| P_s \right| = \frac{E\alpha\beta v^2}{C_P R_s^{3/2} r^{1/2}} , \tag{12}$$

for a sturdy cylindrical source or a short pulse source ($\tau_L \ll \tau_a$). The proportional constant is ignored in the equations above. r is the distance between the PA source and the observation point, R_s the source radius and τ_a the transit time that an acoustic pulse travels across the radial direction of acoustic source.

It must be pointed out that the radius of the acoustic source differs from the radius R_b of the laser beam. If τ_L is much longer than τ_a, the acoustic source radius equals $v\tau_L$, rather than R_b. In this case, the radius of the laser beam has little effect on the PA amplitude. The PA amplitude, however, is strongly affected by the duration of the laser pulse. This is the case for a thin cylindrical source as expressed in Eq. (11). Only in the case that τ_L is considerably shorter than τ_a, is the acoustic source radius near equal to R_b. In this case, the laser duration has little effect on the PA amplitude. This is the case of a sturdy source as expressed in Eq. (12).

3.3.1.3 Spherical source

The sound source is spherical in shape, for example, when a laser pulse illuminates an absorbed droplet in a transparent liquid, and the absorbed energy E_a in the droplet is assumed to be homogeneously distributed. Another case involves liquid surface illuminated by a laser beam with an optical penetration depth that is near equal to the radius of the beam. In this case, the shape of the sound source is hemispherical. Using the same method as in Section 3.3.1.1, the amplitude can be deduced as

$$P_t(r) = P(R_t / r) \approx \frac{E_a \beta v^2}{C_P R_t^2 r} , \tag{13}$$

for a big source or a short light pulse ($\tau_L \ll \tau_a$) and

$$P_s \approx \frac{E_a \beta}{C_P r \tau_L^2} , \tag{14}$$

for a long light pulse ($\tau_L \gg \tau_a$) or a point source. In this equation, E_a is proportional to the laser pulse energy E and the absorption coefficient of the liquid, and R_t is the source radius. The ratio of Eq. (14) and Eq. (13)

$$\frac{P_s}{P_t} \approx \left(\frac{R_t}{v \tau_L} \right)^2 \ll 1 , \tag{15}$$

also shows that a longer light pulse produces a weaker acoustic signal, all other conditions being equal (in actuality, the output energy of the laser tends to vary with the duration of the laser pulse).

3.3.2 Rigorous theory

Knowing the shape of the wave and its frequency spectrum facilitates the design of the acoustic detector and the effective reception of sound waves. The information of PA wave shapes is not known in Section 3.3.1 because of simple modes. A more rigorous theory, described in this section, can solve this problem.

When the heat conduction time in the absorbing medium exceeds the transit time of acoustic wave in PA source and the so-called viscous effect can be ignored, the formation of photoacoustic waves can be described by the thermally generating wave equation

$$\left(\nabla^2 - \frac{1}{v^2} \frac{\partial^2}{\partial t^2} \right) p = -\frac{\beta}{C_p} \frac{\partial H}{\partial t} , \tag{16}$$

where H is a function defined as the heat deposited in the medium per unit volume and time. Because H correlates closely with the parameters of the light source and the properties of the medium, it is impossible to provide a general analytic solution for any shapes of laser pulse and absorbing volume, excluding the special cases in below.

3.3.2.1 Plane source

If a laser irradiates a strongly absorbing liquid, a plane-shaped source is formed under the boundary of the illuminated area, as shown in Fig. 4. In the frequency domain, the heat function in the absorbing liquid can be expressed by

$$H(z,t) = \alpha I_0 e^{-i \omega t} e^{-\alpha z} , \tag{17}$$

where ω is the modulation frequency of the radiation intensity I_0.

heat function: $H(z,t) = \alpha I_0 \, e^{-\alpha z} \, \delta(t)$

optical beam

acoustic wave

acoustic wave

0

z

transparent medium   absorbing medium
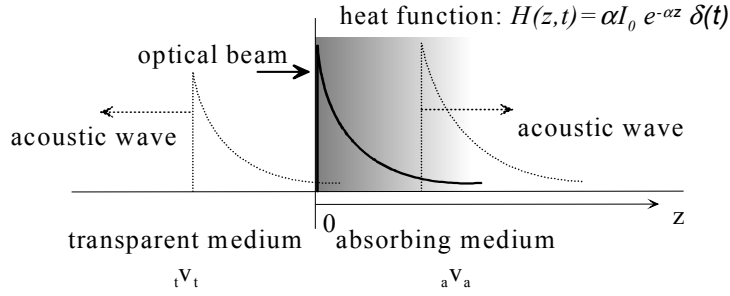
$_t v_t$

$_a v_a$

Fig. 4. Generation and propagation of acoustic waves in a plane PA model.

Pressure p must be continuous across the interface between two media. Moreover, the gradient of the pressure divided by the densities of media must also be continuous. The acoustic pressure produced by a short-pulsed laser (producing a delta heat function) can be obtained by a simple Fourier transformation of the frequency domain solution, i.e.

$$p_a(\tau) = \frac{E_0 \alpha \beta v^2}{2 C_P} \{ \Theta(-\tau) \cdot e^{\alpha v_a \tau} + R_c \cdot \Theta(\tau) \cdot e^{-\alpha v_a \tau} \} , \qquad (18)$$

$$p_t(\tau_t) = \frac{E_0 \alpha \beta v^2}{2 C_P} T \cdot \Theta(\tau_t) \cdot e^{-\alpha v_t \tau_t} , \qquad (19)$$

where

$$R_c = \frac{\rho_t v_t - \rho_a v_a}{\rho_t v_t + \rho_a v_a} ,$$

$$T = \frac{2 \rho_t v_t}{\rho_t v_t + \rho_a v_a} ,$$

$$\tau = t - z/v_a ,$$

$$\tau_t = t + z/v_t ,$$

$\Theta(\tau)$ is the Heaviside unit function and ρ and v are the density and the acoustic velocity of the medium, respectively. The subscripts a and t describe the parameters in the absorbing and the transparent media.

The first term in Eq. (18) is a forward-going wave under the absorbing medium, while the second term is a reflection wave at the incident interface. When a short pulsed laser is just fired ($t < z/v_a$), $\tau < 0$ forces the second term in Eq. (18) to zero. As a result, only a forward-going wave can be detected at any point in the absorbing medium. After time $t > z/v_a$ has passed, $\tau > 0$ reduces the first term to zero but the second term begins to operate. This means that the forward going wave has passed the point, and the reflection wave dominates the wave shape. Eq. (19) describes the acoustic wave that is transmitted back to the transparent medium from the PA source in the absorbing medium. All the waveforms are exponential, just like the form of the heat function or that of the distribution of optical absorption in an absorbing medium.

The specific acoustic waveform in an absorbing medium is determined by its

reflection coefficient R_c. Practical applications involve three common cases. In the case of a rigid boundary, light incidents a liquid sample from the glass window of a cuvette, and R_c is roughly equal to 1. In the free boundary case, a laser irradiates the liquid directly (although there may be a layer of air on the liquid surface), in which case, R_c equals -1. In the non-boundary case, a laser beam passes through a non-absorbing liquid to arrive at an absorbing one. If the two liquids have similar acoustic properties, R_c is nearly equal to zero. These results have been demonstrated by Park et al [89].

The acoustic pressure generated by a long pulsed laser ($\tau_L \gg \tau_a$) can be obtained by a convolution integral between the incident radiation and the sound pressure produced by the delta heat function. Since the incident pulse intensity has a Gaussian distribution, i.e.

$$I_0 = \left(\frac{E_0}{\sqrt{\pi} \tau_L} \right) \cdot e^{(-t^2/\tau_L^2)} , \tag{20}$$

the acoustic pressure in the non-boundary case is equal to

$$p(\tau) = \frac{E_0 \beta v}{2\sqrt{\pi} C_P \tau_L} \cdot e^{(-\tau^2/\tau_L^2)} . \tag{21}$$

Similar to Eq. (9), the pressure amplitude bears no relationship to the optical absorption coefficient. The waveform keeps same transient information of irradiating pulse. Sigrist gave an experimental demonstration of a case involving a long pulse [82].

3.3.2.2 Cylindrical source

When the optical absorption capacity of the illuminated liquid is weak, the laser beam penetrates a long distance into the medium, producing a cylindrical PA source. PA generation in a cylindrical source has been explored in detail in two milestone papers [88,90], which also provide a prediction of the formats of the amplitude and waveform of the PA response. If the optical absorption coefficient of the liquid is low, although higher than 10^{-5} cm^{-1} (which is typical for all bio-tissues), the electrostriction effect is too small to generate a PA wave and can thus be ignored. Lai and Yong [90] deduced the PA pressure expression as

$$p(r,t) = \frac{E\alpha\beta\sqrt{v}}{8\sqrt{\pi} C_P \sqrt{r}} \tau_e^{-3/2} \frac{d\Phi_0(\xi)}{d\xi} , \tag{22}$$

in which

$\tau_e = \sqrt{\left(\tau_p^2 + \tau_a^2 \right)}$,

$\xi = (t - r/v_a)/\tau_e$,

$\tau_a = R/v$,

R is a measure of acoustic source, τ_p is a measure of the duration of the light pulse, and $d\Phi_0/d\xi$ is the shape function of the wave. The shape of the wave consists of a relatively strong albeit short compressive pulse followed by a weaker but broader rarefaction pulse.

The time difference between the maximal compression and minimal rarefaction is

$$\delta t = 2.35 \cdot \tau_e = \sqrt{\left(\tau_L{}^2 + \frac{(2.35R)^2}{v^2} \right)} . \tag{23}$$

Hence, for a long optical pulse ($\tau_L \gg \tau_a$), Eq. (22) is identical with Eq. (11), and similar to Eq. (12) for a large beam radius ($\tau_L \ll \tau_a$). Eqs. (22) and (23) show that the laser pulse duration should be short and the optical beam radius should be small to generate a sharp PA pulse. In this case, the radial distribution of the laser beam has little effect on the generation of PA waves.

3.3.2.3 Spherical source

Some researchers [80] [83] [[91]] have explored PA generation in a spherical PA source. The model submitted by Hu [80] is suitable for the case of a long pulse or a small source, while Sigrist and Kneubühl [83] used a heat function represented by a three-dimensional heat pole to deduce the pressure expression. This model corresponds to the case of a short laser pulse or a large heat source.

In addition, Hutchins [86] and Hoelen [91] have suggested a single effective time scale τ_e, similar to the case of a cylindrical source. For Gaussian laser beam, the pressure can be expressed by

$$p(r,t) = \frac{E_a \beta}{2\pi^{3/2} C_P \tau_e{}^2 r} \left(\frac{t - r/v}{\tau_e} \right) \exp \left\{ -\left(\frac{t - r/v}{\tau_e} \right)^2 \right\} . \tag{24}$$

The pressure waveform consists of a positive and a negative peak with same amplitude. The time difference between two peaks can be deduced from Eq. (24), i.e.

$$\delta t = \sqrt{2}\tau_e . \tag{25}$$

3.3.2.4 More popular PA theory

Based on Eq. (16), Diebold *et al* [92] explored more popular solutions for three PA models: the absorbing volume of an infinite wide plane, infinite long cylinder and spherical ball which are immersed in a transparent fluid with identical acoustic properties. The PA amplitude and wave width are summarized in Paper I, and the wave shape is described as follows:

(a). In a plane model, the time profile of the PA wave is directly described by the spatial deposition of heat from a short light pulse. The PA waveform excited by a long light pulse is directly proportional to the intensity of the exciting radiation evaluated at the retarded time from the origin.

(b). In a cylindrically symmetrical model, the PA pressure produced by a short light

pulse consists of waves propagating both outward and inward. The inward wave is reflected at the symmetrical axis and arrives at the field point with an inverted amplitude at a time delay relative to the outgoing wave. The PA waveform excited by a long light pulse is proportional to the (½)th time derivative of the intensity of the exciting radiation evaluated at the retarded time from the origin.

(c). In a spherically symmetrical model, the time profile of the PA wave excited by a short light pulse is a mapping of the product of the retarded time with the spatial heating function evaluated at positive and negative values of the retarded time from the origin. The PA waveform excited by a long light pulse is proportional to the time derivative of the intensity of the exciting radiation evaluated at the retarded time from the origin.

3.4 Scattering effect

The basic theory explained in Section 3.3 relates to three source models (plane, cylindrical and spherical) in purely absorbing media. However, many studied objects in engineering and biomedicine are turbid or optically scattering media. This section serves to furnish the optically scattering and its effect on amplitude of photoacoustic wave.

3.4.1 Scattering mechanism

Optical scattering is caused by in-homogeneity in the refractive index of a medium. The intensity and spatial distribution of the scattering light depends on the size and shape of the in-homogeneity relative to the optical wavelength and disparity of the refractive index. Two cases of scattering are usually considered.

Rayleigh scattering relates to scattering particles whose radius a is considerably smaller than the wavelength λ of the incident light (usually, $a < \lambda/20$). Thus, it could be assumed that the instantaneous electric field is uniform over the extent of the particle. An oscillating dipole moment is established within the particle, which isotropically radiates secondary waves of the same wavelength as the excitation. This forms the scattering radiation and is of relatively low intensity. The most significant features of Reyleigh scattering are the λ^{-4} and a^6 dependencies of the scattered light intensity.

If $a > \lambda/20$, we are dealing with so-called Mie scattering. In this case, the electromagnetic field across the particle can no longer be considered uniform, and the following alternative approach must be taken to determine the intensity of the scattered light. A beam incident upon a particle may be thought of as consisting of several individual rays following their own paths. Their light is scattered by means of reflection, refraction and diffraction. Mie theory may be used to determine the fields at any point inside and outside the particle, and, consequently, the distribution of the scattered light may also be determined. The scattering intensity tends to be greater than in Rayleigh scattering, but in a more forward direction. Mie scattering occurs normally when the size of a particle illuminated by visible or near-infrared light is larger than one sub-micrometer.

The effect of scattering can be thought of as a removal of a proportion of the incident intensity from the propagating beam, in much the same way as the effect of absorption.

Beer´s Law is then modified as

$$I = I_0 e^{-\alpha_e l} , \tag{26}$$

where α_e is the extinction coefficient and equals the sum of the absorption and scattering coefficient, and l is the light propagation distance.

3.4.2 Scattering effect in photoacoustics

In terms of energy, the photoacoustic signal is insensitive to the scattering effect, because the PA signal is determined by the absorbed fraction of the incident optical energy that is converted to heat. The scattering event does not include the absorption of energy. However, the photon density distribution of light changes when it is scattered. This produces a modification in the heated region and brings about a corresponding change in the shape of sound source.

Few researchers have studied and discussed the effects of optical scattering in photoacoustics. Helander and Lundstrom consider a semi-infinite (optically and thermally thick) and isotropically scattering sample [93] [94], and Yasa gives a general unified analysis of the effects of scattering in most common PA spectroscopes for arbitrary sample thickness and scattering characteristics [95]. The results indicate that scattering does affect the PA signal to some degree. The calculated maximal change in the PA amplitude is about one order of magnitude for all cases, when the scattering coefficient changes by four or five orders of magnitude. Thus, the PA technique provides a higher degree of immunity from the scattering effect than the optical method. Although the results above are based on continuous-wave excitation, some of them are suitable for the pulsed mode as well.

A detailed description of the scattering effect on the PA signal necessitates a complicated analysis, as the effect depend on the size, shape, concentration and absorption of particles and the background absorption coefficient. In the case of weakly absorbing media, optical scattering increases the mean photon path, corresponding to an increase in the number of absorbed photons. On the other hand, scattering also widens the radius of a cylindrical PA source. As both factors have an opposite effect on the PA amplitude, it almost remains unchanged. This has been experimentally demonstrated in reference [74]. When scattering increases, more photons are likely to be scattered out of the sample rather than be absorbed by it, so the PA amplitude begins to decrease. If scattering becomes strong enough, some outward scattering photons may be scattered back to the PA source, causing a slow amplitude decrease, as described by Fig. 7 in Paper V. Hence, a qualitative description of the scattering effect on a cylindrical PA source can be summarized in Fig. 5.
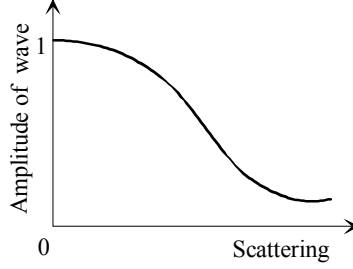
Fig. 5. Optical scattering effect on the PA amplitude of a cylindrical source.

When scattering is well in excess of background absorption, and the incident optical beam is so wide that the diameter of the light beam and the thickness of the sample are larger than the effective optical pathlength, the generated PA source becomes plane-shaped. Karabutov [96] has deduced an approximate formula for the scattering effect in such a plane PA source. He assumes that the reduced scattering coefficient μ'_s is much larger than the absorption coefficient μ_a in a sample which is illuminated by a short light pulse ($\mu_{eff} v \tau_L \ll 1$). The intensity distribution of the PA source is expressed by

$$p(z) = \frac{\beta v^2}{4 C_P} \mu_{eff} E_0 \cdot \left[e^{\mu_{eff} l^*} - e^{-\mu_{eff} l^* (2\Delta + 1)} \right] \cdot e^{-\mu_{eff} z}, \tag{27}$$

where

$$\mu_{eff} = \sqrt{3 \mu_a (\mu_a + \mu_s')},$$

$$\Delta = \frac{2}{3} \left(\frac{1 + R_{eff}}{1 - R_{eff}} \right),$$

and $z > 2l^*$. l^* is the depth at which the collimated radiation incident on the sample is transformed into diffuse radiation. R_{eff} is the effective reflection coefficient of the diffuse radiation from the interface, and z is a spatial axis which originates at the surface of the medium and is directed vertically into it. It is well known that optical intensity is maximal at $z \approx l^*/2$ in the case of illumination by a wide laser beam, corresponding to the maximum PA amplitude. When μ'_s increases, $p(z)$ decreases in the range of $z > 2l^*$ in Eq. (27). Hence, it can be deduced that $p(z)$ will increase in the range of $z < 2l^*$ due to energy conservation. This means that the PA amplitude increases as scattering becomes stronger in this case.

4 The properties of tissue and blood

Optical imaging and non-invasive diagnosis of the human body depend strongly on the optical and physical properties of skin and blood. The composition and morphology of the skin are very complicated. Therefore, to build a reasonable optical model of the skin, its composition and structure must be studied in advance.

4.1 Skin tissue

4.1.1 The composition and structure

The structure and properties of skin vary considerably in different parts of the body. A typical structure is shown in Fig. 6, while Table 2 and Table 3 list the average elemental composition and the biochemical composition of the skin, respectively.

The skin is usually divided into three layers, namely, the epidermis, dermis, and subcutaneous fat, each with their own sublayers. The outermost layer of the epidermis is composed of a relatively thin, but rough, protective top layer of dead and dry skin cells, known as the stratum corneum or horny layer. The remainder of the epidermis, including the stratum lucidum, stratum granulosum and stratum spinosum, is made up of cells called keratinocytes as well as melanocytes, which are pigment cells responsible for skin pigmentation. The thickness of the epidermis varies from 0.1 mm in the eyelids to nearly 1 mm on the palms and soles [97]. The dermis consists of a variety of cells, fibres, amorphous ground substance, nerves, oil glands, sweat glands, blood vessels and hair roots. Its upper layer is called the papillary dermis and contains the vascular network and sensory nerve endings, whereas the deeper layer, referred to as reticular dermis, consists mainly of a loose connective structure and epithelial-derived structures such as glands and follicles. The thickness of the dermis varies from 0.3 mm in the eyelids to about 3 mm in the palm and soles [97]. Subcutaneous fat is composed of fat cells, which form a cushioning layer between the skin and the deeper muscles. It also has an abundant blood content.
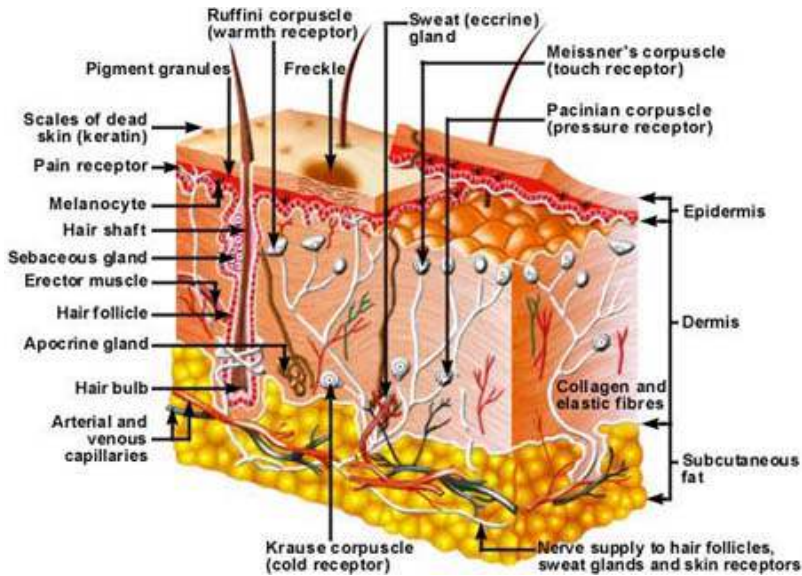
Fig. 6. A structure of human skin [98].

Table 2. Average elemental composition of the skin, percentage by mass [104].

O	C	H	N	Na	Mg	P	Cl	K
59.4 ~ 69.5	25 ~ 15.8	10 ~ 10.1	4.6 ~ 3.7	0.2	0.1	0.2	0.3	0.1

Table 3. Percentage constituents of adult human skin [104].

Water	Protein	Lipid	Ash
58.6 ~ 72.1	22 ~ 27.2	5.2 ~ 13.5	0.7

4.1.2 Optical absorption

Being composed of water as well as proteins and lipids, the chemical make-up of the skin influences its optical absorption properties. Water absorbs photons at wavelengths longer than the middle infrared range, while proteins are strongly absorbing in the ultraviolet and violet region. Fortunately, the optical absorption capacity of water, proteins and lipids is small in the red and near-infrared region. This region, known as the "tissue optical window", ranges from 600 nm to 2300 nm and allows light to penetrate from a few hundreds of micrometers to a few millimetres into the skin tissue. As a result, it can be exploited for a variety of purposes, including diagnosis, imaging or therapy.
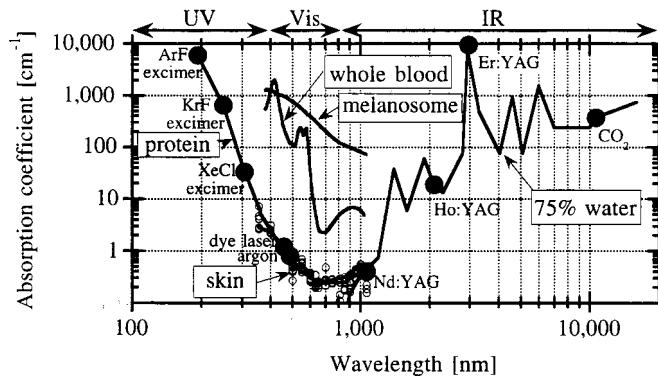
Fig. 7. The absorption spectrum of tissues [99].

At the shorter wavelengths of the tissue optical window, from 600 nm to 1100 nm, the most important photon absorbing chromophores are blood and melanin. Water becomes dominant at incident wavelengths longer than 1150 nm. The epidermis does not contain any blood and its water content is also much lower that of the dermis. However, the stratum granulosum and stratum spinosum comprise some melanocytes, including melanin, which is involved in skin pigmentation. Because the absorption capacity of melanin is stronger than that of blood and water, it is the dominant source of absorption in the epidermis at shorter near-infrared wavelengths. The volume fraction of melanosomes in the epidermis can vary from 1.3 ~ 6.3% for light-skinned adults, 11 ~ 16% for well-tanned adults and 18 ~ 43% for darkly pigmented Africans [99]. The blood content of the dermis is about 0.2 ~ 5%, representing the main source of absorption at wavelengths shorter than 1100 nm. If the optical wavelength exceeds the near-infrared range, water content becomes an important consideration in terms of optical absorption.

It is a well-known fact that the measured values of absorption coefficient of a tissue are different *in vitro* and *in vivo* measurements [100,101]. This can be explained on a number of grounds. First, soaking the tissue sample in saline prior to an *in vitro* measurement may alter its optical properties, and increase the amount of reflectance. Also other kinds of tissue treatments, including freezing, drying, heating or deforming, may change the optical properties of the sample. Second, measuring and calibration procedures may introduce an error into the determined values for diffuse reflectance and total transmittance. Third, the use of simplified calculation methods may result in an incorrect interpretation of the measured data, as in the case of internal reflectance at tissue boundaries.

4.1.3 Optical scattering

Optical scattering is caused by a mismatch or a fluctuation in the refractive index of a medium. The measured refractive index of soft tissues lies in the range of 1.33 ~ 1.55 [104, 114]. Optical scattering in the skin is mainly due to three contributors: the collagen

fibres of the dermis, the membranous ultrastructures of cells, and small-scale scattering from particles or refractive index fluctuations in polymers or lipid aggregations.
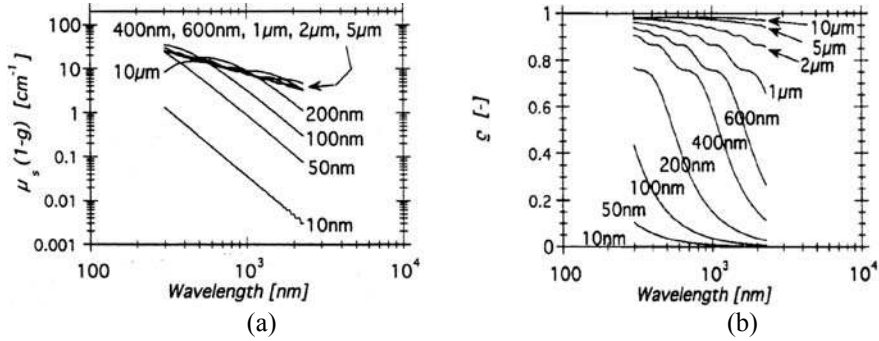

(a) (b)

Fig. 8. Reduced scattering coefficient (a) and anisotropy (b) of collagen fibres for a volume faction of 20% while n_r=1.38/1.35 [99].

Collagen fibres are the major scattering source in the skin's dermis. The diameter of these fibres vary widely from about 0.1 µm in fibrils to 8 µm in fibre bundles. Saidi et al. measured the densities and diameters of collagen fibres in nine neonatal skin specimens [102] and reported that the mean fibre density value was 3×10^6 cm^{-3} per unit volume, and the mean fibre diameter was 2.8 µm. The fibre volume fraction was 21%. The refractive index of collagen fibrils in dermis is estimated at 1.38 [99], while the refractive index of dermal ground substance is assumed to be 1.35, based on estimates in references [103, 104]. Inserting these parameters in cylindrical Mie scattering theory, the reduced scattering coefficient and the anisotropy of collagen fibrils can be computed. The results are shown in Fig. 8.

The membranous structures of the cell include the cell membrane, endoplasmic reticulum, mitochondria, liposomes, nuclei and the entire cell itself, covering a range of sizes from roughly 0.1 ~ 10 µm. However, all these structures are based on the basic lipid bilayer structure, which is approximately 0.1 µm in thickness. Table 3 indicates that the average volume faction of lipids in the skin is about 10%. Based on the refractive index range for hydrogenated fats (1.43 ~ 1.49), the average refractive index of membranes is estimated as 1.46 [99]. The background refractive index of the dermal substance is chosen as 1.35. Now, by applying Mie scattering theory to spheres with a diameter in the region of 0.01 ~ 10 µm, the reduced scattering coefficient and the anisotropy of membranes can be calculated, as shown in Fig. 9.

Fig. 9 also presents small-scale scattering in the skin produced by particles or refractive index fluctuations for spheres with a diameter of 10 nm. Because this dimension is smaller than one-twentieth of the wavelength of the irradiating light, this scattering can be regarded as Rayleigh scattering, constituting a limit to Mie scattering. In this case, the scattering varies with the wavelength as λ^{-4}. It can be seen that scattering caused by small particles is more wavelength-dependent than that by large particles. Moreover, small particles scatter much less at longer wavelengths than large ones. When

the diameter of the particles is larger than 600 nm, the reduced scattering coefficient reaches its maximum value, whereafter it starts to decrease slightly with the increase of particle size. The anisotropy, in turn, increases with the size of the scattering particles and decreases with wavelength. The particles with a size in excess of 1 μm are strongly forward scattering ($g > 0.9$) in near infrared, while scattering produced by particles with a size less than 100 nm is nearly isotropic ($g \approx 0$).

(a)   (b)
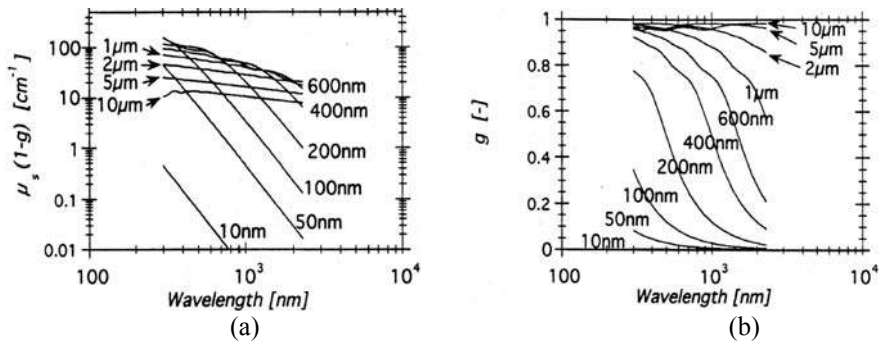
Fig. 9. Reduced scattering coefficient (a) and the anisotropy (b) of spheres for a volume faction of 10% while n_r=1.46/1.35 [99].
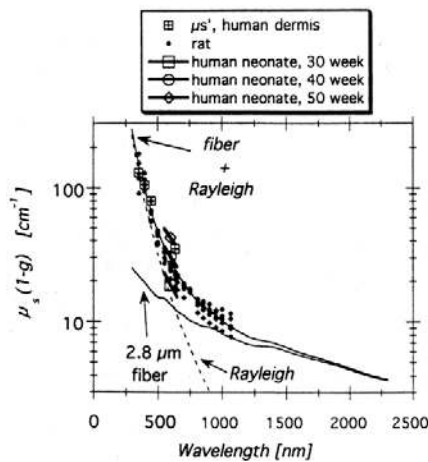
Fig. 10. Reduced scattering coefficient of the skin and the Mie scattering equivalent of a 2.8-μm-diameter collagen fibre at 21% volume fraction and the addition of Rayleigh scattering by small-scale ultrastructure [99].

A few references measured the reduced scattering coefficient of bloodless skin specimens using the integrating sphere *in vitro* and *in vivo* [97, 101, 102,]. The data were analysed by means of delta-Eddington diffusion theory or the Adding-Doubling method.

Fig. 10 summarizes the results and compares them with Mie theory equivalents of 2.8-μm-diameter collagen fibres plus Rayleigh scattering by small-scale ultrastructure. It demonstrates that, for bloodless skin, the contribution of membrane scattering can be ignored. Experimental results concerning the anisotropy of skin are hitherto insufficient.

4.1.4 Other physical parameters in Photoacoustics

Besides optical parameters, other physical parameters such as the expansion coefficient, specific of heat, acoustic velocity, acoustic impedance, acoustic attenuation and thermal conductivity strongly affect PA generation and propagation. These parameters are a function of temperature, but acoustic attenuation and velocity are also closely related to the frequency of the PA wave. At room temperature, the $\beta v^2/C_P$ of bloodless skin is about 0.15 [105]. This figure is somewhat larger than the corresponding value of water (0.11 [106]) while being slightly smaller than that of whole blood (0.18 at 20 °C, calculating from Section 4.2.2). The other physical parameters of the skin and tissues are presented in Fig. 11 and Table 4.
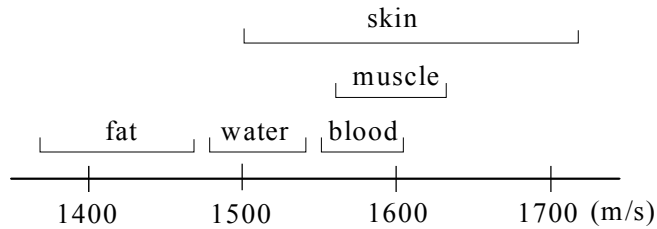
Fig. 11. Acoustic velocities in tissues and water [107].

Table 4. Tissue parameters relative to acoustic propagation [104].

	Density (kgm^{-3})	Characteristic impedance ×10^{-6} (Rayl = kgm^{-2}s^{-1})	Acoustic attenuation (dB/cm/MHz)
skin	1012 ~ 1065	1.51 ~ 1.84	3.7
muscle	1070	1.69	1.5
fat	950	1.38	
blood	1060	1.62	0.15
water	993	1.516	0.0022

4.2 Human blood

4.2.1 Composition of whole human blood

The composition of whole blood is shown in Fig. 12, with an emphasis on the main absorption substance – haemoglobin, which is the oxygen-transporting protein consisting of a globin and a heme (iron-carrying) portion. The volume fraction of cells in whole blood is about 47% ± 5% in a man and 42% ± 5% in a woman. Of the volume, 99% is erythrocytes, i.e., red blood cells (RBC). Haemoglobin, in turn, accounts for about 30% of an RBC's weight. The morphological parameters of blood cells are listed in *Table 5*.
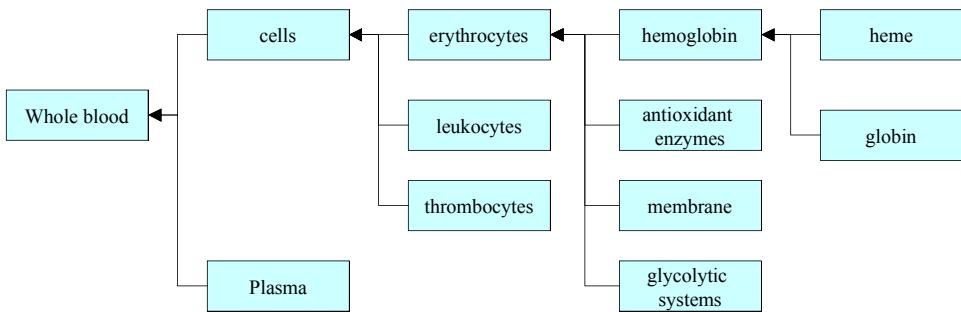
Fig. 12. Composition of whole blood.

Table 5. Morphological parameters of cells in blood [108].

	Volumetric Concentration (%)	Number Concentration (mm^{-3})	Shape	Characteristic Size (μm)	Volume (μm^3)
erythrocytes	46	$(4.2 \div 8.6)10^6$	biconcave discoidal	7.1÷9.2*1.7÷2 4	70÷100
leukocytes	1.2	$(4 \div 8)10^3$	spherical	8÷22	
platelets	0.3	$(2.5 \div 5)10^5$	discoidal	2÷4	6

4.2.2 Thermodynamic and acoustic parameters

Table 6 lists such physical parameters of blood that play an important role in PA generation and propagation:

Table 6. A few physical parameters of blood related with PA generation [104].

Thermal expansion coefficient: $(10^{-4}/°C)$	Specific heat $(J·kg^{-1}·K^{-1})$	Density (kg/cm^3)
2.5 (15 ~ 20 °C)	= 3950 - 7.24H	
3.5 (25 ~ 30 °C)	(H: haematocrit %)	1052 ~ 1064
4.0 (35 ~ 40 °C)	3624 (37.5°C)	

Thermal conductivity $(w/m·K)$	Acoustic velocity (m/s)	Ultrasound attenuation (dB/cm)
= 0.6 - 0.00012H - 0.00226×(37 - T)	1584 (37°C)	2.55 (10 Mhz, 37°C)
H: haematocrit % T: temperature °C	temperature coefficient: 2.0 m/s°C^{-1} (29 ~ 40°C)	1.92 (4.5 ~ 4.8 Mhz, 37°C)

4.2.3 Optical properties

The optical properties of blood depend chiefly on erythrocytes, whose refractive index is about 1.402. Since the corresponding value for plasma is 1.334, the refractive index of whole blood (42% Hct) is 1.362. Besides concentration, the shape, moving velocity, aggregation and sedimentation of erythrocytes have a strong effect on the optical properties of blood [108]. Under normal conditions, an erythrocyte has a characteristic flat biconcave shape with a diameter of 7 to 9 µm and a thickness of 2 µm. This shape offers a high surface area/volume ratio, which enhances the exchange of gases. The high elasticity of the erythrocyte membrane permits it to penetrate capillaries with smaller lumina than the erythrocyte's diameter. The osmolarity of the erythrocyte membrane changes the cell's shape and content ratio, which may affect its optical parameters.

Factors affecting the optical properties of blood were systemically studied by Roggan et al [109], including haematocrit, flow, osmolarity, haemolysis and oxygen saturation. The optical parameters may be calculated with the inverse Monte Carlo method by applying the double integrating sphere technique, changing the above factors and evaluating diffuse backscattering, total transmission and non-scattered transmission. The results are worthily summarized in Fig. 13 to Fig. 18.
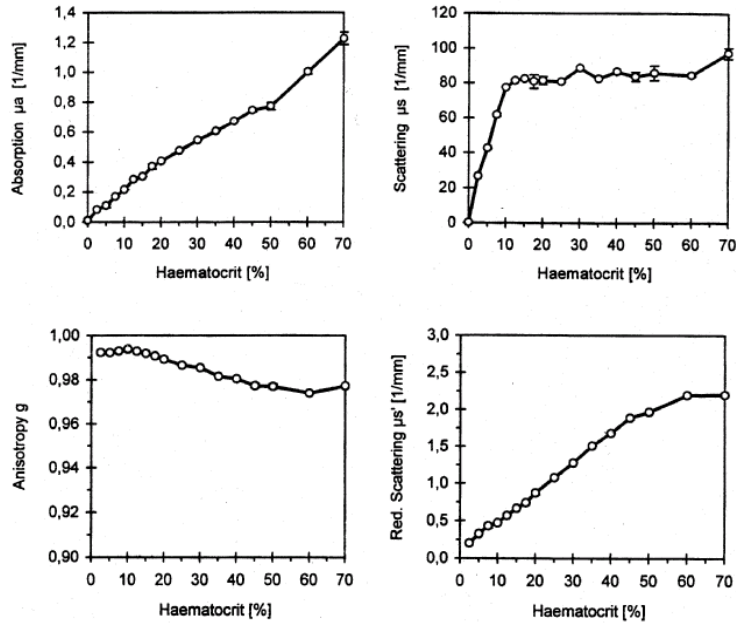
Fig. 13. Mean values ± SD (n = 3) of μ_a, μ_s, g and μ'_s vs. haematocrit (π = 300 mosmol/l, γ = 500 s^{-1}, SatO$_2$ > 98%, λ = 633 nm) [109].
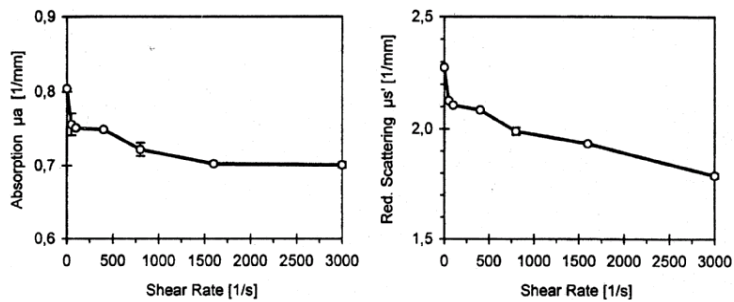
Fig. 14. Mean values ± SD (n = 3) of μ_a and μ'_s vs. shear rate (hct = 41%, π = 300 mosmol/l, γ = 500 s^{-1}, SatO$_2$ > 98%, λ = 633 nm) [109].
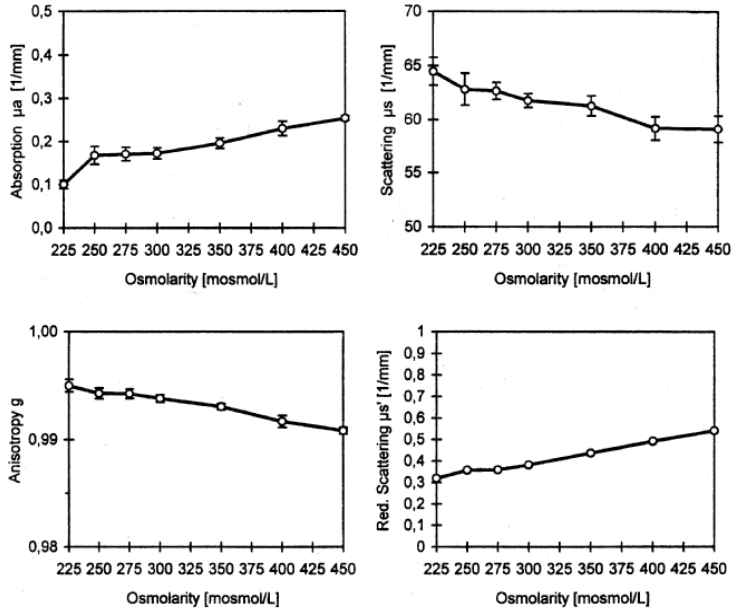
Fig. 15. Mean values ± SD (n = 3) of μ_a, μ_s, g and μ'_s at short flow stop vs. plasm osmolarity (hct = 7.5%, π = 300 mosmol/l, γ = 0 s^{-1}, SatO$_2$ > 98%, λ = 633 nm) [109].
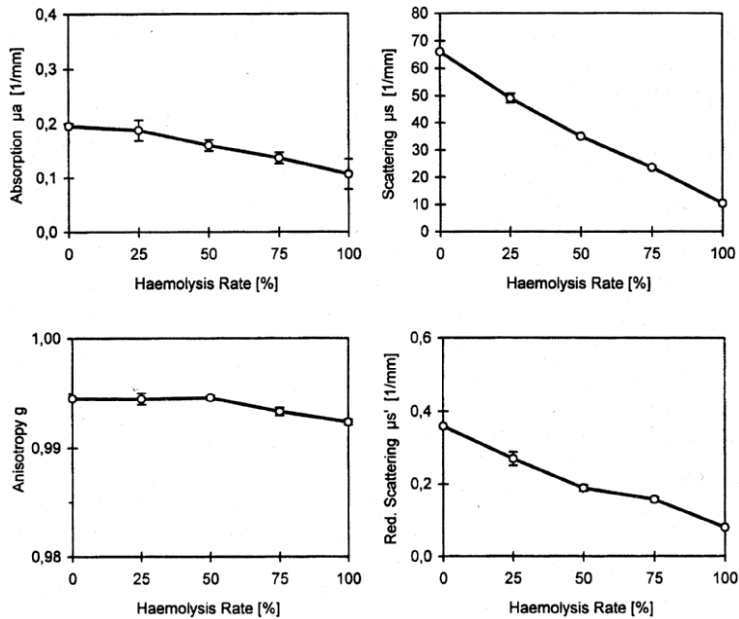
Fig. 16. Mean values ± SD (n = 3) of μ_a, μ_s, g and μ'_s vs. extent of haemolysis (hct = 7.5%, π = 300 mosmol/l, γ = 500 s^{-1}, SatO$_2$ > 98%, λ = 633 nm) [109].
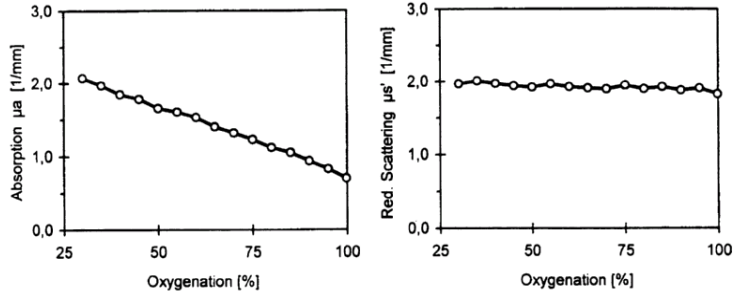
Fig. 17. μ_a and μ'_s vs. O$_2$ saturation (hct = 41%, π = 300 mosmol/l, γ = 500 s^{-1}, λ = 633 nm) [109].

Fig. 18. μ_a of diluted blood and values of μ_s and g which did not vary significantly with oxygenation (hct = 5%, π = 300 mosmol/l, γ = 500 s^{-1}) [109].

5 Simulation of PA source in the skin

5.1 Incident optical distribution in the skin

In the skin, the optical distribution of light varies depending on wavelength and the skin's optical properties. Being comparable to the size of skin cells, wavelengths in the visible and infrared region cause multiple scattering. In the near infrared, moreover, the scattering coefficient of the skin is much larger than its absorption coefficient. This study considers a collimated light beam at normal incident on a sufficiently thick skin. Assuming that the scattering and absorbing centres are uniformly distributed and neglecting internal light generation by fluorescence, the optical distribution can be described by the stationary radiative transfer equation, when the duration of a light pulse is longer than 10^{-8} s [110].

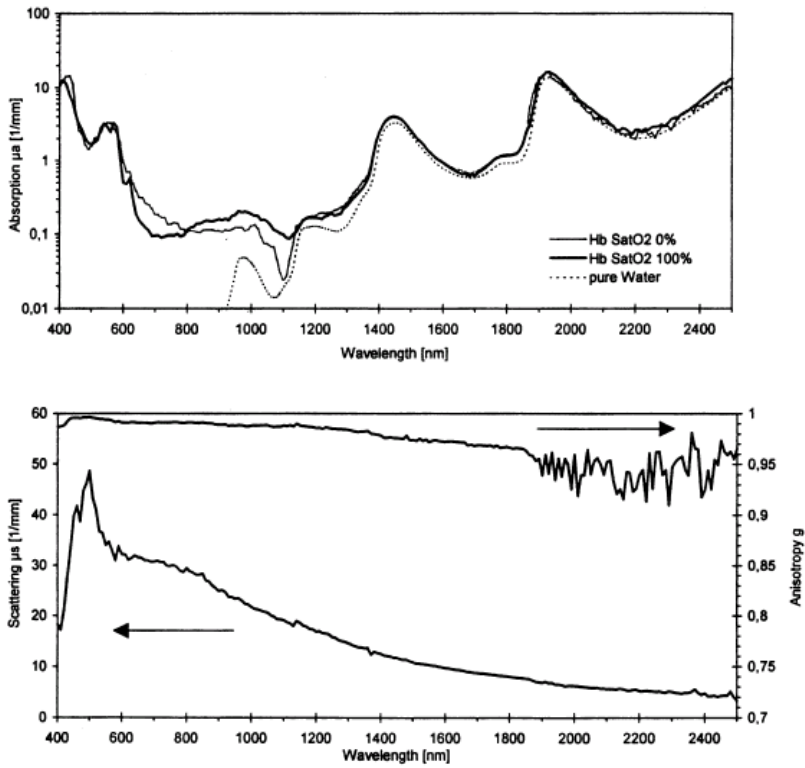$$\boldsymbol{s} \cdot \nabla I(\boldsymbol{r}, \boldsymbol{s}) = -\mu_e\, I(\boldsymbol{r}, \boldsymbol{s}) + \frac{\mu_e}{4\pi} \int_{4\pi} p_f(\boldsymbol{s}, \boldsymbol{s}')\, I(\boldsymbol{r}, \boldsymbol{s}') \mathrm{d}\omega' + \frac{\mu_e}{4\pi}\, p_f(\boldsymbol{s}, z)\, I_c(\boldsymbol{r}, z) \,. \tag{28}$$

The collimated light is attenuated according to modified Beer's law, i.e.

$$dI_c(\boldsymbol{r}, z) = -\mu_e\, I_c(\boldsymbol{r}, z) \cdot dz \,, \tag{29}$$

where $I_c(\boldsymbol{r}, z)$ is the collimated intensity at the position $\boldsymbol{r}$ in the incident direction z, and $\boldsymbol{r}$ is a position vector. $I(\boldsymbol{r}, \boldsymbol{s})$ is the scattered specific intensity (watt/cm^2/sr) at the position $\boldsymbol{r}$ in the direction $\boldsymbol{s}$, and $\boldsymbol{s}$ is the directional unit vector. $P_f(\boldsymbol{s}, \boldsymbol{s}')$ is the phase function that represents the scattering contribution from $\boldsymbol{s}'$ in the direction $\boldsymbol{s}$. ω' is the solid angle. μ_e is the extinction coefficient defined as the sum of the absorption coefficient μ_a and the scattering coefficient μ_s. The physical terms on the right hand side of Eq. (28) are the intensity decrease of scattered light by absorption and scattering, intensity increase owing to scattering from other scattered light, and intensity increase owing to scattering from collimated light, respectively. Even though the radiative transfer equation provides an accurate description of light distribution in turbid media, there is no general solution. It is, however, possible to obtain numerical and approximate solutions for different situations.

When μ_a is much larger than μ_s, the scattering effect can be neglected and Eq. (29) degenerates into Beer's law describing the distribution of light in a purely absorbing medium. The intensity of light in such media decreases exponentially with increasing depth. This corresponds to the propagation of UV or IR light in the skin. The other extreme is the case of strong scattering, where μ_s is much larger than μ_a. This occurs when the skin is illuminated by a laser with a wavelength in red or shortly near infrared region. The transfer equation can be approximated by a diffusion equation. This diffusion approximation assumes that light is scattered almost uniformly after numerous scattering events. As a consequence, the equation does not provide an accurate description of scattering near the incident boundary of the medium. Between the two extremes described above, i.e., when μ_s is of the same order as μ_a, no simple solution or approximation exists for the radiative transfer equation. The problem can be solved, however, by using some numerical approaches. The Monte Carlo simulation offers a flexible and yet general and rigorous approach to photon transport in turbid media, including strongly scattering media.

5.2 Optical model of the skin at near-infrared wavelengths

Noninvasive skin measurements require that the laser wavelength be in the diagnostic and therapeutic window for human tissue, i.e., in the near-infrared spectroscopic range. The 904 nm wavelength is particularly interesting, because the optical penetration in the skin close to this wavelength is the deepest and the commercial laser diodes irradiating at this wavelength emit a higher output power.

Chapter 4 described the physical structure of the skin consisting of the epidermis, dermis and subcutaneous fat. The dermis can be further divided into two layers: stratum papillaris and stratum reticularis, of which the former is especially rich in capillaries. Muscles usually sit under subcutaneous fat. Hence, our optical model of the skin comprises five layers, as shown in Fig. 19. Excluding the muscle layer, the chosen thickness of every layer is 0.2 mm, 0.2 mm, 1.5 mm and 0.3 mm, in accordance with reference [97]. For the sake of simplicity, it is assumed that the every layer is homogeneous and muscles have semi-infinite slab geometry.

The presented optical model of the skin ignores the presence of melanin in the epidermis, thereby enabling light to penetrate the skin effectively. This is reasonable as far as the skin on a human finger is concerned. The optical parameters of a melanin-free epidermis are similar to those of bloodless dermis, which is 0.025 mm^{-1} of the absorption coefficient (shown in Fig. 7 or [111]), 0.9 mm^{-1} of the reduced scattering coefficient (shown in Fig. 10 or [100]), and 0.9 of the anisotropy factor (g = $0.62 + \lambda \times 0.29 \times 10^{-3}$, where λ is in nm, [112]). As the volume fraction of blood in the skin is about 2% to 6% [113], the skin model adopted here sets the value at 4%. The absorption coefficient of blood is about 0.7 mm^{-1} at 904 mm (shown in Fig. 7 and Fig. 13). Moreover, assuming that blood is homogeneously distributed in the stratum papillaris, the resulting absorption coefficient is 0.053 mm^{-1}. The scattering coefficient of blood can be determined from Fig. 13and Fig. 18. The refractive index of every layer and the parameters of fat and muscle are cited from reference [114]. All parameters of the skin model are listed in Table 7.
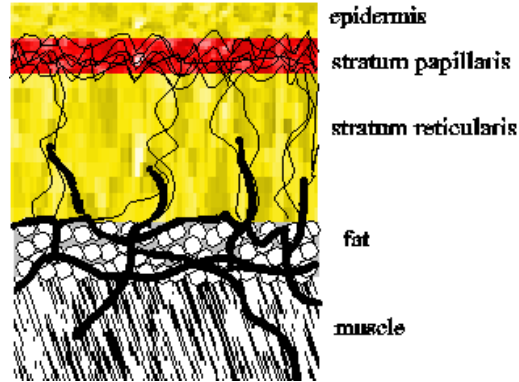
Fig. 19. A skin model.

Table 7. Parameters of the skin model.

	μ_a (mm^{-1})	μ_s'(mm^{-1})	g	n	t (mm)
epidermis	0.025	0.9	0.9	1.5	0.2
papillaris dermis	0.053	0.93	0.9	1.4	0.2
reticulars dermis	0.025	0.9	0.9	1.4	1.5
subcutaneous fat	0.0112	1.08	0.9	1.44	0.3
muscle	0.032	0.59	0.9	1.37	10

5.3 Simulation of the PA source in the skin

5.3.1 Monte Carlo method

The Monte Carlo method, simulating photon propagation in turbid media that are readily described by radiative transport theory, is based on the stochastic nature of radiation interactions and relies on calculating the propagation of a large number of photons, where each photon is depicted as a particle and its waveform is ignored. The medium is divided into a great number of small cells, whose macroscopic optical properties are assumed to be uniform. The photon is continuously scattered as it propagates until it is absorbed by, reflected from, or transmitted through a medium. Comparing with diffusion theory, it is not limited by such optical parameters as the albedo (μ_s/μ_e) and the anisotropy factor g; it is a rigorous and powerful tool.

A Monte Carlo modelling of light transport in a multi-layered tissue was developed by Wang and Jacques [115]. A photon packet was launched into the tissue, where it was subsequently absorbed, scattered, reflected at or transmitted through tissue boundaries or

multi-layered interfaces. It was terminated, if it reflected or transmitted out of the tissue. After a number of interactions, the photon weight of a photon packet that was still propagating in the tissue would drop below a threshold value. A proper termination technique known as the roulette was used to ensure the conservation of energy without skewing the distribution of photon deposition. If the photon's weight dropped below a threshold level and did not survive the roulette, the weight was reduced to zero and the photon was terminated. Then, a new photon packet was launched into the tissue and the same record-keeping procedure was iterated. The Monte Carlo simulation is capable of scoring multiple physical quantities simultaneously.

5.3.2 Simulation parameters and results

If the irradiated energy is vertically incident on the skin surface, the distributions of physical quantities such as fluence and heat generation rate are symmetrical to the axis of the incident light. A cylindrical co-ordinate is set up with the origin at the centre of the point of incidence and the z-axis is directed into the skin. The size of each grid element is chosen as 50 μm in the z direction and 30 μm in the r direction (along the skin's surface), where the number of grid elements in the two directions is 200 and 300, respectively. The total number of photon packets to be traced is 1000000. The incident energy beam is assumed to show a Gaussian distribution in the r direction. The simulation program was written by Wang and Jacques [115]. In the simulation, the total incident energy is set at 1 J, the convoluting resolution and the number of input points in the r direction equal those of the grid elements, and the relative convolution error is chosen as 0.01. The $1/e^2$ radii of the incident beams are chosen as 100 μm and 6 mm, to enable comparisons between distributions produced by narrow and wide beams.

The simulation results and the contour lines of absorbed energy in the z-r symmetrical plane in the skin model are shown in Fig. 20 and Fig. 21 for a narrow and a wide beam, respectively. Although the results are obtained from a steady-state situation, they also apply to a pulsed laser, provided its pulse duration ranges from a few nanoseconds to sub-microseconds, because in this pulse duration the time-resolved distribution of light resembles the steady-state distribution in tissue. If the non-radiative relaxation procession is the main mechanism of energy transformation, the absorbed photon energy is converted to heat, which causes a thermal expansion, and produces a PA source in the absorbed region. As a result, the distribution of absorbed energy corresponds to the shape of the PA source (or acoustic transmitter in the skin), which, apparently, is the rotation body of contour lines representing absorbed energy around the z-axis.

The maximal intensity in the PA source is located on a portion of the z-axis that is in the papillary dermis, not at the surface of the skin. This is mainly because the maximal absorption coefficient of the papillary dermis is just under the epidermis. As shown in Fig. 20, a narrow laser beam produces a cylindrical PA source less than a few sub-mm from the skin's surface. For a wide laser beam, as depicted in Fig. 21, the situation is slightly more complicated. Intensity distribution in excess of e^{-2} is divided into two parts (due to the low absorption property of subcutaneous fat) and its depth can be up to a few millimeters into the skin. However, the portion of the intensity distribution of the PA source that exceeds e^{-1} is located within or near the papillary dermis forming a plane

shape. Hence, the PA source produced by a wide laser beam contains more information about deeper skin layers. A more detailed discussion about the relationship between the radius of the laser beam, the depth of the PA source and the transverse resolution of a PA diagnosis can be found in Paper III.
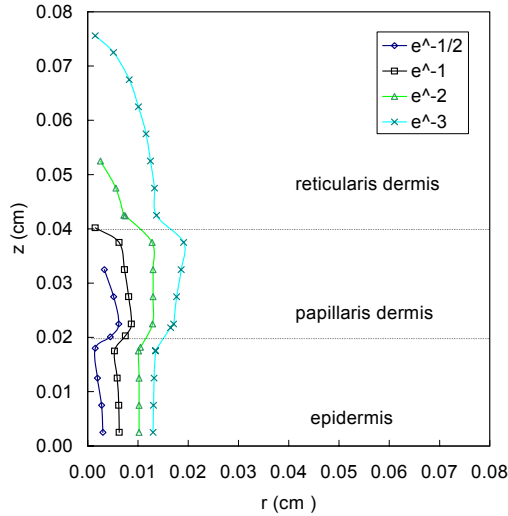

Fig. 20. Contour lines of absorbed energy in the skin model, in the case of a narrow incident beam (the $1/e^2$ radius of the incident beam is equal to 0.01 cm).
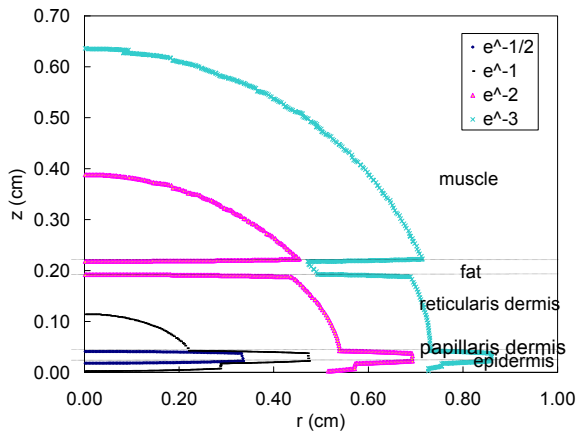

Fig. 21. Contour lines of absorbed energy in the skin model, in the case of a wide incident beam (the $1/e^2$ radius of the incident beam is equal to 0.6 cm).

6 Time-resolved stress detection

6.1 Introduction

The PA techniques presented in Chapter 3 can be employed to determine the average absorption coefficient and trace concentrations in liquid media, merely based on measuring the stress amplitude. In this chapter, a more powerful photoacoustic technique, time-resolved stress detection (TRSD) has been developed, which can rebuild the absorbed optical distribution in studied media by simultaneously detecting the laser-induced stress amplitude and profile. This can be used to measure the absorption and scattering coefficients together and to image the interior structure of turbid samples. Current technological advances in wideband piezoelectric transducers and fast-digitising oscilloscopes have permitted the development of a TRSD technique with excellent temporal resolution. The main TRSD-based biomedical applications include tissue diagnostics, such as the determination of optical properties and photoacoustic tomographic imaging, and light dosimetry during laser treatments.

The core of the TRSD technique is to reconstruct the initial stress distribution in media. This distribution is similar in profile to the distribution of either optical absorption (in purely absorbing media) or effective optical attenuation (in turbid media). A simple case is that a plane PA source produced by a short optical pulse has an exponential relation with the optical absorption coefficient or the effective attenuation coefficient. In planar PA source, it only considers the longitudinal (z-axial) distribution of thermo-elastic stress, thereby rendering the problem one-dimensional.

To produce a planar PA source, the diameter of the incident beam should be much larger than its optical penetration depth in the studied object. Since the effective attenuation coefficient of a typical soft tissue equals 1 or 2 cm^{-1} in the near-infrared region, the laser beam's diameter has to range from a few millimetres to a centimetre. Current diode lasers does not satisfy this demand, due to their limited optical power output. As a result, the most common type of optical source in near-infrared TRSD is a pulsed Q-switched Nd:YAG laser.

To maintain the profile similarity between the initial stress and the following optical absorption distribution, the duration of the laser pulse is usually in the order of 10 ns.

This means that the produced acoustic wave has a frequency component of more than a few tens MHz in media characterized by strong optical attenuation. Hence, the acoustic transducer used for receiving signal should have a fast response time and a bandwidth in excess of a few tens MHz. Thus, a common choice of detector is either a PVDF or a LiNbO$_3$ transducer.

Although posing strict requirements for the laser source and the detector, TRSD offers some apparent advantages. In the study of heterogeneous and layered media, it can detect the distribution of the absorbed optical energy in every layer, whereas traditional PA methods only give an averaged optical value. Moreover, TRSD is capable of measuring the absorption and the attenuation coefficient by a single laser pulse; the dynamic range can be larger than 10^3 for attenuation and 10^4 for absorption. In PA imaging, its longitudinal resolution can be up to 10 µm, and its transverse resolution can be of the order of one mm (depending on the laser beam's diameter). In addition, the technique enables noninvasive and *in vivo* measurements and imaging. Finally, it is worth pointing out that the limitation in the dynamic range of TRSD is not imposed by the method itself, but arises out of technological restrictions: the fastest acoustic transducer based on current technology is in the ns range, while the usual size of objects studied in biomedical measurements is in the mm or cm range. The following chapters provide a detailed theoretical description of the TRSD method.

6.2 Laser-induced stress generation

PA generation in the TRSD technique is belonged to the thermo-elastic mechanism discussed in Chapter 3. Short laser pulses allow the most efficient realization of PA generation at a given incident laser fluence. The PA pressure of a planar PA source produced in a clear (non-scattering) absorbing medium by a short laser pulse (δ pulse) can be described by Eq. (18), rewritten as

$$p_a(\tau) = \frac{E_0 \alpha \beta v^2}{2C_P} \{\Theta(-\tau) \cdot e^{\alpha v_a \tau} + R_c \Theta(\tau) \cdot e^{-\alpha v_a \tau}\} . \qquad (30)$$

At initial time ($t = 0$), when the laser incidents on the absorbing medium, Eq. (30) is simplified as

$$P(z) = \frac{E_0 \alpha \beta v^2}{C_P} e^{-\alpha z} = \Gamma E_0 \alpha e^{-\alpha z} , \qquad (31)$$

where the coefficient of ½ is removed, because the initial stress is not divided in two opposite propagation directions. Eq. (31) shows the initial stress distribution, which decreases exponentially along the *z*-axial. It is strictly valid only in the case when the heating process is much faster than the thermal expansion of the medium. Hence, the stress distribution is a redisplay of the heat function, so that it is identical with the distribution of absorbed optical energy.

The situation is different for a turbid medium. Consider a biological tissue whose reduced scattering coefficient μ_s' is much larger than its absorption coefficient μ_a. When

the tissue is irradiated by a wide laser beam, the subsurface fluence $E(0)$ is higher than the incident laser fluence E_0 due to backscattering. Hence, the corresponding stress can be modified as [106]

$$P(0) = \Gamma E(0) \mu_a \qquad (z = 0) , \qquad (32)$$

$$P(z) = \Gamma E_0 \kappa_s \mu_a \exp(-\mu_{eff} z)$$

$$= \frac{1}{2} \Gamma E_0 \mu_{eff} \left(e^{\mu_{eff} l^*} - e^{-\mu_{eff} l^* (2\Delta+1)} \right) \exp(-\mu_{eff} z) \qquad (z > 1/\mu_{eff}) . \quad (33)$$

For optically thickness samples, $E(0) = (1 + 7.1 R_{d\infty}) E_0$, where $R_{d\infty}$ is the total diffuse reflectance. κ_s is the factor that accounts for the effect of backscattered irradiance that increases the effective energy density absorbed in the subsurface. The second row in Eq. (33) comes from Eq. (27).

6.3 Stress relaxation

The duration of the laser pulse discussed in the section above is very short and can be described by the delta function. This satisfies the stress-confinement condition, i.e., stress is limited to the region of thermal elastic expansion and has no time to relax during irradiation. This stress relaxation can be described by the time that the stress wave takes to propagate through the thickness of the irradiated region, i.e.

$$\tau_a = d / v , \qquad (34)$$

where the thickness $d = 1/\mu_a$ in absorption-dominated media and $d = 1/\mu_{eff}$ in scattering-dominated media. The stress-confinement condition is $\tau_a \gg \tau_L$, or $\mu_{eff} v \tau_L \ll 1$ in scattering-dominated media. It needs to be pointed out that the heat diffusion time, defined as the time during which heat escapes from the irradiated region, is much longer than τ_a in many kinds of media (particularly in biological tissues). Therefore, the pressure decrease caused by heat diffusion is negligible in comparison with stress relaxation.

If τ_L is increased such that the requirement of the stress-confinement condition is not satisfied, the laser-induced stress is significantly relaxed, resulting in a corresponding decrease in the stress amplitude. By further increasing τ_L to $\mu_{eff} v \tau_L \geq 1$, the stress amplitude continues to decrease and the stress shape apparently broadens. The actual acoustic pulse profile produced by a finite laser pulse duration τ_L can be calculated by the convolution of the initial stress distribution (for example, Eq. (33)) and the temporal profile of the laser pulse $L(t)$, i.e.

$$P(z, \tau) = \Gamma v \mu_a \kappa_s E_0 \int_0^{\tau_L} L(t) \exp(-v|\tau - t| / d) dt . \qquad (35)$$

The relative stress amplitude $R_\tau(\tau_L)$ can be defined as the ratio between Eq. (35) and Eq. (33), as presented in Fig. 22, provided that the laser pulse profile is a Gaussian function

$$L(t) = \frac{1}{\sqrt{\pi}} \exp\left[-(2t/\tau_L)^2\right] . \qquad (36)$$

Eq. (35) represents the rigid boundary case, whose derivative is the free boundary case [106]. In the latter case, stress relaxation is faster than in the former. This is because a free boundary can expand in two directions. Effective expansion occurs toward the free surface and is much less significant in the opposite direction. In contrast, a rigid boundary can only expand in one direction.
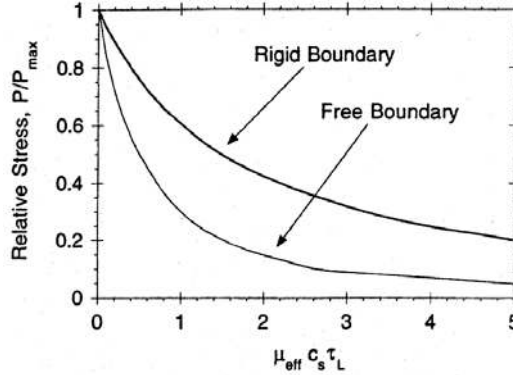
Fig. 22. Relative stress amplitude R_τ vs. the confined stress parameter $\mu_a v \tau_L$ [106].

6.4 Acoustic-wave diffraction

The principle of wave mechanics states that an acoustic wave propagating in media will diverge due to diffraction. Thus, diffraction plays an important role in the dissipation of acoustic energy, increasing the effective area, decreasing the amplitude and changing the profile of the wave. This profile change includes wavefront and waveform changes.

6.4.1 Wavefront Distortion

Wavefront distortion takes place mainly in the plane component of an acoustic wave. When the beam radius R_b of a laser pulse produces a plane sound wave with a wavelength λ_a, the acoustic pressure along the beam axis z is described by [116]

$$p(z) = \left| p(0) \cdot 2 \sin\left\{ \frac{\pi}{\lambda_a} \left(\sqrt{R_b^2 + z^2} - z \right) \right\} \right|$$

$$= \begin{cases} P(0) \cdot 2\sin\left(\dfrac{\pi R_b}{\lambda_a}\right) & (z \ll R_b) \\[3mm] P(0)\dfrac{\pi R_b{}^2}{\lambda_a}\dfrac{1}{z} & (z \gg R_b{}^2 / \lambda_a) \end{cases} . \qquad (37)$$

The amplitude of the acoustic wave holds constant in the near field, which is a characteristic property of a plane wave. In the far field, on the other hand, the amplitude of the wave decreases with z^{-1} and the wavefront is converted into a spherical form. The region of transformation is near z_D ($\sim R_b{}^2/\lambda_a$) from the acoustic source, where $R_b > \lambda_a$. As a consequence, a sound wave produced by a laser beam with a small radius R_b in a medium with a small μ_{eff} (large λ_a) is easily diffracted and distorted (corresponding to a small z_D). The plane wave diverges into a spherical region whose apex is in the centre of the source. The half apex angle θ_h is described by $\theta_h = \arcsin(R_b/z_D)$.

6.4.2 Waveform Distortion

Terzic [117] and Sigrist [82] have discussed the waveform distortion of the temporal shape of a plane acoustic wave in water ($\alpha^1 \ll v\tau_L$) and in n-heptane ($\alpha^1 \gg v\tau_L$). The theoretical calculations for both liquids are in good agreement with actual experimental results. These results can be described as follows:

In the case of rigid boundary condition, diffraction produces a rarefaction wave with a growing amplitude behind the pure compression pulse; in other words, a monopolar pulse becomes bipolar. The waveform steepens slightly and its amplitude decreases with increasing propagation distance.

In the case of free boundary condition, diffraction also produces another compression pulse with increasing amplitude that follows the original compression/rarefaction wave; in other words, a bipolar pulse becomes tripolar. The ratio between the compression and rarefaction peaks decreases and the waveform steepens slightly.

Owing to the same physical mechanism, diffraction produces similar effects in cylindrical and spherical waves; i.e., the initial bipolar acoustic pulse becomes tripolar, the waveform steepens, all amplitudes decrease and the ratio between the compression and rarefaction amplitudes decreases. This is confirmed by the experiments reported in references [83] [118] and [119], where the author of [83] concludes that the third wave peak results from a very slight vaporisation of the liquid. It is more likely, however, that the third peak is produced by diffraction.

6.4.3 Diffraction factor

The effect of acoustic diffraction on stress amplitude can be expressed as a parameter known as diffraction factor, which is defined as the ratio between the effective acoustic wave area on the surface of a medium (equal to a laser beam area A_L) and the acoustic

wave area A_a on the detecting surface at the depth z. If we set $z_D = 2R^2/\lambda_a$ and consider θ_h = arcsin(R_b/z_D), the diffraction factor can be deduced as

$$D = A_L / A_a = 1 / \left(1 + \frac{z}{z_D}\right)^2 = \left(1 + z\frac{\lambda_a}{2R_b^2}\right)^{-2} = \left(1 + z\frac{v}{2R_b^2 f_{ac}}\right)^{-2}. \quad (38)$$

If $D = 1$, there is no diffraction. Fig. 23 showed the diffraction factor as a function of the laser diameter $2R_b$ and acoustic frequency f_{ac}. The experimental points were obtained from a 10-mm thick sample of aqueous potassium chromate, and the sensitive area of the LiNbO$_3$ acoustic detector was 1 mm^2 [106]. The theoretical curves agree well with the experimental points, except in the case of strong diffraction (a small laser diameter and low acoustic frequency), where laser–induced transient stress covers a wide spectrum of acoustic frequencies. This is because low frequency components disappear quickly due to diffraction while higher frequency components decrease slowly.
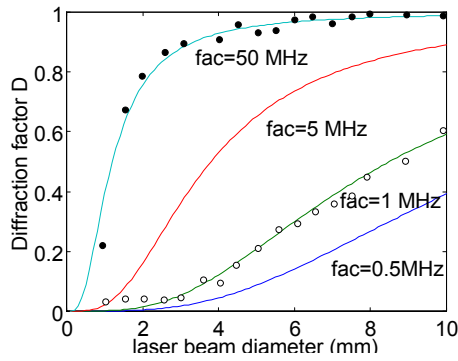
Fig. 23. Diffraction factor D vs. the laser beam diameter for different acoustic frequencies (dots are experimental results in [106]).

Hence, low frequency acoustic waves are significantly affected by diffraction, which dissipates their acoustic amplitude and alters their wave profile. To reconstruct the distribution of heat in a medium by an acoustic wave, it is necessary to avoid diffraction-induced changes in the acoustic profile of the wave during propagation. This calls for a diffraction factor within the region of 0.4 to 1, in which range the alteration of the acoustic profile has been found minimal. However, the typical photoacoustic frequency in near-infrared biological tissue measurements may vary from 0.5 to 10 MHz. This means that the diameter of the laser beam should be wider than a few millimetres, as seen in Fig. 23. As a consequence, the limited output power of diode lasers makes them unsuitable for the task.

6.5 Acoustic-wave attenuation

The absorption and scattering of acoustic waves will decrease the amplitude and alter the profile of the initial waves. In a uniform and static liquid, attenuation is mainly caused by acoustic absorption. The absorption of sound in a liquid is the result of the liquid's viscosity and heat conduction ability. Usually, it is convenient to sum acoustic absorption and scattering into a single parameter, referred to as the attenuation coefficient α_{ac}. If the initial plane stress distribution produced in a medium is marked by $P_0(z)$, the profile of the acoustic wave which propagates a distance d along the z-axial can be described by

$$P(z) = P_0(z)\exp(-\alpha_{ac}d) = \Lambda P_0(z) \tag{39}$$

where Λ is the acoustic attenuation factor. The acoustic attenuation coefficients of most bio-tissues and liquids are summarized in [104]. For most liquids, α_{ac} is proportional to the square of the frequency in the range of 3 ~ 100 MHz. The attenuation of an acoustic wave in pure water can be calculated as α_{ac} (cm^{-1}) = $2.5 \times 10^{-4} f_{ac}^2$, the unit of frequency f_{ac} being MHz. At lower acoustic frequencies, liquids have a slightly higher attenuation than might be expected on the basis of the f_{ac}^2 law. In the frequency range between 10 kHz and 1 MHz, the attenuation coefficient is about $0.5 \sim 1.5 \times 10^{-3}$cm^{-1}. For many soft tissues, $\alpha_{ac} \propto f_{ac}$, and when the acoustic frequency reaches 1 MHz, $\alpha_{ac} = 0.01 \sim 0.05$ cm^{-1}. In near-infrared PA tissue measurements, the PA frequency varies from a few hundreds of kHz to a few MHz. If the detection distance is shorter than a few centimetres, acoustic attenuation can be neglected ($\Lambda \approx 1$). However, in other medical applications, the acoustic frequencies can be in the range of 10 ~ 75 MHz, where attenuation becomes pronounced.

It must be pointed out that pulsed PA generation covers a wide spectrum range. When a PA wave propagates, its higher frequency components are attenuated more than the lower ones because of the acoustic attenuation coefficient correlating positively with acoustic frequency. Hence, in addition to decreasing the amplitude of an acoustic wave, attenuation will also alter its acoustic profile. This effect usually broadens the acoustic pulse, thereby attenuating the higher frequency components even further. Fortunately, in most tissue measurements by near-infrared TRSD the acoustic frequencies are lower than a few MHz, rendering the acoustic profile alteration due to attenuation negligible.

6.6 Non-linear Effects of Sound

The mechanism causing non-linear effects is based on the increase of sound velocity with a strong acoustic pressure p [82]

$$v' = v + \frac{p}{\rho v} + \frac{B/A}{2}\frac{p}{\rho v}, \tag{40}$$

where B/A is Beyer's non-linear coefficient.

In practice, diffraction and non-linear effects exert a simultaneous influence on the waveform of sound waves. Sigrist [82] describes the net influence of non-linear effects on waveforms. He splits a laser pulse into two equal parts and attenuates one of them by a

factor of 15. The two laser pulses generate two acoustic waves with different pressure amplitudes. The results indicate that after propagating over the same distance, the waveform produced by the laser pulse with the larger amplitude is steeper. Waveform distortions caused by diffraction depend on the propagation distance, and are not proportional to the initial pressure amplitude. Hence, the difference between the acoustic amplitudes produced by the two laser pulses represents the net non-linear effect, causing a steepening of the acoustic waveform.

There are several methods for reducing the waveform distortion caused by non-linear effects. These methods include shortening the acoustic propagation distance, improving laser power control and using a liquid with a smaller Beyer's non-linear coefficient. Moreover, non-linear effects are smaller in water than in methanol and ethanol. In weakly absorbing materials, such as bio-tissues irradiated at near-infrared wavelengths, they can be neglected altogether.

In addition, a change in Grüneison coefficient Γ following a temperature rise will produce a thermal non-linear effect. This breaks the linear relationship between the absorbed energy density and the acoustic pressure, and may eventually distort the initial pressure distribution. Hence, keeping the samples´ temperature constant is an important consideration in laser TRSD.

6.7 Acoustic-wave transmission

As explained in Section 3.3.2.1, a laser-generated planar stress wave propagates in two directions: along the axis of the laser beam into the absorbing medium and in the reverse direction toward the transparent medium. The pressure amplitude of the transient stress propagation in each direction equals half of the initial stress amplitude. An acoustic wave propagating through a medium boundary can be partially reflected and partially transmitted through it, depending on the acoustic impedance of the medium. In the same reason, when an acoustic wave is received at the surface of a transducer, it will be partially reflected and partially transmitted through it. When a planar sound wave propagates vertically onto the interface, the transmitted intensity is described by

$$I_t = I_i \frac{4Z_m Z_t}{\left(Z_m + Z_t\right)^2} \, , \tag{41}$$

where I_i is the incident acoustic intensity, Z_t and Z_m are the acoustic impedances, defined as the multiple of density and sound velocity of the transducer material and the propagation medium, respectively. It can be seen that if the impedances match, i.e., $Z_m = Z_t$, I_t is equal to I_i and all incident sound energy is received by the transducer. However, the physical quality measured by the acoustic transducer is the acoustic pressure P, which is equal to $\sqrt{I_a Z_a}$. Hence, transmittance through the receiving surface of the transducer is expressed by

$$T = \frac{P_{tr}}{P_i} = \frac{2Z_t}{Z_m + Z_t} \, . \tag{42}$$

Transmittance in the equation above may be larger than 1 and reach a maximal value of 2 when $Z_t \gg Z_m$. This was demonstrated in an experiment carried out by Oraecsky [106], in which T equalled 1.9 for a stress wave generated in an aqueous solution and measured by a transducer with a germanium conductor. For other piezoelectric materials, the corresponding transmittance are summarized in Table 8:

Table 8. Acoustic impedance and transmittance of piezoelectric materials in water.

	$Z \times 10^6$ (Rayl = kgm^{-2}s^{-1})	Z/Z_w	T
Quartz (x-cut)	11.4	7.6	1.77
PZT-5A	35	23	1.92
PVDF	4	2.6	1.44

The voltage amplitude of the transducer output is equal to

$$U = \frac{P_{tr}}{\sqrt{\kappa_{se} R_r Z_t}}, \tag{43}$$

where κ_{se} is the transfer coefficient of sound-to-electric energy, and R_r is the electric resistance of the transducer.

6.8 Response of acoustic transducers

When an acoustic transducer receives a stress wave, it transfers the wave into an electrical signal. The amplitude ratio of the electrical signal and acoustic pressure is defined as the response S of the transducer, which is a function of piezoelectric material, thickness and area of the transducer, received acoustic frequencies and piezoelectric loading. Typical values are ~ 30 µV/Pa for the PZT transducer made by Tam and Patel [120], ~ 0.1 µV/Pa for the LiNbO$_3$ transducer made by Sigrist [83] or LST Incorporated, and ~ 0.1 µV/Pa for a PVDF transducer (Marconi Y-33-7611). On the other hand, higher response usually trades off narrower bandwidth.

TRSD necessitates the use of a wideband acoustic transducer to reconstruct the initial stress distribution in the medium. Common detectors include PVDF transducers, LiNbO$_3$ transducers and optical sensors. Fig. 24 provided an example of a LiNbO$_3$ transducer response for an ultrasonic frequency range from 0.7 to 140 MHz. It can be seen that S varies at different acoustic frequencies. If the acoustic velocity in the medium is known and the effective optical attenuation in a turbid medium is obtained from the simple exponential fit of the laser-induced stress profile, the centre frequency can be calculated from $f_{ac} = 2v\mu_{eff}$. Thus, the acoustic response can be estimated from Fig. 24. In most soft bio-tissues, the centre acoustic frequency excited by a visible or a near-infrared laser ranges from a few hundred kHz to 10 MHz.
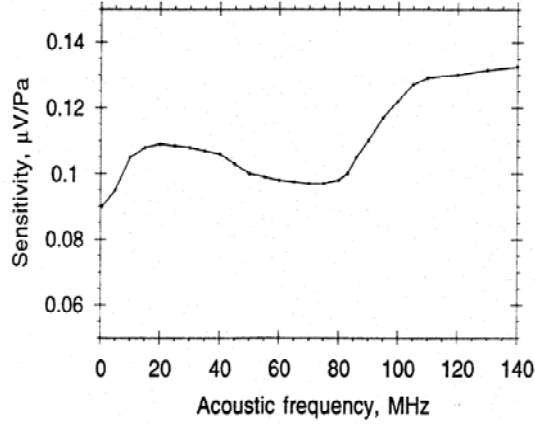
Fig. 24. Response of a WAT-04 LiNbO₃ transducer [106].

6.9 TRSD by acoustic transducers

If an acoustic transducer is to redisplay the initial stress distribution in PA source, it is important that the incident laser beam is perpendicular to the surface of both the sample and the transducer. The centre of the laser beam should be aligned with the centre of the acoustic transducer to avoid detector edge effects. Moreover, the surface of the sample should be as flat as possible to allow the formation of a planar acoustic wave along the axis of the incident laser beam. For a soft tissue, this can be achieved by covering it with a glass plane.

To summarize the main content of the sections above, we may conclude that TRSD by acoustic transducers can be expressed as

$$P(z) = \frac{1}{2} R_\tau D \Lambda T S \Gamma E_0 \mu_{eff} \left(e^{\mu_{eff} l^*} - e^{-\mu_{eff} l^* (2\Delta+1)} \right) \exp(-\mu_{eff} z), \qquad (44)$$

where the non-linear effect is neglected for weak absorption or near-infrared tissue TRSD. It must be noted that Eq. (44) applies to TRSD in a turbid medium such as a soft tissue (transmission mode). If TRSD is performed at the surface of a tissue (reflection mode), a transmission factor of stress from the tissue surface must also be considered.

Before finishing this chapter, it should be pointed out that most of the results described above also hold for other kinds of PA source. If TRSD is applied to a cylindrical PA source, possible applications include measuring the optical distribution of the laser beam and the absorption profile parallel with the laser beam in the sample. In contrast to a plane PA source, the ideal reception position in association with a cylindrical PA source is that the axial of the transducer is vertical to the laser beam in one plane. The detection of a spherical source demands that the axis of the transducer pierces the centre of the source. As a result, the transducer should be mounted as close to the source as possible, while being outside it. Hence, the received wave will exhibit maximal amplitude and minimal profile alteration.

7 PA glucose measurements

In this chapter, the relevantly PA parameters of glucose are studied and measured in Section 7.1 at first. Then, the optical sources and detectors which are usually used in PA measurement and imaging are described in Sections 7.2 and 7.3 respectively. Our PA experimental apparatus is shown in Section 7.4. In Section 7.5, The PA measurements of glucose are carried out in water, milk solution, tissue sample and whole human blood. Moreover, the non-invasive PA experiments at human finger are also done in this section. The measurement results are discussed in the last section.

7.1 Glucose properties

7.1.1 Near-infrared optical absorption in a glucose solution

In the human body, glucose is dissolved in fluids and blood, which both consist mainly of water. Fig. 25 and Fig. 26 display the absorption spectroscopy of glucose solution:
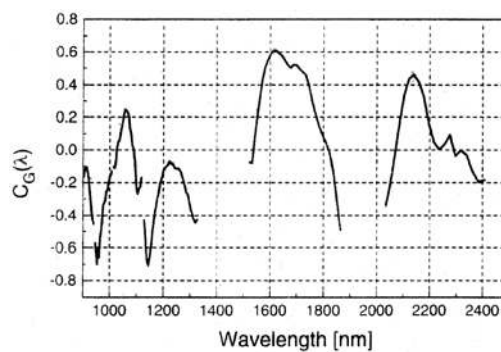

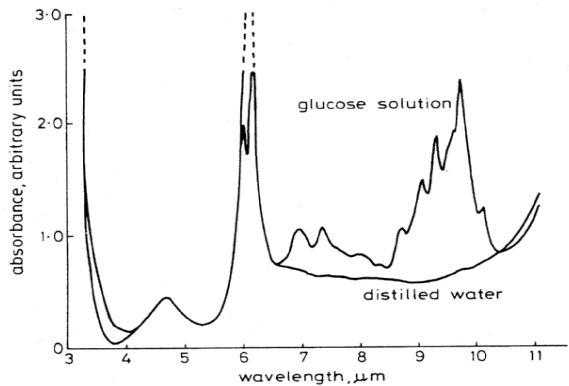**Fig. 25. Near-infrared absorption of 10% glucose solution [121].**

Fig. 26. FT-IR spectra of a glucose solution and distilled water in the middle infrared [76].

It can be seen that absorption is much stronger in water than in glucose at $3 \sim 6.5$ μm, while glucose has higher absorbance peaks at wavelengths between $8.5 \sim 10$ μm. Nevertheless, background absorption caused by water in the mid-infrared region is too distractive to permit non-invasive tissue measurements. In the near-infrared region, however, glucose has relatively large absorption at wavelengths between $1500 \sim 1800$ nm and $2100 \sim 2200$ nm. The background absorption caused by water in tissue is around ~ 1 mm^{-1}, which enables light to propagate a few hundreds of micrometers into the skin. This propagation may reach all the way to the dermis, where glucose is dissolved in blood and interstitial fluid. At wavelengths shorter than 1500 nm, the absorption of light in glucose is overshadowed by background absorption in water or the skin, making these wavelengths uninteresting for studies based on the absorption properties of glucose.

7.1.2 Effects of glucose on the reduced scattering coefficient of tissues

As glucose is found mainly in interstitial fluid and blood plasma, changes in glucose concentration may change the refractive index mismatch between interstitial fluid, collagen fibres and cell membranes, producing a corresponding change in the scattering properties of the tissue. It has been demonstrated experimentally at near-infrared wavelengths that the glucose concentration of a tissue correlates with the reduced scattering coefficient. Furthermore, it has been calculated that the reduced scattering coefficient decreases about 3.3% in a tissue phantom [43], $3.6\% \sim 11.2\%$ in clamping tests at the abdomen [44], and even up to 20% in glucose tolerance tests in thigh muscles, [42], provided that the change in the glucose concentration is at the upper level of the physiological range (33 mM). These values are much larger than signal changes detectable by absorption spectroscopy, suggesting that detection sensitivity can be improved by measuring the scattering coefficient or some other scattering-related quality of the tested medium in the near infrared. However, it is not clear whether the change in scattering is mainly caused directly by glucose (matching of refractive indexes) [114] or

by some other agency, such as physiological change, blood circulation, body temperature shift, and so on.

To elucidate an answer to this question, a system comprising a pulsed diode laser with a duration of 30 ps and a wavelength of 900 nm and a streak camera (C5680, Hamamatus) was used to study the scattering effect of glucose in a human blood sample, as explained in Paper VII. The measured temporal dispersion curves showed that glucose precipitated the signal's arrival and caused a narrowing in its temporal width. Both these effects indicate a reduction in the scattering capacity of the sample. Hence, glucose may directly decrease the reduced scattering coefficient of a tissue.

7.1.3 Thermal and acoustic properties

In addition to the optical parameters of a medium, PA generation also affects such thermal and acoustic parameters as the thermal expansion coefficient, specific heat and sound velocity, as described in Chapter 3. These parameters are functions of temperature, but are not associated with the exciting optical source. In this section, thermodynamic methods are used to measure the expansion coefficient and specific heat, using the PA method to measure sound velocity in a glucose solution.

7.1.3.1 Measurement of the expansion coefficient

In this measurement, the test liquid is placed in a pycnometer, whose volume V is about 25 ml at 20 $^{\circ}$C. The pycnometer is held in place by a holder and immersed in a thermostate bath filled with a fluid. The thermostate bath, model GRANT W6-KD/W6-KA, heats and circulates the fluid. The bath also keeps the temperature of the fluid at a definite value with an error margin of less than 0.1 $^{\circ}$C. When the circulating fluid is heated, it transfers the heat to the test sample in the pycnometer. In a matter of a few seconds, the temperature of the sample rises until it equals that of the circulating fluid. The test sample expands accordingly and a glass tube with a volume scale shows the volume change ΔV. If the temperature change of the sample is ΔT, the expansion coefficient can be calculated by

$$\beta = \frac{\Delta V}{V} \frac{1}{\Delta T} . \tag{45}$$

First, the experimental results were calibrated using a test sample of pure water. Table 9 compares our results with those published in [122]. It is evident that the expansion coefficient of water is a function of temperature and our results are always slightly smaller that the published data. This error can be explained by two factors. One is the volume increase of the pycnometer with temperature. The other is that our results represent an average temperature change value, 5 $^{\circ}$C for every experiment. However, if the focus of interest is on the relative change of the expansion coefficient between the solution and water, this error can be eliminated.

Table 9. Physical coefficients of water.

T (^oC)	β ($\times 10^{-6}/^oC$)[*]	β ($\times 10^{-6}/^oC$)	C_P (J/ (g $\times$ ^oC))	v ($\times 10^3$ m/s)
20	196	208	4.1819	1.483
30	288	304	4.1785	1.510
40	379	396	4.1786	1.530

Extract from Table 11-3 in [122]

*: results measured by the author.

Next, glucose solutions with different concentrations were made and then tested as above. The relationship between the relative change of the expansion coefficient and the concentration of the solution at 30 ^oC, is shown in Fig. 27. The linear trendline shows that Δβ/β equals about 1.2% per percent change in glucose concentration.
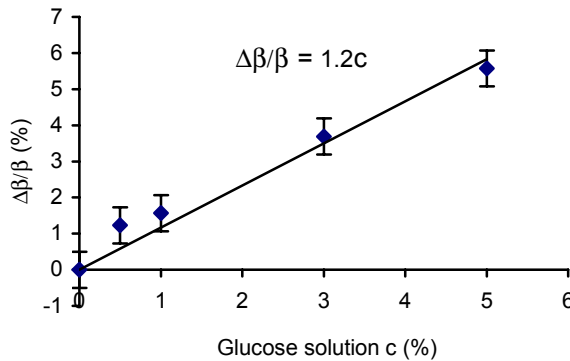
Fig. 27. Relative change of the expansion coefficient with glucose concentration.

7.1.3.2 Measurement of the specific heat

The accurate measurement of specific heat requires special facilities and a highly trained physicist. We designed a simple apparatus to measure the average specific heat of a glucose solution in the region of room temperature. The sample solution was loaded in a vacuum flask, which was heated by a heating resister immersed in it. A mechanical mixer was employed to maintain a homogeneous temperature, measured by a thermometer. The experiment was controlled by a computer.

In this experiment, the computer set a start temperature, a temperature change ΔT and a heating voltage. When the temperature of the sample equalled the start temperature, the computer began to record the electrical energy Q_E dissipated in the heater. If the sample weight is m, the total energy Q_t absorbed by the sample is equal to Q_E and the temperature rise in the sample is ΔT, the specific heat can be calculated by

$$C_p = \frac{Q_E}{m \cdot \Delta T} \ . \tag{46}$$

There were two kinds of sample: a pure water sample and a glucose solution with different concentrations. Every sample weighed 200 grams. The start temperature was set at 20 $^{\circ}$C, the temperature rise was 20 $^{\circ}$C and the voltage across the electric heater was 25 volts. The mixer was driven by a DC electrical supply at 0.8 volts. First, the pure water sample was measured to calibrate the later results.

The measured specific heat of water was about 4.7 J/(g $^{\circ}$C), which is larger than the previously reported value of 4.18 J/(g $^{\circ}$C). This error can be accounted for by two reasons. One is the escaped heat energy Q_e from the vacuum flask. The other is the heat energy Q_a absorbed by the mixer, heater, detecting head of the thermometer and air in the flask. Thus, the energy required to heat the sample Q_t is actually equal to Q_E - Q_e - Q_a. In the C_P measurement above, Q_e and Q_a were ignored so that the measured C_P is larger than the calculated value from Eq. (46).

Measuring Q_e and Q_a is a rather complicated affair. Fortunately, this thesis is chiefly interested in the specific heat change ΔC_P between the glucose solution and the water. This simplifies matters, because Q_a does not vary among the different samples. Q_e is a function of heating time and the temperature difference on the inside and outside of the flask, which can also be assumed to be nearly identical for all samples. Thus, Q_e and Q_a can be cancelled in the calculation of ΔC_P, as shown by

$$\Delta C_P = \frac{Q_{ts} - Q_{tw}}{m \cdot \Delta T}$$
$$= \frac{Q_{Es} - Q_{Ew}}{m \cdot \Delta T} \ . \tag{47}$$

The lowercase s and w indicate the variables for the glucose solution and water, respectively. Having obtained ΔC_P, we divide it by the C_P of pure water, 4.18 J/(g $^{\circ}$C), not by the measured value of 4.7 J/(g $^{\circ}$C). The results are drawn in Fig. 28. The linear trendline shows that the specific heat of the glucose solution decreases about 0.6% for a percent concentration change.

The error in Fig. 28 is produced by six factors. First, the heating time between the glucose solution and the water sample varies slightly, so that Q_e is not cancelled exactly in Eq. (47). Second, the instability of heating power also causes a difference in the heating time. Third, the temperature in the flask is not really homogeneous. Thus, the temperature measured by the thermometer only represents the reading at the detection point. Fourth, a weight error exists between the test samples. Fifth, the error of ΔT, about 0.1 $^{\circ}$C, arises from the thermometer. Sixth, the minimal heating time controlled by the computer, 1 second in our experiment, causes an error in Q_E. An appropriate choice of heating power, ΔT, sample weight and the relative positions of the heater, mixer and thermometer serve to decrease errors resulting from the last four sources.
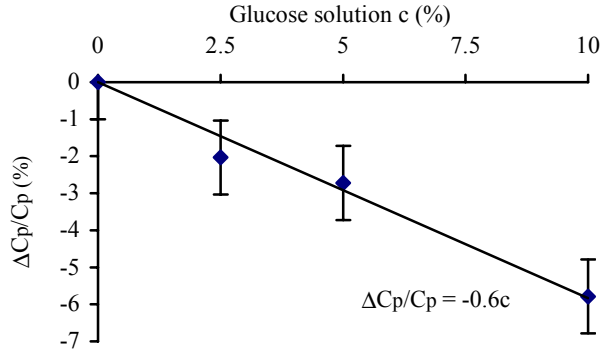
Fig. 28. Relative change of specific heat with glucose concentration.

7.1.3.3 Sound velocity in glucose solutions

One application of the PA technique is the measurement of sound velocity in a medium. Using the experimental PA apparatus described in Section 7.4, sound velocity was measured in pure water. Moving the PZT transducer by 13 mm causes a delay of 8.69 µs in the receiving time. Taking account of a distance error of ±0.01 mm established by a micromanipulator and a time error of ±0.02 µs shown by an oscilloscope, we get the sound velocity of $(1.496 \pm 0.009) \times 10^3$ m/s. This value agrees very well with the published data in Table 9.

Then, glucose solutions were prepared and acoustic changes in their concentrations were measured. Having fixed the position of every component in the apparatus, the pure water and glucose solutions were injected into the PA cell. The measurements were performed in the following order: water, followed by a low concentration glucose solution and a high concentration solution. The relative change of sound velocity can be expressed by

$$\frac{\Delta v}{v} = \frac{v_s - v_0}{v_0}$$
$$= \frac{t_0 - t_s}{t_s} \tag{48}$$

The lowercase s and 0 indicate the relative parameters of solution and the water. It can be seen that $\Delta v/v$ is a function of propagation time only. The time is determined at the first peak of the PA wave. Table 9 indicates that the velocity of sound is affected by the temperature of the propagation medium. The experiments were carried out at room temperature, so the ambient temperature may be assumed identical for all samples, as they were measured in the course of a few minutes. The measurement results are shown in Fig. 29, in which the error is due to the limitation of time resolution of the oscilloscope. The linear trendline gives a relative change of 0.28% in sound velocity for a
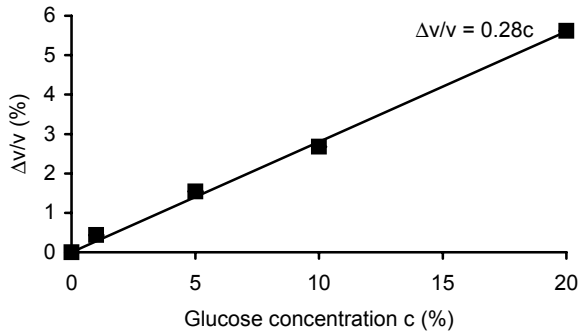
percent change of glucose concentration.

Fig. 29. Relative change of sound velocity with glucose concentration.

7.2 Laser sources

PA waves can be generated by any radiation energy source with a short duration. Thermoelastic generation, however, requires a high power radiation source, due to the low efficiency (< 0.0001) of optical to acoustic transformation. Pulsed laser sources have some advantages over continuous-wave modulating sources in terms of PA techniques. First, pulsed lasers offer a higher detection sensitivity owing to their high output power producing a correspondingly strong PA signal. The high frequency PA signals produced by pulsed lasers are easy to separate from the low frequency noise in the environment, resulting in a low noise level. Furthermore, the use of timing gates is a very efficient technique for getting rid of noise signals produced by the absorption and light scattering from other parts of apparatus. Secondly, in spite of their high output power, pulsed lasers are free of convection currents and, owing to their low duty cycle, they are immune to the spurious effect caused by sample heating. Avoiding sample heating is an important consideration for some applications. Thirdly, unlike continuous-wave lasers, PA signals generated by pulsed lasers exhibit no complex dependence on the thermal diffusion length and chopping frequency. And, finally, narrow banding the laser with intra-cavity etalons enables high-resolution studies.

Various kinds of gases, solids, semiconductors and dye lasers have been used in PA spectroscopy and photoacoustics. In recent years, near-infrared laser sources such as the Nd:YAG laser and the diode laser have been widely used in PA research in biomedicine and environmental protection. These devices allow the study of the internal properties and structure of weakly absorbing materials in the near-infrared region, including aqueous substances and most bio-tissues.

7.2.1 Q-switched Nd:YAG laser

In the Nd:YAG laser, Nd^{3+} ions are embedded in the solid matrix of an yttrium aluminum garnet ($Y_3Al_5O_{12}$). Laser action is induced by the level transitions of the Nd^{3+} ions. Usually, a flashlamp is used for pumping the laser in the high power pulsed operation at a transition wavelength of 1.06 μm. If the peak power of the pulse is sufficiently high, a suitable crystal can be used to generate the second and third harmonic at 532 nm and 355 nm, respectively. The output energy is usually on the order of mJ and can reach the order of sub-Joule, where the pulse duration ranges from a few nanoseconds to a few hundreds of nanoseconds. Moreover, other wavelengths, for examples, 436nm and 461 nm, can be produced by applying a Raman shifter to the output of the laser [123].

At the shorter end of the near-infrared region (700 nm ~ 1200 nm), the optical absorption of aqueous samples and most bio-tissues is low, and light can penetrate into the human tissue to a depth of a few millimetres or centimetres. This is very useful for non-invasive imaging and diagnostics. Because the output energy of the Q-switched Nd:YAG laser is fairly high, the laser beam can be expanded to the centimetre scale for a time-resolved PA measurement of the optical parameters and internal structure of various tissues [106,124]. The efficiency of the method has been demonstrated in the diagnosis of breast cancer, skin cancer and various other skin disorders and tissue pathologies deep inside the body. Based on the correlation between the reduced scattering coefficient and the glucose concentration of the tissue, the time-resolved PA measurement of tissue optical parameters may be used in non-invasive glucose measurements. The main advantage is improved detection sensitivity (-3%/mM) [79].

7.2.2 Pulsed diode lasers

The diode laser is based on the recombination of electrons and holes in semiconductors and in the associated release of energy in the form of light radiation. The wavelength of the radiated emission is determined by the band gap of the active semiconductor layer. Although the diode laser has some disadvantages such as relatively low output energy and poor directionality, it has a wide application range, due to its lightweight, small volume, high efficiency, low price and easy compaction. With wavelengths in the near-infrared and middle-infrared region, current diode lasers can be very useful in biomedical applications and environmental monitoring.

The advance direction of a diode laser is toward to reduce the threshold current density and the linewidth of the lasing emission. A typical structure comprises a double heterostructure and a buried heterostructure in which the active layer takes the form of a narrow stripe of semiconductor material. Many diode lasers have been developed for the needs of optical communications, with wavelengths corresponding to the absorption minima of optical fibbers (880 nm, 1300 nm and 1550 nm). Diode lasers emitting at other wavelengths have also been made available in recent years. However, the output energy of most laser diodes is too weak for PA generation, although some high power pulsed laser diodes listed in Table 10 below are capable of producing a detectable PA signal. These high power laser diodes, driven by peak currents of several Amperes, have a

relatively large volume active region. The output pulses have the duration of one hundred microseconds or more.

Table 10. Commercial pulsed laser diodes with high output energy.

λ (nm)	Manufacturer	Model	Pulse Energy (μJ)	Emitting area (μm × μm)	# of diodes
810	SDL	2100	0.1		1
850	Northem Telecom	LP8M10C	0.2		1
880	Hamamatus	L4356	4.0		1
904	LDP Inc.	LD-163	5.0		3
905	EG&G	PGAS1S24	4.0	600 × 1	1
905	EG&G	PGAF5S16	16.0	400 × 450	5
1300	EG&G	C86045	1.0		1
1550	EG&G	C86091E	0.8	150 × 1	1

Although the low output energy limited the application of laser diodes in PA techniques, there were two published papers involving this possibility. The first one considered monitoring oil contamination in water, and the achieved detection limit was 40 mg/dl [125]. The other attempted building a portable non-invasive blood glucose monitor [77], but did not report clinical results and statistical data.

7.2.3 Tuneable laser sources

The tunability of the laser wavelength plays a significant role in spectroscopic studies as the absorption ability of a material determines the wavelength at which it can best be studied. Several tuneable near-infrared laser sources that may be applied to PA glucose measurements will be described below.

When high power radiation propagates in an optical fibre, the high intensities maintained at the core of the fibre produce a frequency-shifted radiation at a longer wavelength (the Stokes wave) by single-pass stimulated Raman scattering (SRS) [126]. The wavelength shift and the critical pump power depend on the materials used. Pump power is defined by [127]

$$P_{cr} \approx 16k \frac{A_{eff}}{g_s L_{eff}},$$ (49)

where k is a relative polarization factor (in the range of $1 \sim 2$) which equals 1, if the polarization of the pump and the Stokes wave is maintained along the fibre, and 2 if the polarization is completed scrambled. A_{eff} is the effective fiber area, g_s is the gain coefficient of the fibre and L_{eff} is the effective interaction length of the fiber defined by [128]

$$L_{eff} = \frac{1}{\alpha_p} \{1 - \exp(-\alpha_p L)\} , \qquad (50)$$

where α_p is the fibre attenuation for the pump frequency (dB/km). It can be seen that L_{eff} is near equal to the actual fibre length L, if $\alpha_p L \ll 1$ or α_p^{-1} if $\alpha_p L \gg 1$. The Raman gain coefficient g_s is dependent on the composition of the fibre core and can be varied significantly with the use of different dopants. It is worth noting that wavelength tunability by stimulated Raman scattering offers significant cost benefits and technical advantages over other tuneable laser systems based on parametric oscillators or frequency-mixing techniques. Furthermore, the technique has proved to be a stable and reliable near-infrared source.
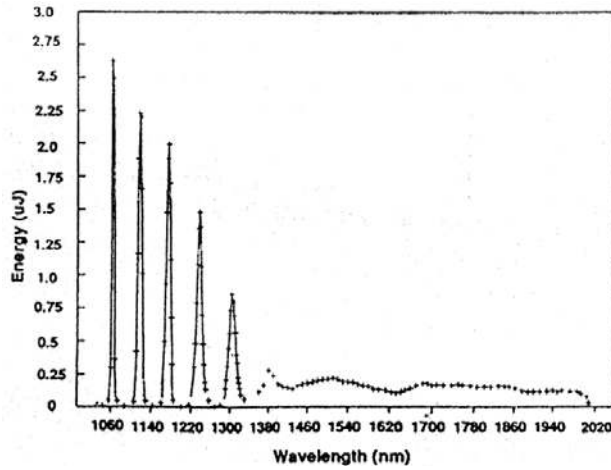
Fig. 30. Spectrum output from a silica fibre due to Raman scattering excited by a Nd:YAG laser [74].

MacKenzie [74] used a Q-switched Nd:YAG laser (Model SL50Q, Spectron Lasers) emitting at 1064 nm to pump a 1 km-long graded index multi-mode optical fibre (STC CA1618/392F) to produce tuneable near-infrared radiation. The pulsed duration of the pump was 180 ns, the pulse energy was about 3 mJ, and the pulse repetition rate was 200 Hz. The output spectrum of the fibre is shown in Fig. 30. The pulse duration varied between 190 ns and 600 ns, depending on wavelength. Wavelength selection was achieved with a scanning grating monochromator. The output energy was on the order of microjoule. This tuneable near-infrared optical source was used in the detection of PA glucose and oil in an aqueous system [74, 129].

The optical parametric oscillator is based on the non-linear optical process in which the energy of a pump photon is divided between two generated photons, called the signal and idler, such that the total energy and photon momentum are conserved [130]. Crystals such as beta barium borate (BBO) are often used as non-linear media. The pump requirements for BBO are met typically by a XeCl excimer or a Nd:YAG laser. Such a

system provides a tuning range extending from the near ultraviolet to beyond 3 μm in the near infrared. The output pulse energies are several tens of millijoules across the tuning range. The linewidth of the radiation is usually ~10 nm.

MacKenzie and Ashton [131] used a tuneable laser system (MOPO-710 Spectro-Physics), pumped by the third harmonic of a Nd:YAG laser at an output wavelength from 400 nm to 2300 nm, to study glucose in a solution with other blood analytes, such as sodium chloride, cholesterol, and bovine serum albumin (BSA). Shen [132] applied a similar laser system and the time-resolved PA technique to measure the optical absorption coefficient of a glucose solution. Köstli [133] used an OPO system, pumped by a Q-switched Nd:YAG laser emitting at the foundational wavelength of 1064 nm, with a tuneable wavelength range from 1500 ~ 3500 nm, to study soft tissues using PA infrared spectroscopy. Hodgson [134] applied a XeCl excimer pumped OPO for PA measurement of oil concentration in water. He found that there was considerable noise associated with the discharge spike produced by the operation of the excimer pump. This noise interfered with the PA signal, making quantitative analysis difficult.

Ti^{3+} sapphire laser is based on an electronically vibrational transition between the Ti^{3+} energy levels. Ti^{3+} ions are impurities formed within a sapphire crystal. The system has a broad laser transition linewidth, resulting in a wide tuning range. The Ti^{3+} sapphire laser can be operated in CW or pulsed mode, with an emission range from 660 nm to 1180 nm. It can output 100 mJ in a 10 ns pulse and produce an extremely short (20 fs) pulse. The Ti^{3+} sapphire laser has been used in high-resolution PA spectroscopy to investigate the vibration-rotation structure of C-H and C-C bonds in acetylene [135].

Several diode lasers radiating at different wavelengths may be combined into one instrument to provide a degree of wavelength tunability. In practice, the output wavelength of these diode lasers can be tuned by changing the temperature or using an adjustable external cavity. They offer an inherent advantage for portable devices.

Fiber lasers constitute another interesting form of tuneable near-infrared laser. They comprise an optical fibre doped typically with a rare earth element such as erbium or neodymium and may be pumped by a variety of sources. The tuning range of these lasers is usually in tens of nanometers. However, according to the literature, there are no PA applications as yet, probably due to the low energy output of fibre lasers.

7.3 Acoustic detectors

Several different types of acoustic detectors are available for PA detection. They include microphones, piezoelectric transducers, capacitance transducers, fibre-optic sensors, non-contact optical detectors, and so on [87]. The choice of detector for a particular application is mainly based on factors such as detection style, sensitivity, response time, bandwidth, impedance matching, noise, size and ruggedness. In the PA study of condensed matter, the most common detectors are the piezoelectric transducer and the non-contact optical detector. The former has a good acoustic impedance match while the latter can requires no contact with the object of study or form all optical device.

7.3.1 Piezoelectric detection

The piezoelectric effect is based on an electric charge produced on the surface of a material when deformed by pressure. This effect was first observed in natural crystals and is caused by a certain type of asymmetry in the crystal's structure. Any pressure change will distort the crystal, leading to a redistribution of charged elements in the lattice. The net result of this redistribution shows on the surfaces of the crystal. The voltage response of a thin piezoelectric element to a normal incidence plane pressure wave increases linearly as a function of the element's thickness, and is also proportional to its piezoelectric constants. However, if the thickness of the element exceeds the acoustic wavelength, a further increase in thickness does not result in a proportional increase in output voltage. If the acoustic waves are not planar in shape, the cross-sectional area of the element becomes an important consideration, since the pressure exerted may not be uniform over its entire area. The rise time of a piezoelectric element is equal to the ratio of the element's thickness and the acoustic velocity in the element.

Table 11. Properties of commonly used piezoelectric materials.

	LiNbO$_3$ (z-cut)	PZT-5A	PVDF
Piezoelectric constant			
d$_{33}$ (10^{-12} C/N)	6	374	-39 ~ -44
g$_{33}$ (Vm/N)	0.023	0.025	- 0.32
Mechanical Q factor	100	75	5 ~ 10
Density (g/cm^3)	4.64	7.7	1.78
Sound velocity (m/s)	7316	4500	2260
Acoustic impedance (10^6 kg/(m^{2}s))	33	35	4
Work temperature ($^\circ$C)	< 1100	< 300	< 60
Advantages	wideband, rugged	high sensitivity, inexpensive	wideband, inexpensive
Disadvantages	expensive	narrowband, ringing	non-rugged

In the reception of PA waves, commonly used piezoelectric materials include single crystals (quartz, lithium niobate), polycrystalline ceramics (lead zirconate titanate, Brium titanate, lead metaniobate) and polymer materials (PVDF, Teflon and Mylar). The most important properties and parameters of lithium niobate (LiNbO$_3$), lead zirconate titanate (PZT-5A) and PVDF are listed in Table 11.

a) Ceramic transducer

Piezoelectric ceramics are hard, dense and can be manufactured in almost any given shape or size. Their physical, chemical and piezoelectric characteristics can be tailored to specific applications. They are chemically inert and immune to moisture and other atmospheric conditions. Their mechanical and electrical axes are set during "poling", and

can be precisely oriented in relation to the shape of the ceramic. The geometry and composition of the ceramic element determines its resonant frequencies. If the frequencies of the acoustic waves received match the resonant frequencies of the piezoelectric element, the element will produce a maximum electrical signal.

The simplest and most common shape of ceramic element is a disk. It is characterized by two vibration modes: one in the thickness direction and another in the radial direction. In liquid or soft tissue detection, the acoustic wave is longitudinal, so only vibrations in the thickness mode are considered. The thickness of the disk element should be selected properly, such that the resonance frequency is identical to the frequency of the received signal, to ensure the efficient production of electrical signals. The disk transducer can efficiently receive signals produced by a point-like or a plane acoustic source. However, when the task in hand requires the reception of cylindrical acoustic waves, a piezoelectric ceramic tube is more efficient. The tube has also two main vibration modes: the thickness and the radial mode [136]. The sample under study fills the tube and a laser beam passes through the centre axis of the tube, producing a cylindrical acoustic source in it. When the beam diameter is sufficiently small, the detected vibration of the electrical signals is dominated by resonance in the thickness mode, otherwise, by resonance in the radial mode will prevail. All the emitted PA signals are received in an equi-phase condition at the entire cylindrical surface of the tube, resulting in maximal detection sensitivity [125]. However, it is very difficult to apply a tube-shaped detector to *in vivo* tissue measurements. In this application, a disk-shaped detector should replace it.
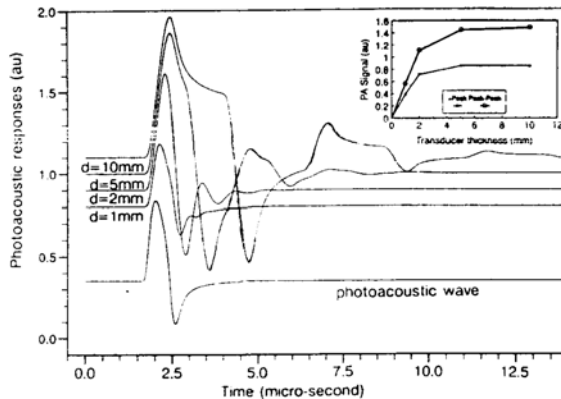
Fig. 31 Simulated PA responses from four piezoelectric detectors with different thickness [125].

The sensitivity of the piezoelectric ceramic transducer is high; a typical value is 30 μV/Pa for a disk-shaped PZT-5A transducer with a diameter and a thickness of 4 mm [88]. With increasing disk thickness, the PA response becomes gradually saturated, as illustrated by the simulation results in Fig. 31. Furthermore, the frequency response curve of the transducer is not flat and must be calibrated at the PA frequencies used. The acoustic impedance of a ceramic transducer is somewhat higher than that of soft tissues,

35×10^6 kg/(m^{2}s) in the PZT-5A and 1.5×10^6 kg/(m^{2}s) in water or a soft tissue. Even through the acoustic impedance mismatch causes a part of the incident acoustic energy to be reflected or scattered, the ceramic transducer offers a higher acoustic response than a polymer transducer or a microphone. Hence, if high detection sensitivity is the prime requirement, as it must be in the determination of glucose or other analytes, a ceramic transducer is usually chosen.

b) Polymer transducer

The PA response of a ceramic transducer is often dominated by the transducer's own frequency characteristics, which usually differ from those obtained with frequency spectroscopy. Hence, the shape of the electrical response produced by a ceramic transducer is not identical to the PA waveform. This is a drawback for applications that require a faithful reproduction of the PA waveform. By contrast, a polymer film transducer is capable of satisfying this requirement, due to its wideband characteristics and flat sensitivity–frequency curve, which is very useful in time-resolved PA detection and medical imaging. Moreover, as polymers are flexible and thin up to a few micrometers, the receiving surface of the transducer can be shaped at will.

The most common type of polymer used in transducers is a PVDF thin film. The transducer could be a fast rise-time (~ 5 ns) and a wide bandwidth (> 100 MHz). Tam has used a PVDF transducer successfully to receive 10 ns acoustic pulses [118]. The acoustic impedance of PVDF is about 4.1×10^6 kg/m^{2}s, closely matching that of soft tissues and water (1.5×10^6 kg/m^{2}s). The mechanical Q factor of PVDF is low enough to prevent ringing at the relevant frequencies. Although film thickness is a significant consideration, the film diameter is also important in time-resolved measurements. In reality, the active part of a piezoelectric film integrates the pressure experienced over its entire active area to produce a voltage output. To assure a broad angular response and to preclude diffraction effects from frequency filtering of the transducer's response, the diameter of the active area of a PVDF film is ideally restricted to a quarter of the wavelength at the highest frequency of interest. In medical applications, where many frequency components are typically below 3 MHz, the diameter of the film tends to be 200 ~ 400 μm. If the active diameter is larger than that, the alignment of the transducer relative to the acoustic wave under measurement is of critical importance. In addition, there is a trade-off between the size of the active area and measurement sensitivity.

c) Lithium niobate transducer

Although the polymer film transducer can be used in wideband measurements, its robustness and long-term stability leave a lot to be desired, making accurate absolute calibration difficult. A lithium niobate transducer can circumvent these deficiencies, since lithium niobate is a single-crystal piezoelectric material with is characteristically very hard and has a high Curie temperature. Moreover, it can easily be cut thinner than 20 mm, producing a resonance frequency in excess of one hundred MHz. Moreover, the longitudinal velocity of an acoustic wave in a z-cut lithium niobate crystal is high (7316 m/s), enabling a fast response and a wide bandwidth.

Sigrist [83] was the first to use a lithium niobate transducer to study high-frequency PA waves produced in a liquid. The transducer's sensitivity was of the order of 1 μV/Pa and it had a response time of 4 ~ 11 ns. The thickness of the crystal was 30 ~ 80 nm and the size is 2 mm × 2 mm. Oraevsky and Jacques [106] used a lithium niobate transducer in tissue optical parameter measurements *in vivo* and in medical diagnostics (PA

tomography). Owing to its high sensitivity and wide bandwidth, the lithium niobate transducer is suitable for PA imaging based on time-resolved stress detection. A few commercial products designed for medical applications (LaserSonix Technologies) exist, offering a sensitivity of a couple of 0.1 µV/Pa and an ultrasonic response frequency range of up to 300 Mhz. This means that the temporal resolution offered by the transducer is about 3 ns, corresponding to a 5 µm longitudinal resolution in tissue imaging.

7.3.2 Optical detection

A good systematic description of optical detection of ultrasound is provided by Monchalin [137], who classified relevant techniques into interferometric and non-interferometric techniques. Although he focused on the detection of ultrasonic waves in opaque solids, the fundamental principles of at least some of the techniques are also applicable to ultrasonic detection in liquids and tissues. References to ultrasonic detection in transparent solids and liquids by optical methods can also be found in references [138, 139].

The optical detection of ultrasonic waves offers some advantages over piezoelectric detection. First, it allows remote, wireless and non-contact monitoring. Second, it maintains its operational capability in magneto-electrically noisy and hazardous environments due to its full optical devices. Third, it can be positioned in places where even an opaque piezoelectric transducer may either obstruct or be affected by an irradiating light beam. Fourth, it is not difficult to assemble imaging arrays with sufficiently small element sizes and interelement spacings, while still retaining adequate detection sensitivity. On the other hand, by contrast with piezoelectric transducers, optical detectors tend to be less sensitive and require more complicated methods to rebuild the PA waveform.

a) Probe-beam deflection methods

When a light beam travels through a medium whose refractive index varies as a function of density or temperature drift, the light beam will be deflected from its incident direction. In addition, it has been established that an acoustic wave produces a density shift along its propagation path in a medium, causing a relative change in the medium's refractive index. Based on these two principles, a technique called probe beam deflection or beam lensing has been developed for the detection of PA signals [118, 140]. In accordance with the necessary geometric arrangements, this technique can be classified into two styles, transmitted probe-beam deflection and reflected probe-beam deflection.

The transmitted probe-beam deflection technique is based on the deflection of a probe light beam as it traverses a region of refractive-index change associated with a PA pulse in a medium, as shown in Fig. 32. A photodiode with a reception area much smaller than the cross-sectional area of the probe beam is used to receive the optical signals created by the deflection beam. Sullivan and Tam [118] used a probe optical beam parallel to the excitation beam and obtained a good redisplay of the PA waveform with 10 ns duration in methanol. They deduced that the transient angular deflection of the probe and the detection sensitivity were proportional to the time derivative of the acoustic pressure at the probe beam position in the medium, which was demonstrated by the output voltage amplitude of the photodiode in their experiment. Similar to piezoelectric detection,

integrating the voltage signal from the photodiode permits us to rebuild the PA waveform [82] and the absorbed optical distribution. In contrast with piezoelectric detection, however, the detection sensitivity of the probe-beam method depends on the parameters of the propagation medium, which, in turn, are influenced by temperature. This makes it difficult to compare different media in absolute terms. Moreover, this method cannot be used in opaque or light-scattering media.
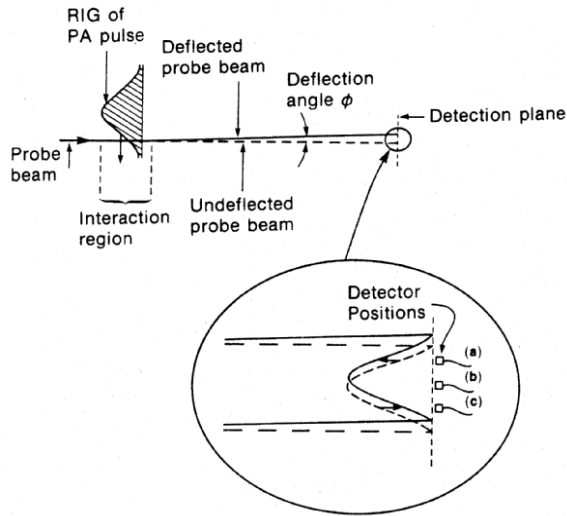

Fig. 32. Transmitted probe-beam deflection technique for PA detection due to the transient deflection of a narrow collimated probe beam by a refractive-index gradient [87].

The reflected probe-beam detection method was put forward by Paltauf et al. [140,141] for measuring the light distribution in scattering media (such as bio-tissues), as shown in Fig. 33. A glass prism, coupled with water, is mounted on the surface of a sample. An excitation beam illuminates the sample vertically, and a probe beam is tilted at an angle producing total internal reflection. The probe beam is focused on the prism-water interface. Having been reflected by the interface, the probe beam is directed onto a photodiode. The output voltage and the detection sensitivity of the photodiode are proportional to the pressure derivative of the reflectance at the measuring spot located on the glass-water surface. There are two operation modes for the excitation beam: the transmission mode used when the excitation and the probe beam are on the same side of the sample, and the reflection mode used when they are on different sides. Of these, the reflection mode is more relevant here, because it can be applied to the detection of the tissue optical attenuation coefficient *in vivo*, the layered structures of tissues and the distribution of pigments or blood vessels below skin surfaces. The reflected probe-beam method lends itself to the study of opaque or light-scattering media, better than the transmitted probe-beam detection method.
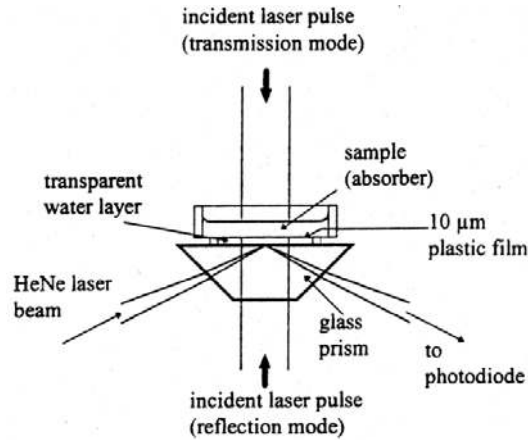
Fig. 33. Reflected probe-beam deflection methods [141].

b) Interferometry

An optical interferometer can detect distortions caused by physical parameters (such as pressure, temperature and so on) on the surface of an object. In this method, a probe beam is split into two parts; the first one is then reflected from the sample surface and the other from a reference surface. The two reflected beams are recombined, and the resultant interference intensity is monitored. In interferometric PA measurements, a beam whose optical path length is affected by PA pressure is compared to an unperturbed reference beam. The effects of pressure changes can then be observed in the interference pattern.

So far, such interferometric measurements have been used in the non-contact detection of PA pulse shapes in metal plates [142, 143] and in the non-destructive testing (NDT) of solids [144, 145]. The detection of acoustic waves in a liquid is based on the same principles, but the low optical reflection coefficient at the air/water interface decreases the sensitivity of this technique. Hodgson [134] used a Michelson-based optical fibre interferometer to investigate acoustic displacements on the surface of a liquid. These displacements were generated by the PA process within liquid. He constructed a pre-prototype instrument based on this principle for measuring the presence of oil in a water pipeline.

Jacques and Andersen [146] built a dual-beam common-path interferometer to study laser-induced PA waves from buried absorbing objects. This study simulated the detection of subcutaneous optically absorbing objects in the human skin, such as haemorrhages or vascularized tumours, which generate PA waves when slightly heated by a Q-switched laser pulse. When two beams are reflected onto a surface, pressure waves arriving at the surface reach one beam site before arriving at the second one. This produces a differential surface movement and a difference in the pathlength of the beams, which can be detected by an interferometer. The detectable surface movement was in the range of 0.1 ~ 63 nm with good linearity, and dynamic range of the linear measurement was 20 mbar ~ 200 bar at 20 mV/bar. They achieved sub-mm resolution in imaging an absorbing object at the depth of 11 mm within an aqueous phantom medium. They concluded that the sensitivity and noise level of the interferometer equalled or even

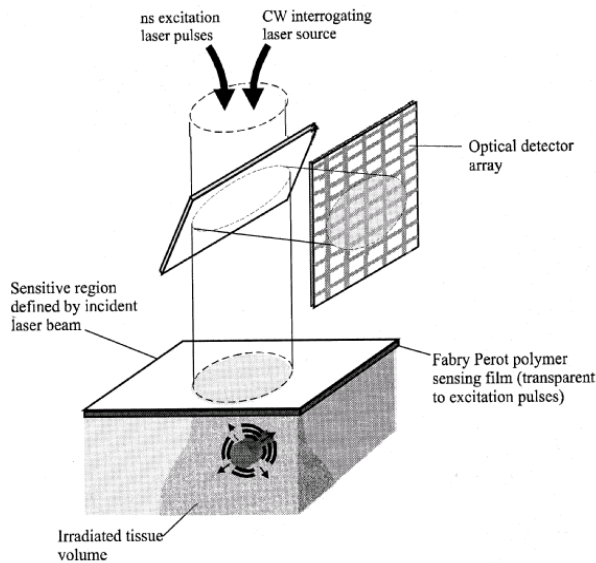exceeded those of lithium-niobate piezoelectric transducers.

Fig. 34. Schematic of a FPI photoacoustic imaging system [147].

A polymer film Fabry Perot sensing interferometer, developed by Beard and Mills [148,149], has also been used as an ultrasonic sensor. It provides a viable alternative to the piezoelectric detection method in applications involving PA imaging, because there are substantial difficulties involved in fabricating high-density 2D piezoelectric arrays with sufficiently small element sizes and inter-element spacing while retaining adequate detection sensitivity. The sensing mechanism of an FPI is based on the detection of acoustically-induced variations in the optical thickness of a Fabry Perot polymer film, presented in Fig. 34 for backward-mode PA imaging [147]. Nanosecond excitation laser pulses are transmitted through the sensing film into the target, generating PA contributions from each point in the diffusely irradiated volume. When illuminated by a CW interrogating laser source (aligned coaxially with the pulsed excitation beam), the film acts as a F-P interferometer, whose mirrors are formed by the deposition of wavelength-selective dielectric coatings on both surfaces of the polymer sensing film. They are designed to be reflective at the wavelength of the CW interrogating laser, but transparent at the wavelength of the excitation laser pulse. The PA signal modulates the optical thickness of the polymer film, thereby affecting the reflected light. A representation of the incident acoustic field across the sensing film can be obtained by leading the reflected light beams onto an optical detector array such as a CCD or a photodiode array. The achieved work has shown that the achieved detection sensitivity (< 10 kPa, without signal averaging) and bandwidth (30 MHz) are comparable to wideband piezoelectric PVDF ultrasonic transducers with the prospect of achieving substantially smaller element sizes (< 35 μm).

7.4 Pulsed PA apparatus based on a laser diode — PZT transducer

A schematic of the experimental apparatus is shown in Fig. 35. In this set-up, a laser, driven by a laser-driving circuit, outputs light pulses that are projected onto a sample. The acoustic wave produced in the sample is received by an acoustic transducer, which transforms it into an electrical signal. An amplifier enhances the output of the transducer, and the final electrical signal is input to a digital oscilloscope for analysis and storage. In the experiments described in this thesis, the exciting source is a laser diode, because it has a stable optical pulse, which makes energy monitoring and the normalization of the acoustic signal to pulse energy unnecessary.
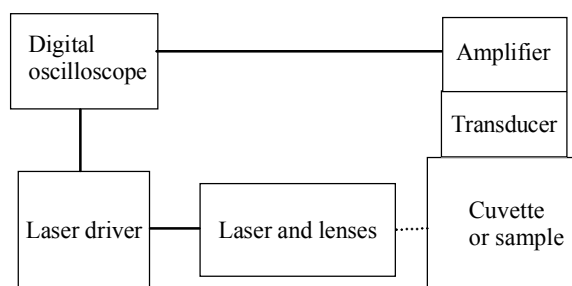
Fig. 35. Schematic of the PA apparatus used in the experiments.

To enable non-invasive determination of glucose in the human blood, the wavelength range of the laser was in the "human tissue window", i.e. in the near-infrared region. In this range, a laser beam is capable of penetrating into tissue and interacting with the glucose therein. In view of developing a portable glucose sensor, a pulsed laser diode was chosen as the exciting source due to such properties as light weight, small volume and low cost. The final choice fell on two commercially available diode lasers listed in Table 10, the PGAF5S16 and the C86091E. At 905 nm, the emission wavelength of the PGAF5S16 coincides well with the small background absorption feature present in both tissues and aqueous solutions. In addition, its pulsed energy is the highest of all commercial diode lasers. The emission wavelength of the C86091E (1550 nm), on the other hand, is at the wing of the strong water absorption feature centred at 1445 nm, which helps to decrease the background absorption of tissues. Both laser diodes were driven by homemade laser drivers [150] capable of supplying 40 A and 20 A peak currents in pulses with a typical duration of 200 ns and 160 ns, respectively. The pulse duration and repetition rate of the laser drivers were adjustable in the range of 50 ns to 1000 ns and 100 Hz to 1000 Hz, respectively.

A lens system (C110MP-B, THORLABS Inc.) consisting of a fibre-to-fibre matched pair was used to focus and project the output of the laser diode onto the sample. Its number aperture was 0.4 and focus length 6.2 mm. An optical fibre delivery system was designed to deliver excitation energy to the human body conveniently. The system was consisted of a 1-m long optical fibre and two fibre coupling lens pairs (C230220P-B,
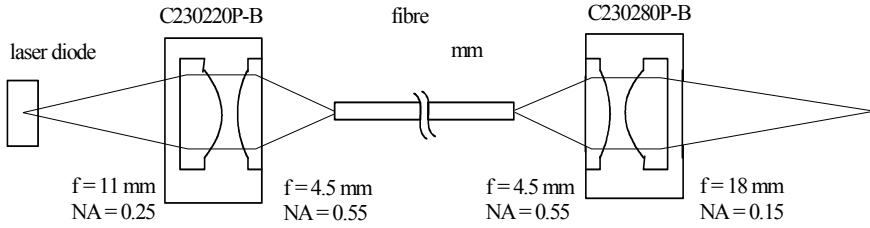
C230380P-B, THORLABS Inc.), shown in Fig. 36.

Fig. 36. Fibre delivery system of the PA apparatus.

A few cuvettes and holders were made for holding various samples and the piezoelectric transducer in the measurements. An ideal holder should not affect PA generation and reception, contaminate the sample or produce additional acoustic noise by absorption through its window and walls. Hence, the material and size of the cuvette should be selected carefully, especially when studying samples with low absorption and high scattering characteristics. Nevertheless, some stray light may still be absorbed by the cuvette wall, causing spurious signals produced by a temperature rise in the wall [87], i.e.

$$\Delta T = const /(\lambda_{dif} \rho \ C_P), \tag{51}$$

where λ_{dif} is the heat diffusion length of the wall, while ρ and C_P are the density and specific heat of the wall material, respectively. The "const" in the equation above contains the surface optical absorption factor. Thus, it is evident that the desired material properties of the cuvette should include small optical absorption at the surface, large thermal diffusion, high density and high specific heat. In these respects, silver or aluminium is a better choice than stainless steel. However, their high degree of chemical reactivity makes the choice of stainless steel a reasonable compromise. In actuality, we selected low absorption glass or quartz, both of which eliminate multi-reflection or scattering of stray light in the cuvette.

In our experiments, the duration of the excitation pulse was of the sub-microsecond order and the size of the cuvette was on the centimetre scale, making the geometry of the cuvette unimportant. However, the thickness of the cuvette should be considered carefully, because optical pathlength is related to the signal-to-noise ratio and contrast of the PA signal [74].

The selection of acoustic detector was influenced by two main considerations. Glucose solutions and tissues are weakly absorbing media and the excitation energy of a laser diode is low. As a result, a piezoelectric ceramic transducer was chosen owing to its high sensitivity. To achieve maximal detection sensitivity of PA waves generated in a weakly absorbing medium, the geometry of the transducer should resemble a hollow cylinder. However, as such cylindrical transducers are apparently not suitable for non-invasive measurements in the future, a few disc-shaped PZT transducers were made during the experimental part of this thesis. A schematic of these transducers is shown in Fig. 37.
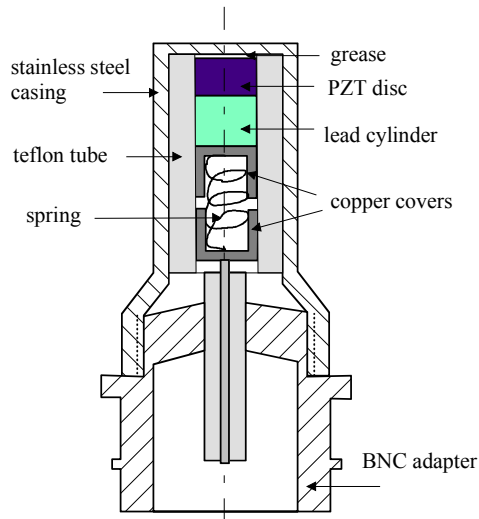
Fig. 37. Schematic of the piezoelectric PZT transducer.

To ensure the effective reception of acoustic waves, the two surfaces of the bottom plate of the stainless steel casing were polished, and the PZT disc was contacted with the internal surface by a layer of grease. In order to prevent excessive acoustic reflection at the rear face of the PZT disc, a backing material made of lead was coupled to the PZT disc. Because lead offers a high acoustic attenuation and its acoustic impedance is similar to that of PZT, the arrangement greatly decreased the ringing effect produced by acoustic multi-reflections in the PZT disc.

In this thesis, all measurements were carried out in weakly absorbing media excited by a laser diode. As the electrical signal produced by the PA pressure on the PZT transducer is very weak (on the order of microvolts), a low-noise preamplifier was needed to amplify the transducer's output for further analysis. A weak signal is easily interfered with by an environmental electromagnetic field, so the preamplifier was not connected to the transducer with a cable, but assembled together with it, to avoid electromagnetic pickup originating from the cable. Moreover, with a view to reducing noise pickup, a battery was deemed better than an alternating source as the power source of the preamplifier. The first stage of the preamplifier plays a significant role in meeting the low-noise requirement. The practical design used a low-noise junction field-effect transistor (U310) to pick up the output of the transducer, followed by an operational amplifier to amplify the signal. The circuit of the preamplifier is drawn in Fig. 38, with a gain of 40 dB.
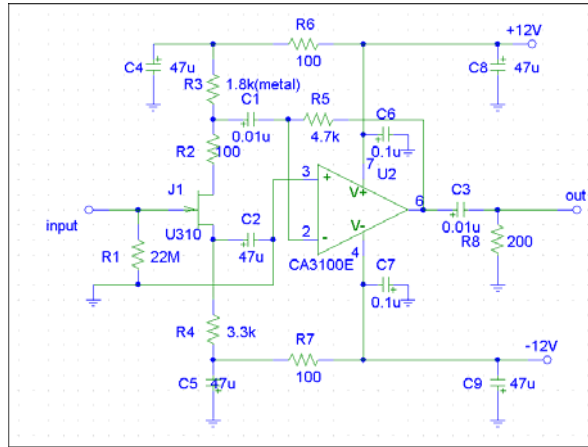
Fig. 38. The electrical circuit of preamplifier in the detectors.

PZT discs with different sizes of φ 1.5 mm × 1.5 mm, φ 4mm × 3 mm, and φ 5mm × 0.5 mm made a few piezoelectric transducers. Assembled directly with the preamplifier, the transducer consisting of a φ 4 mm × 3 mm PZT disc offers a larger PA signal (a few millivolts of electrical output produced in pure water). The frequency response of the detector is shown in Fig. 39, while its resonance frequency is approximately 420 kHz. The signal-to-noise ratio of the PA apparatus exceeds 200 when the signal is averaged 1024 times.
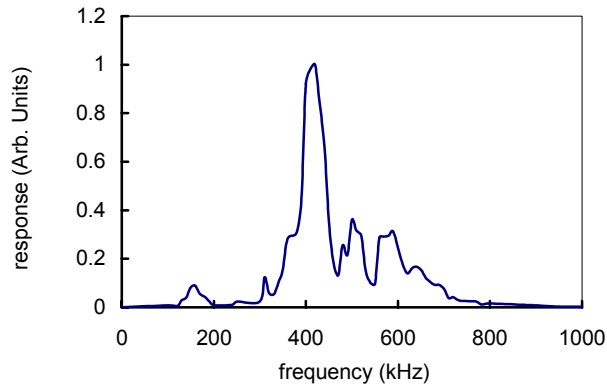
Fig. 39. Frequency response of the PZT detector.

7.5 PA experiments and results

7.5.1 Water solution

Anhydrous D-glucose is a white powder with excellent hydrophilic properties. When dissolved in distilled water, it releases micro-air bubbles forming the glucose solution colourless and transparent. Reference [121] studied the near-infrared absorption spectroscopy of glucose and established that the absorption coefficient of glucose differs approximately ±20% from that of water at 905 nm and 1550 nm (0.007 mm^{-1} and 0.98 mm^{-1}, respectively). If a laser beam with a wavelength of 905 nm illuminates a glucose solution, a cylindrical PA source is produced in it because of low optical absorption.

In the schematic of experimental apparatus shown in Fig. 35, the transducer was vertically aligned to the direction of the laser beam for the reception of the maximal acoustic signal in the case of a cylindrical PA source. 25 ml glucose solutions with different concentrations were prepared and kept motionless for half an hour before each test. The cuvette, measuring 2.5 cm (width) $\times$ 2.5 cm (thickness) $\times$ 5.0 cm (height), had a small valve at the bottom through which the different solutions could be drained during the experiment. The transducer was in direct contact with the solution for improved acoustic pickup. The measurements started with the lower concentration solutions, and proceeded toward increasingly high concentrations. In experiments at wavelength of 1550 nm, the reception surface of the transducer was turned against the direction of the laser beam to allow effective reception of PA signals, because of high optical absorption at that wavelength.

Typical PA signals produced by water and the various glucose solutions were similar, except for their amplitudes. The relationship between glucose concentration and the relative change of the PA signal is depicted in Fig. 40. It can be seen that the PA amplitude increases by about 2% when the glucose concentration increases by 1% in the experimental range. This result is identical to that reported in Paper VI. The minimal glucose concentration detected by the apparatus was about 0.5%.
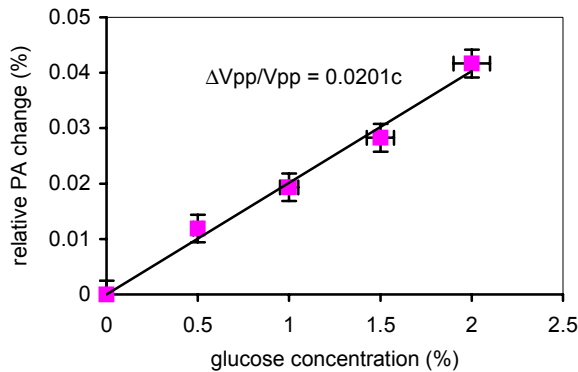

Fig. 40. Relative PA change of glucose solutions with different concentrations.

7.5.2 Milk solution

The composition of commercially available milk is listed in Table 12, which shows, among other things, that the proportion of dry ingredients is 12.9%. The diameters of fat globules are in the range of 0.1 μm to 10 μm, while the corresponding dimensions of casein micelles vary from 0.01 μm to 0.3 μm. Compared with the human skin [104], the percentage of every dry ingredient is low (apart from lactose, whose absorption resembles that of water at 905 nm), which means that the optical absorption of milk is lower than that of the skin at 905 nm. At this wavelength, the absorption coefficient of the skin (0.23 cm^{-1} [111]) is a little higher than the absorption coefficient of water (0.07 cm^{-1}). Hence, it can be deduced that the absorption coefficient of diluted milk is approximately equal to that of water at 905 nm. In the red and short near-infrared region (at least from 600 nm to 1100 nm), scattering particles with diameters larger than 50 nm scatter light in accordance with Mie scattering, which is relatively wavelength independent. Thus, it is reasonable to assume that scattering in milk is dominated by Mie theory. The scattering coefficient of milk, measured in Paper V, has been established at about 1.45 cm^{-1} for a 1% milk aqueous solution. These figures indicate that, as a substance, milk can be characterized as having low absorption and high scattering characteristics.

Table 12. Average compositions of commercial milk [151] and skin [104].

	Water (%)	Fat (%)	Protein (%)	Lactose (%)	Ash (%)
milk	87.1	3.94	3.27	4.93 %	0.76
skin	65.3	9.4	24.6		0.7

Papers V and VI describe PA experiments on milk solutions, whereas Paper VI studies changes in PA signals in a 3% milk solution with varying glucose concentrations. These experiment used the same apparatus and cuvette as the water experiments described in Section 7.5.1. An amount of glucose solution was dropped into a milk solution to change its glucose concentration. The results show that PA amplitude increases by about 5.4% when the glucose concentration in the sample increases by 1%.

7.5.3 Tissue sample

Paper VI describes glucose measurements in a tissue sample consisting of fresh lean pork. To facilitate alterations in the sample's glucose concentration, the sample was immersed in a glucose solution. This enabled the diffusion of glucose into the tissue. The size of the sample was carefully selected, because a large sample requires a long diffusion time, while a small one distorts the measurement such that changes in the PA signals are caused mainly by glucose in the liquid, not by glucose in the tissue. On the other hand, blood and interstitial fluid diffuse out of the tissue and into the glucose solution. Hence, the tissue should be drained of blood prior to the experiment, because blood has a great influence on the absorption property of the tissue. In this experiment, the sample was

immersed in a phosphate buffer solution and washed a few times in the course of two days, until it was clean of capillary blood and interstitial fluid. The sample was then soaked in the buffer solution to keep the hydration rate constant. In addition, it was always stored in a refrigerator at 4 °C before each PA measurement.

During the experiment, the tissue sample was immersed in the buffer solution to decrease the reflection of acoustic waves at the boundaries between the tissue and the transducer and glass of cuvette wall. A high concentration glucose solution was dropped into the buffer solution, and the subsequent diffusion of glucose molecules into the tissue sample was observed. The experiment showed that the diffusion of glucose gradually increased the PA amplitude of signal. The measured concentration sensitivity was about 2.5% when the glucose concentration increased by one percent. The water content of the soaked sample was approximately 75%, which was measured by drying the sample after the PA measurements.

7.5.4 Whole blood

A detailed description of the experimental procedure and the results of the study of glucose in whole human blood can be found in Paper IV. It should be emphasized that it is considerably more difficult to make PA glucose measurements in whole blood than in water or milk. Because blood is an active substance with ongoing biochemical and biophysical changes, the red blood cells are capable of changing their morphology, or forming sediment structures and aggregating, which may strongly affect the optical and acoustic properties of blood sample. Thus, PA signals produced in the blood sample are not characterized by a high degree of stability.

As shown in Section 4.2.3, the absorption coefficient, scattering coefficient and anisotropy factor of a blood sample are strongly affected by such parameters as haematocrit, flow velocity, osmolarity, oxygen saturation and haemolysis [109]. As a consequence, the condition of the blood sample has far-reaching effects on its optical parameters. The blood sample in this experiment was drawn from a vein and collected in evacuated tubes with an anti-clotting agent (EDTA). The experiment used only one blood sample to avoid variations caused by haematocrit. The sample was put into a cuvette which connected with a liquid circulating system. The circulation velocity of blood was carefully selected to avoid the sedimentation and haemolysis of red blood cells. The blood in cuvette was exposed to air and comprised a function that maintained the oxygen content of the sample in a saturated state during circulation. Moreover, the environmental temperature was also kept at a constant level during the experiment. Based on these processes, the PA signal gradually trended to stability after blood sample circulated about ten minutes.

A liquid dispenser dropped a high concentration glucose solution into sample. To maintain the osmolarity of the sample, the glucose solution was prepared by dissolving anhydrous glucose into a buffer solution, isotonically with human blood. When the glucose solution was added into the blood sample, the PA signal increased immediately. The results showed that the PA amplitude increased about 7% when the glucose concentration rose up to 500 mg/dl, corresponding to the upper level of the physiological glucose concentration. The minimum detectable concentration was about 100 mg/dl. The

experiment was performed within 2 hours after the sample was drawn from the vein.

7.5.5 Human body experiment

The measurement site is an important consideration in noninvasive blood glucose sensing. Burmeister and Arnold [32] have reported a study using near-infrared transmission spectroscopy, where they evaluated the cheek, lower lip, upper lip, nasal septum, tongue and webbing tissue between the thumb and the forefinger as measurement sites. Their results show that the tongue is the best site, because it has the lowest fat content. However, the conditions are different in near-infrared PA spectroscopy, where important concerns include preventing light from directly irradiating the surface of the piezoelectric transducer and keeping a proper distance between the transducer and the PA source to decrease the effects of scattering photons on the transducer. Because soft tissues are weakly absorbing and the excitation source in our apparatus was a laser diode with low output power, a transducer with high piezoelectric effect (PZT) and large active area was used to receive the PA signals. The experiment demonstrated that the maximum PA signal could be produced and received at the fingertip, as shown in Fig. 41.
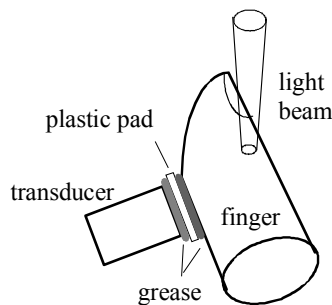
Fig. 41. Sketch of the PA experiment on a finger.

To illuminate the side of the index finger, a laser beam was guided by the fibre/lens system depicted in Fig. 36. The transducer was in contact with the finger pad through a thin plastic film, and high vacuum silicone grease was used to increase the acoustic coupling between them. The function of the plastic film was to impede scattering photons from impacting the receiving surface of the transducer and to decrease noise pickup from the finger. During the experiment, the test person was lying down to keep his body, arm, hand and finger naturally relaxed and as motionless as possible. The contact force between the transducer and the finger was fixed at an appropriate level.

The PA experiments were carried out on the right index finger of three healthy volunteers who had fasted overnight before the measurements, as described in Paper VII. The results showed that the stability of the PA signal at the finger was inferior to that in the *in vitro* measurements discussed above. If the contact force between the transducer

and the finger was too strong, it tended to produce a decrease in the PA signal over time. After the volunteer drank some water or a glucose solution, the PA amplitude increased to some degree. Unfortunately, the experimental results cannot make a distinction between drinking water and imbibing a glucose solution.

7.6 Discussion

As mentioned in Chapter 3, the shape of a PA source produced in a homogeneous medium can be described as being cylindrical, spherical or planar. Disregarding scattering effects, the PA amplitude resulting from thermal expansion can be united as

$$P = k_c \frac{E_a \beta v^u}{C_p r^i R^j} , \tag{52}$$

where R is a measure of the radius of the acoustic source, r the distance of detection, and k_c a proportional constant. The indexes of i and j are in the region of $0 \sim 1$ and $0 \sim 2$, respectively, and relate to the shape of the acoustic source, whereas u is in the region of $\frac{1}{2} \sim 2$, and relates to the duration of the exciting pulse. Although Eq. (52) is deduced from a non-scattering medium, it can be used to explain the scattering effect on PA amplitude in weakly absorbing media.

In the PA experiments described in the previous section, the laser duration was in the range of 160 ns $\sim$ 200 ns and the emitting area of the diode laser (PGAF5S16) was 400 μm $\times$ 430 μm. The acoustic velocity of aqueous solutions and tissues is about 1500 m/s. The calculation showed that $\tau_L < \tau_a$, which corresponds roughly to the case of short pulse excitation or stress confined condition. Hence, $u \approx 2$ and then Eq. (52) can be simplified for PA generation in a weakly absorbing medium

$$P \approx \frac{k_c E}{\sqrt{r}} \frac{\mu_a \Gamma}{R^{3/2}} , \tag{53}$$

where $\Gamma = \beta v^2 / C_p$. In the experiments above, the laser energy was maintained at a constant level and the apparatus was not moved. Hence, the relative change of PA signal produced by composition change can be expressed by

$$\frac{\delta P}{P} \approx \frac{\delta \mu_a}{\mu_a} + \frac{\delta \Gamma}{\Gamma} - 1.5 \times \frac{\delta R}{R} . \tag{54}$$

Eq. (54) provides an exact description only for a case where a change in the composition of the sample does not greatly affect its relative parameters. This condition is satisfied in the glucose experiments above. Therefore, it may be concluded that a change in PA amplitude is the sum of changes in μ_a, Γ and R, where the change in Γ can be calculated from

$$\frac{\delta \Gamma}{\Gamma} = \frac{\delta \beta}{\beta} + 2 \cdot \frac{\delta v}{v} - \frac{\delta C_P}{C_P} . \tag{55}$$

In the glucose-water solution experiment, a 1% concentration change caused $\delta\alpha/\alpha = -0.16$ % and $\delta\Gamma/\Gamma = 2.33$ %, on the basis of referring Fig. 25 and the results in Section 7.1.3, respectively. Because a glucose solution is transparent, the concentration change does not affect the cylindrical radius of the PA source, so $\delta R/R = 0$. Hence, $\delta P/P = 2.17\%$ as calculated by Eq. (54). This agrees well with the experimental results in Section 7.5.1 ($\delta P/P = 2\%$).

In 3% milk, the scattering coefficient (≈ 4.5 cm^{-1} in Paper V) is much larger than the absorption coefficient, and the concentrations of fat, protein and lactose are about 0.12%, 0.1% and 0.15%, respectively. At 905 nm, the absorption coefficients of fat, protein and lactose are of the same order as the absorption coefficient of water. Therefore, it is reasonable to assume that the absorption coefficient μ_a and Γ of 3% milk are similar to those of water, considering the low composition concentrations. Thus, when the glucose concentration changed by 1%, $\delta\mu_a/\mu_a \approx -0.16\%$ and $\delta\Gamma/\Gamma \approx 2.33\%$. On the basis of Eq. (54) and the results obtained in Section 7.5.2 ($\delta P/P = 5.4$ %), it may be calculated that $\delta R/R \approx -2.15\%$. This means that the addition of glucose into a milk solution decreases the radius of the PA source. This decrease is produced by a reduction in the scattering coefficient of the sample.

For a bloodless tissue, μ_a equals 0.025 mm^{-1} [111] at 905 nm and Γ is 0.15 [105]. Bearing in mind the fact that the absorption coefficient of water is about 0.085 cm^{-1} and the Γ of 1% glucose solution is 2.33% larger than that of water (equal to 0.11 [106]). The result ($\delta P/P = 2.5\%$) described in Section 7.5.3 and equation (54) give $\delta R/R = -2.26\%$ for the diffusion of one percent glucose in a bloodless tissue. Hence, similar to a milk solution, glucose decreases the scattering coefficient of the tissue. It can be seen that the signal response resulting from changes in absorption (a decrease of 0.64%) and Γ (a decrease of 0.25%) is smaller than the change of term $-1.5\delta R/R$ (= 3.4%). This shows that the glucose detection sensitivity is mainly dependent on the scattering effect caused by glucose in tissue.

The glucose detection sensitivity of the apparatus is higher in milk and tissue than in distilled water, due to decreased scattering. This can be explained as follows. The refractive index of glucose (in a 40% solution) and water is 1.39 and 1.33, respectively [152], while the indices of fat, protein and cellular membranes vary between 1.35 ~ 1.46 [114,153]. As a consequence, the dissolution of glucose decreases the mismatch between the refractive indices in the scattering samples, causing a relative decrease in the scattering coefficient of milk and tissue. Furthermore, the glucose detection sensitivity is smaller in a tissue sample than in a milk solution. This is partly due to cancelling effects between the contributions of the terms $\delta\mu_a/\mu_a, \delta\Gamma/\Gamma$ and the scattering term $-1.5\delta R/R$ in the case of glucose in tissue. Another, perhaps more significant, reason may be that washing the tissue sample a few times effectively removed a multitude of small particles, thereby decreasing the contribution from $\delta R/R$.

Whole (oxygenated) blood is known to have an optical absorption coefficient of 0.7 mm^{-1} and a reduced scattering coefficient of 1.2 mm^{-1} at the wavelength of 905 nm. In addition, its Γ is about 0.18. Mathematical calculations indicate that a PA source in blood tends toward a spherical shape, when the radius of the exciting light beam is about 0.5 mm. In this case, the proportional index before $\delta R/R$ in Eq. (54) changes its value from 3/2 to 2. When one percent glucose is added into a whole blood sample, its $\delta\mu_a/\mu_a \approx -1\%$ and $\delta\Gamma/\Gamma \approx -0.4\%$. Hence, $\delta R/R \approx -7.7\%$. It is evident that the term $\delta R/R$ also dominates

the change of PA signal. Moreover, the value of $\delta R/R$ produced in whole blood is larger than the corresponding terms produced in the 3% milk solution or tissue sample. This maybe explained as follows. The refractive indices of plasma and erythrocytes are 1.33 and 1.4, respectively, and the volume ratio of plasma in whole blood is about 55%. When the glucose concentration in whole blood changes by one percent, the relative concentration of glucose in plasma is larger than one percent, because glucose is mainly dissolved in plasma. This produces a better match between the refractive indices of plasma and red blood cells. Hence, scattering decreases even further, and the size of the PA source decreases correspondingly.

In the initial experiment, a glucose powder was added into a few blood samples directly, as in Paper II. This introduced some disadvantages. First, an error in the haematocrit content of different blood samples may cause an error in the PA amplitude before the addition of glucose. Second, the glucose powder may change the shape of blood cells or cause them to break up, owing to its powder property and different osmolarity. Third, the glucose powder may be surrounded by blood cells such that it does not dissolve immediately and completely. Fourth, in measuring different samples, drifts in the oxygen saturation level and the cell's velocity may produce variations in the relevant optical parameters, affecting the PA amplitude. Hence, the results are equivocal. These points may also explain why the glucose concentration sensitivity reported in Paper II was somewhat lower than that described in Paper IV.

The skin experiments *in vivo* described in this thesis demonstrate that a correlation exists between PA changes and physiological changes. This is attested by the finding that the PA amplitude drift is about 5% ~ 10% (reported in Paper VII) before the volunteers drink water. This figure is far in excess of the drift values of 0.5% and 1%, measured in distilled water and whole blood, respectively. The variance reveals that physiological fluctuations like body temperature shift, body fluid or blood composition drift and moisture uptake-release in the skin may produce great fluctuations in PA signals. After the volunteers drank 300 ml of water, the PA amplitude started to increase. The reason is that drinking water will change the blood circulation and water content of the skin, causing a result of affecting the skin's composition, temperature and morphology, thereby altering its optical and thermal parameters. However, the skin experiments failed to show any correlation between PA change and changes in the physiological glucose level. The dominant reason is the signal produced by physiological glucose change is smaller than the sum produced by other physiological changes, as explained in below paragraph. The other reasons include motion artefacts, low signal level, environmental electromagnetic noises and temperature drift.

The experimental results explained in Sections 7.5.3 and 7.5.4 showed that a 500 mg/dl change in glucose concentration, i.e., the upper value of the physiological glucose level, produced a change of 1.2% in the PA signal in the tissue sample and a 7% change in the whole blood sample. In addition, the *in vivo* experiment in Section 7.5.5 indicated that other physiological fluctuations and changes are capable of causing a fluctuation of up to10% in the PA signal. This means that the PA signal generated by a physiological glucose change submerges into the noise produced by other physiological drifts. Eq. (54) and the analysis above suggest that changes in the PA signal are mainly caused by the term $\delta R/R$, i.e., that PA changes are chiefly produced by changes in scattering by glucose. It has been reported that, at different locations in the skin, the reduced scattering coefficient may vary from 3.3% [43] via 9.9% [44] to 20% [42], provided that the change

in the glucose concentration is at the maximum physiological level (33 mM). On the other hand, reference [154] reports that physiological shifts may produce a drift of up to 15% in the scattering coefficient of the epidermis in the course of 20 minutes. This analysis demonstrates again that a change in scattering generated by the physiological glucose level could be embedded in the change produced by other physiological fluctuations. Thus, we may conclude that although the near-infrared pulsed PA technique offers higher detection sensitivity than the optical absorption method, it faces the same problem as optical methods based on measuring the scattering coefficient when applied to non-invasive glucose determination in human skin.

8 Summary

In 1993, the research group led by MacKenzie in Heriot-Watt University first reported PA blood glucose measurement. Three years later, Optoelectronics and Measurement Techniques Laboratory in University of Oulu began to pursue this research direction. I joined the research project in September 1996, to work on the photoacoustic theory at first. In 1997, we started studying tissue optics, with a focus on the optical parameters of the human skin. This work included the construction of skin models, whose PA sources were simulated by the Monte Carlo method. Subsequent work involved using the thermodynamic method to measure the thermal expansion coefficient and specific of heat of glucose solutions. In 1998, I applied the PA experimental apparatus to demonstrate pulsed PA theory and solute measurements. And same time, I finished my licentiate thesis. Since 1999, I have concentrated on refining the experimental apparatus, particularly the piezoelectric transducers and the preamplifiers. A number of PZT and PVDF transducers were made and assembled together with homemade preamplifiers. The new detectors greatly increased the response of the PA signals and the signal-to-noise ratio of the apparatus. Just before the Millennium, I began to explore blood optics and make PA glucose measurements in whole human blood. Since then, my research work has centred on optical scattering and its effects on the PA measurement. In the second half of the year 2000, I conducted a set of experiments to study the scattering function of milk in water and glucose in whole blood. Because the time-resolved stress detection technique has great potential in non-invasive human glucose measurements, I investigated the technique and its application to medical diagnosis and imaging. In the first half of 2001, I employed the PA apparatus to study the scattering property of glucose in weakly absorbing media such as milk solutions and tissue samples. At the same time, I experimented with non-invasive PA measurements in the human skin and analyzed the results. The writing of this dissertation began in April of 2001.

The thesis work relates to photoacoustics, a cross subject of optics and acoustics and to tissue (including blood) optics, another interdisciplinary subject incorporating medicine and optics. The study of these two subjects is not limited to blood glucose measurements, other potential applications include tissue property measurements, tissue diagnosis and imaging, drug and cosmetic delivery, waste water processing, and trace determination in industries.

In this thesis, PA amplitudes were first deduced on the basis of the thermodynamic

principle, which correspond very well with results deduced from the wave equation of thermal generation. The PA amplitude and acoustic duration formulas reveal the mechanism of thermo-elastic acoustic generation. In some cases, the concept of time-resolved stress detection can also be applied to a cylindrical PA source.

The study of near-infrared tissue optics led to the development of a five-layer optical model of the skin. The Monte Carlo simulation demonstrated that the shape of the PA source depends not only on the distribution of optical parameter in the skin, but also on the radius of the exciting energy beam. The results showed that a sturdy laser beam produces a planar PA source and drives the source deeper into the skin, while a thin laser beam generates a PA source closer to the surface of the skin. In addition, a thin beam offers a higher transverse resolution for PA diagnosis and imaging.

The initial PA apparatus failed to detect any PA signals in pure water or in samples with a low absorption coefficient at 905 nm. However, the development of new PZT transducers and preamplifiers with a ten-fold increase in signal-to-noise ratio solved the problem.

The formula for PA amplitude implies that PA spectroscopy has inherently higher detection sensitivity than optical absorption spectroscopy, due to the effects of the thermal expansion coefficient, specific of heat and acoustic velocity. However, a separate measurement of these physical parameters showed that a 1% glucose solution increases the united physical parameter Γ (Grüneisen parameter) only by 2.3%, compared to pure water. Considering the fact that Γ is slightly larger in the skin than in water and that the physiological glucose concentration is close to 0.1%, we may conclude that the PA method offers no apparent advantage over the optical method in terms of detection sensitivity in non-invasive glucose measurements.

The scattering effect of glucose in a blood sample was studied by a picosecond pulsed laser and a streak camera. The given temporal dispersion curves of blood glucose samples demonstrated that glucose decreases the scattering coefficient of blood. This is also proven by PA blood glucose measurements. The blood sample measurements do away with physiological changes in *in vivo* measurements, which means the decrease in scattering is directly caused by a change in the refractive index.

The results of the PA measurements show that the detection sensitivities (for 1% glucose change) in water, 3% milk solution, tissue sample and whole human blood are about 2%, 5.4%, 2.5% and 14%, respectively, at 905 nm. With the exception of glucose in a water solution, the observed glucose detection sensitivity in other turbid samples was larger than the expected theoretical values, provided we only consider changes in absorption and the united physical parameter. This demonstrates that the scattering effect of glucose is significant for the detection sensitivity of the PA method, particularly in the case of whole human blood.

A glucose tolerance test has been reported that the reduced scattering coefficient decreases by 2.1% when blood glucose concentration on human body increases 3.6 mM. [42]. This result equally stated that the change ratio of reduced scattering coefficient is about 32% for 1% change of blood glucose concentration. It then follows that, in near-infrared blood glucose measurements, if the scattering change is mainly produced by a change of glucose concentration, the optically diffuse reflectance technique has a higher sensitivity than PA method.

In non-invasive skin experiments, the PA signal fluctuated by about 10%. This fluctuation was related to shifts in physiological drift, blood circulation and the skin's

water content. This value is close to or larger than the PA signal changes produced in tissue and whole blood samples by changes in the physiological glucose concentration. Moreover, drinking water apparently increases the PA signal, thereby effecting the non-invasive PA determination of blood glucose.

It is known that glucose scattering influences detection sensitivity in near-infrared wavelengths much more than its absorption or united thermal physical parameter. However, the change in the reduced scattering coefficient is smaller than 16% when blood glucose changes in the physiological concentration. On the other hand, it has been reported [154] that physiological shifts may produce a drift of up to 1 % in the scattering coefficient of the epidermis in just 20 minutes. This finding demonstrates that glucose detection based on measuring the scattering coefficient is not a viable option because of physiological fluctuation producing largely scattering change in skin.

It must be emphasized that the PA method is not a better choice for optical scattering measurements or non-invasive blood glucose determination based on optical scattering effects. This can be explained as follows. Rather than being directly related to the optical scattering coefficient, the PA mechanism depends more on the total effect of optical absorption and thermal expansion. Even the scattering measurement suffers from the problem that scattering changes tend to be the combined result of all skin, rather than being produced by a specific composition, for example by glucose. However, if a special layer in skin can be separately studied, such as to be processed by optical coherent tomography, it is conducive to decrease the interferences from other skin layers. This should be a direction of future work in non-invasive glucose measurement.

References

1. Amos AF, McCarty DJ & Zimmett P (1997) The rising global burden of diabetes and its complications: estimates and projections to the year 2010. Diabetic Medicine, Supplement 5: S1-S5.
2. Lahmann W, Ludewig HJ, & Welling H (1977) Opto-acoustic trace analysis in liquids with the frequency-modulated beam of an Argon ion laser. Analytical Chemistry 49: 549-551.
3. Oda S, Sawada T & Kamada H (1978) Determination of ultra trace Cadmium by laser-induced photoacoustic absorption spectroscopy. Analytical Chemistry 50: 865-867.
4. Oda S, Sawada T, Nomura M & Kamada H (1979) Simultaneous determination of mixtures in liquid by laser-induced photoacoustic spectroscopy. Analytical Chemistry 15: 686-690.
5. Oda S, Sawada T, Moriguchi T & Kamada H (1980) Analysis of turbid solutions by laser-induced photoacoustic spectroscopy,.Analytical Chemistry 52: 650-653.
6. Voigtman E, Jurgensen A & Winefordner JD (1981) Comparison of laser excited fluorescence and photoacoustic limits of detection for static and flow cells. Analytical Chemistry 53:1921-1923.
7. Voigtman E, Jurgensen A & Winefordner J (1981) Condensed phase photoacoustic spectroscopic detection of porphyrins and dyes. Analytical Chemistry 53: 1442-1446.
8. Collins PM (1987) Carbohydrates. Chapman and Hall, London.
9. Libnau FO (1994) Structure of water and anomeric components of glucose resolved by evolving latent projections of infrared spectroscopic profiles. Doctoral thesis, Department of Chemistry University of Bergen.
10. Marshall WJ (1989) Illustrated Texbook of Clinical Chemistry, Gower Medical, London.
11. Kunst A (1984) Methods of Enzymatic Analysis. In: Bergmeyer HU (ed), 3rd edition, 6: 178-185.
12. Auses JP, Cook SL & Maloy JT (1975) Chemiluminescent enzyme method for glucose. Analytical Chemistry 47: 244-249.
13. Eggins BR (1996) Biosensors: An introduction. John Wiley & Sons Ltd and BG Teubner.
14. Shults MC, Rhodes RK, Updike SJ, Gilligan BJ & Reining WN (1994) A telemetry instrumentation system for monitoring multiple subcutaneously implanted glucose sensors. IEEE Transactions on Biomedical Engineering 41: 937-942.
15. Fischer U, Rebrin T, Woedtke TV & Abel P (1994) Clinical usefulness of the glucose concentration in the subcutaneous tissue – properties and pitfalls of electrochemical biosensors. Hormones Metabolism Research 26: 515-522.
16. Sternberg F, Meyerhoff C, Mennel FJ, Bischof F & Pfeiffer EF (1995) Subcutaneous glucose concentration: its real estimation and continuous monitoring. Diabetes Care 18: 1266-1269.
17. Tamada JA, Bohannon NJV & Potts RO (1995) Measurement of blood glucose in diabetic subjects using non-invasive transdermal extraction. Nature Medicine 1: 1198-1201.
18. http://www.cygn.com/glucowatch.html.

19. Kimura J, Kuriyama T, Kikuchi M & Arai T (1992) non-invasive monitoring of glucose in blood. Chemical Sensor Technology 4: 241-251.
20. Kuriyama T (1994) A portable blood glucose monitoring system. Proceedings of Electro-chemical Society 9414: 10-16.
21. Kost J, Mitragotri S, Gabbay RA, Pishko M & Langer R (2000) Transdermal monitoring of glucose and other analytes using ultrasound. Nature Medicine 6(3): 347-350.
22. Mitragotri S, Coleman M, Kost J, & Langer R (2000) Transdermal extraction of analytes using low –frequency ultrasound. Pharmaceutical Research 17(4): 466-470.
23. Heise HM (1996) non-invasive monitoring of metabolites using near infrared spectroscopy: state of the art. Hormones Metabolism Research 28: 527-534.
24. Coté GL (1997) Noninvasive optical glucose sensing – An overview. Journal of Clinical Engineering 22(4): 253-259.
25. Waynant RW & Chenault VM (1998) Overview of non-invasive fluid glucose measurement using optical techniques to maintain glucose control in diabetes mellitus. LEOS Newsletter 4: 3-6.
26. Khalil OS (1999) Spectroscopic and clinical aspects of non-invasive glucose measurements. Clinical Chemistry 45(2): 165-177.
27. McNichols RJ & Coté GL (2000) Optical glucose sensing in biological fluid: an overview. Journal of Biomedical Optics 5(1): 5-16.
28. Haaland DM & Thomas EV (1988) Partial least-squares methods for spectral analyses 1: relation to other quantitative calibration methods and the extraction of qualitative information. Analysis Chemistry 60: 1193-1202.
29. Heise HM, Marbach R, Janatsch G & Krüse-Jarres JD (1989) Mulitivariate determination of glucose in whole blood by attenuated total reflection infrared spectroscopy. Analysis Chemistry 61: 2009-2015.
30. Martens H & Naes T (1991) Multivariate Calibration. Wiley, Chichester.
31. Robinson MR, Eaton RP, Haaland DM, Koepp GW, Thomas EV, Stallard BR & Robinson PL (1992) Noninvasive glucose monitoring in diabetic patients: a preliminary evaluation. Clinical Chemistry 38(9): 1618-22.
32. Burmeister J & Arnold MA (1999) Evaluation of measurement site for non-invasive blood glucose sensing with near-infrared transmission spectroscopy. Clinical Chemistry 45(9): 1621-1627.
33. Blank TB, Ruchti TL, Malin SF & Monfre SL (1999) The use of near-infrared diffuse reflec-tance for the non-invasive prediction of blood glucose levels. IEEE Laser Electro-Optics Society Newsletter 13(5): 9-12.
34. Heise HM, Marbach R, Koschinsky TH & Gries HM (1994) Non-invasive blood glucose sensors based on near-infrared spectroscopy. Artificial Organs 18: 439-447.
35. Marbach R, Koschinsky TH, Gries HM & Heise HM (1993) Non-invasive glucose assay by near –infrared diffuse reflectance spectroscopy of the human inner lip. Applied Spectroscopy. 47: 875-881.
36. Heise HM & Marbach R (1994) effect of data pre-treatment on the non-invasive blood mea-surement by diffuse reflectance near-IR spectroscopy. SPIE Proceedings 2089: 114-115.
37. Jagemann KU, Fischbacher C, Danzer K, Muller UA & Mertes B (1995) Application near infrared spectroscopy for non-invasive determination of blood /tissue glucose using neural network. Zeitschrift für Physikalische Chemie 191S: 179-190.
38. Fischbacher C, Jagemann KU, Danzer K, Muller UA, Papenkrodt L & Schuler J (1997) Enhancing calibration models for non-invasive near-infrared spectroscopic blood glucose determinations. Fresenius Journal of Analysis Chemistry 359: 78-82.
39. Muller UA, Mertes B, Fischbacher C, Jagemann KU & Danzer K (1997) Non-invasive blood glucose monitoring by means of new infrared spectroscopic methods for improving the reliability of the calibration models. International Journal of Artificial Organs 20: 285-290.
40. Kienle A, Lilge L, Patterson MS, Hibst R, Steiner R & Wilson BC (1996) Spatiallly resolved absolute diffuse reflectance measurements for noninvasive determination of optical scattering and absorption coefficients of biological tissue. Applied Optics 35: 2304-2314.

41. Farrell T, Patterson M & Wilson B (1992) A diffusion theory model for the non-invasive determination of tissue optical properties in-vivo. Medical physics 19: 879-888.

42. Maier JS, Walker SA, Fantini S, Franceschini MA & Gratton E (1994) Possible correlation between blood glucose concentration and the reduced scattering coefficient of tissue in the near infrared. Optics Letters 19(24): 2062-2064.

43. Kohl M, Cope M, Essenpreis M and Böcker D (1994) Influence of glucose concentration on light scattering in tissue-simulating phantoms. Optics Letters 19(24): 2170-2172.

44. Bruulsema JT, Hayward JE, Farrell TJ, Patterson MS, Heinemann L & Berger M (1997) Correlation between blood glucose concentration in diabetics and noninvasively measured tissue optical scattering coefficient. Optics Letters 22(3): 190-192.

45. Heinemann L, Schmelzeisen-Redeker G, on behalf of the Non-invasive Task Force (1998) Non-invasive continuous glucose monitoring in type I diabetic patients with optical glucose sensors. Diabetologia 41: 848-854.

46. Heinemann L, Krämer U, Klötzer H-M, Hein M, Volz D, Hermann M, Heise T & Rave K (2000) Noninvasive glucose measurement by monitoring of scattering coefficient during oral glucose tolerance tests. Diabetes Technology & Therapeutics 2(2): 211-220.

47. Patterson M, Moulton JD, Wilson B, Berndt KW & Lakowicz JR (1991) Frequency-domain reflectance for the determination of the scattering and absorption properties of tissue. Applied Optics 30: 4474-4476

48. Fishkin JB & Gratton E (1993) Propagation of photon density wave in strongly scattering media containing an absorbing semi-infinite plane boundedly a straight edge. Journal of Optical Society of America A10: 127-140.

49. Fantini S, Franceschini MA, Fishkin JB, Barbieri B & Gratton E (1994) Quantitative determi nation of the absorption spectra of chromophones in strongly scattering media: a light-emitting-diode based techniques. Applied Optics 33: 5204-5213.

50. Rabinovitch B, March WF & Adams RL (1982) Noninvasive glucose monitoring of the aqueous humour of the eye. Diabetes Care 5: 254-265.

51. Coté GL, Fox MD & Northrup RB (1992) Noninvasive optical glucose sensing using a true phase measurement technique. IEEE Transaction of Biomedical Engineering 39(7): 752-756.

52. Pohjola S (1966) The glucose content of the aqueous humor in man. Acta Ophthalmologica Supplementum 88: 11-80.

53. Chou C, Han CY, Kuo WC, Huang YC, Feng CM & Shyu JC (1998) Noninvasive glucose monitoring in vivo with an optical heterodyne polarimeter. Applied Optics 37(16): 3553-3557.

54. Cough DA (1982) the composition and optical rotary dispersion of bovine aqueous humor. Diebetes Care 5: 266-270.

55. Coté GL & Cameron BD (1997) Noninvasive polarimetric measurement of glucose in cell culture media. Journal of Biomedical Optics 2(3): 275-281.

56. Berger AJ, Wang Y & Feld MS (1996) Rapid, non-invasive concentration measurements of aqueous biological analytes by near infrared Raman spectroscopy. Applied Optics 35: 209-212.

57. Wicksted JP, Erkens RJ, Motamedi M & March WF (1997) Raman spectroscopy studies of metabolic concentrations in aqueous solution and in aqueous humor species. Applied Spectroscopy 49: 987-993.

58. Goetz MJ, Cote GL, Erkens RJ, March WF & motamedi M (1995) Application of multivariate technique to Raman spectra for quantification of body chemicals. IEEE transaction of Biomedical Engineering 42: 728-731.

59. Dou X, Yamaguchi Y, Yamamato H, Harumi H & Ozaki Y (1996) Biological applications of anti-Stokes Raman spectroscopy: quantitative analysis of glucose in plasma and serum by a highly sensitive multichannel Raman spectrometer. Applied Spectroscopy 50: 1301-1306.

60. Tarr RV & Steffes PG (1998) The non-invasive measure of D-glucose in ocular aqueous humor using stimulated Raman spectroscopy. IEEE Laser Electro-Optics Society Newsletter 12(2): 22-27.

61. Berger AJ, Koo TW, Itzkan I, Horowitz G & Feld MS (1999) Multicomponent blood analysis by near-infrared Raman spectroscopy. Applied Optics 38(13): 2916-2926.

62. Schmitt JM (1999) Optical coherence tomography (OCT): a review. IEEE Journal of Selected

Topics in Quantum Electronics 5(4): 1205-1215.

63. Huang D, Swanson EA, Lin CP, Schuman JS, Stinson WG, Chang W, Hee MR, Flotte T, Gregory K, Puliafito CA & Fujimoto JG (1991) Optical coherence tomography. Science 254: 1178-1181.

64. Larin K, Larina I, Motamedi M, Gelikonov Y, Kuranov R & Esenaliev R (2001) Potential application of optical coherence tomography for non-invasive monitoring of glucose concentration. Proceedings of SPIE 4263: 83-90.

65. Klonoff DC, Braig JR, Sterling BB, Kramer C, Goldberger DS & Trebino Y (1998) Mid-infrared spectroscopy for non-invasive blood glucose monitoring. IEEE Laser Electro-Optics Society Newsletter 12(2): 13-14.

66. Sodickson LA & Block MJ (1994) Kromoscopic analysis: a possible alternative to spectro-scopic analysis for non-invasive measurements. Clinical Chemistry 40: 1838-1844.

67. Sodickson LA (1997) Improvements in multivariate analysis via kromoscopic measurements. Spectroscopy 12: 13-24.

68. Misner MW & Block MJ (1997) The raw data of kromoscopic analysis. Spectroscopy 12: 20-21.

69. Li L & Walt DR (1995) Dual-analyte fiber-optic sensor for the simultaneous and continuous measurement of glucose and oxygen. Analytical Chemistry 67: 3746-3753.

70. Gunsingham H, Tan CH and Seow JKL (1990) Fiber-optic glucose sensor with electrochemical generation of indicator reagent. Analytical Chemistry 62: 755-759.

71. Abdel-Latif MS and Guilbault GG (1988) Fiber-optic sensor for the determination of glucose using micellar enhanced chemiluminescence of the peroxylate reaction. Analytical Chemistry 60: 2671-2674.

72. Schultz JS, Mansouri S & Goldstein IJ (1982) Affinity sensor: A new technique for developing implantable sensors fro glucose and other metabolites. Diabetes Care 5: 245-253.

73. Ballerstadt R & Schultz JS (1997) Competitive-binding assay method based on fluorescence quenching of ligands held in close proximity by a multivalent receptor. Analytical Chemistry Acta 345: 203-212.

74. Mackenzie HA, Christison GB, Hodgson P & Blanc D (1993) A laser photoacoustic sensor for analyte detection in aqueous systems. Sensors and Actuators B 11: 213-220.

75. Quan KM, Christison GB, MacKenzie HA & Hodgson P (1993) Glucose determination by a pulsed photoacoustic technique: an experimental study using a gelatin-based tissue phantom. Physics in Medicine and Biology 38: 1911-1922.

76. Christison GB & MacKenzie HA (1993) Laser photoacoustic determination of physiological glucose concentrations in human whole blood. Medical and Biological Engineering and Computing 31: 248-290.

77. Duncan A, Hannigan J, Freeborn SS, Rae PWH, Mclver B, Greig F, Johnston EM, Einnie DT & MacKenzie HA (1995) A portable non-invasive blood glucose monitor. Transducers'95, Eurosensors IX: 455-458.

78. (1996) Laser arrays measure blood glucose levels. Opto & Laser Europe 32: 31-32.

79. Bednov AA, Karabutov AA, Savateeva EV, March WF & Oraevsky AA (2000) Monitoring glucose in vivo by measuring laser-induced acoustic profiles. Proceedings of SPIE 3916: 9-18.

80. Hu CL (1969) Spherical model of an acoustic wave generated by rapid laser heating in a liquid. The Journal of the Acoustic Society of America 46: 728-736.

81. Asshauer T, Rink K & Delacrétaz G (1994) Acoustic transient generation by holmium-laser-induced cavitation bubbles. Journal of Applied Physics 76: 5007-5013.

82. Sigrist MW (1986) Laser generation of acoustic waves in liquids and gases, Journal of Applied Physics 60(7): R83-121.

83. Sigrist MW & Kneubuhl FK (1978) Laser-generated stress waves in liquids. The Journal of the Acoustic Society of America 64: 1652-1663.

84. Brewer RG & Rieckhoff KE (1964) Stimulated Brillouin scattering in liquids. Physical Review Letters 13(11): 334-336.

85. Emmony DC (1985) Interaction of IR laser radiation with liquids. Infrared Phys. 25: 133-139.

86. Hutchins DA (1986) Mechanisms of pulsed photoacoustic generation. Canadian Journal of

Physics 64: 1247-1264.

87. Tam AC (1986) Applications of photoacoustic sensing techniques. Reviews of Modern Physics, 58(2): 381-431.

88. Patel CKN & Tam AC (1981) Pulsed optoacoustic spectroscopy of condensed matter. Reviews of Modern Physics 53(3): 517-550.

89. Park SM, Khan MI, Cheng HZ & Diebold GJ (1991) Photoacoustic effect in strongly absorbing fluids. Ultrasonics, 29: 63-67.

90. Lai M & Young K (1982) Theory of the pulsed photoacoustic technique. Journal of Acoustic Society of America 72: 2000-2007.

91. Hoelen CGA, de Mul FFM & Greve J (1995) Non-destructive photoacoustic subsurface tissue imaging: a feasibility study. Proceedings of SPIE 2628: 308-318.

92. Diebold GJ & Sun T (1994) Properties of photoacoustic waves in one, two, and three dimensions. Acustica 80:339-351.

93. Helander P & Lundström I (980) Light scattering effects in photoacoustic spectroscopy. Journal of Applied Physics 51(7): 3841-3847.

94. Helander P (1983) theoretical aspects of photoacoustic spectroscopy with light scattering samples. Journal of Applied Physics 54(6): 3410-3414.

95. Yasa ZA, Jackson WB & Amer NM (1982) Photothermal spectroscopy of scattering media. Applied Optics 21(1): 21-31.

96. Karabutov AA, Pelivanov IM, Podymova NB & Skipetrov SE (1999) Determination of the optical characteristics of turbid media by the laser optoacoustic method. Quantum Electronics 29: 1054-1059.

97. Goldsmith LA (1991) Physiology, Biochemistry and Molecular Biology of the Skin. 2nd edition, Oxford University Press.

98. http://www.education.eth.net/enrich/human_body/jrcoll_gk14.htm

99. Jacques SL (1996) Origins of tissue optical properties in the UVA, visible and NIR regions. OSA TOPS on advances in optical imaging and photon migration 2: 364-371.

100. Graaff R, Dassel ACM, Koelink MH, de Mul FFM, Aarnoudse JG & Zijlstra WG (1993) Optical properties of human dermis in vitro and in vivo. Applied Optics 32: 435 - 447.

101. Matcher SJ, Cope M & Delpy DT (1997) Invivo measurements of the wavelength dependence of tissue-scattering coefficients between 760 and 900 nm measured with time-resolved spectroscopy. Applied Optics 36: 386-396.

102. Saidi IS, Jacques SL & Tittle FK (1995) Mie and Rayleigh modelling of visible-light scattering in neonatal skin. Applied Optics 34: 7410-7418.

103. Maurice MD (1957) The structure and transparency of the cornea. The Journal of Physiology 136: 23-286.

104. Duck FA (1990) Physical Properties of Tissue: a Comprehensive Reference Book. Academic Press Inc., San Diego.

105. Oraevsky AA, Esenaliev R, Jacques SL, Thomsen S & Tittel FK (1995) Lateral and z-axial resolution in laser optoacoustic imaging with ultrasonic transducers. Proceedings of SPIE 2389: 198-208.

106. Oraevsky AA, Jacques SL & Tittle FK (1997) Measurement of tissue optical properties by time-resolved detection of laser-induced transient stress. Applied Optics 36: 402-415.

107. Hill CR (1986) Physical Principles of Medical Ultrasonics. Chichester: Ellis Horwood.

108. Priezzhev AV (2001) Biomedical diagnostics and instrumentation. InfoTech Oulu Workshop 2001, Oulu, Finland.

109. Roggan A, Friebel M, Dörschel K, Hahn A & Müller G (1999) Optical properties of circulating human blood in the wavelength range 400-2500 nm. Journal of Biomedical Optics 4: 36-46.

110. Welch AJ, Yoon G & van Gemert MCJ (1987) Practical model for light distribution in laser-irradiated tissue. Laser in Surgery and Medicine 6: 488-493.

111. Jacques SL (1997) Tissue Optics Short Course Notes. SPIE's Photonics West, San Jose.

112. Van Gemert MJC, Jacques SL, Sterenborg HJCM and Star WM (1989) Skin optics. IEEE Transactions on Biomedical Engineering 36: 1146-1154.

113. Jacques SL (1995) Tissue fluorescence. Proceedings of SPIE 2371: 2-13

114. Tuchin V (2000) Tissue Optics: light scattering methods and instruments for medical diagnosis. SPIE Press.

115. Wang LH & Jacques SL (1992) Monte Carlo modelling of light transport in multi-layered tissue in standard C, University of Texas M.D. Anderson Cancer Center.

116. Silk MG (1984) Ultrasonic Transducers for Nondestructive Testing. Adam Hilger Ltd., Bristol BS1 6NX.

117. Terzic M & Sigrist MW (1984) Diffraction characteristics of laser-induced acoustic waves in liquids. Journal of Applied Physics 56: 93-95.

118. Sullivan B & Tam AC (1984) Profile of laser-produced acoustic pulse in a liquid. Journal of Acoustic Society of America 75: 437-441.

119. Kuo CY, Vieira MMF & Patel CKN (1984) Transient optoacoustic pulse generation and detection. Journal of Applied Physics 55: 3333-3336.

120. Tam AC & Patel CKN (1979) Optical absorption of light and heavy water by laser optoacoustic spectroscopy. Applied Physics 18: 3348-3357.

121. Tenhunen J, Kopola H & Myllylä R (1998) Non-invassive glucose measurement based on selective near infrared absorption: requirements on instrumentation and special range. Measurement 24: 173-177.

122. Zemansky MW (1968) Heat and Thermodynamics: an Intermediate Textbook. 5th edition, McGraw-hill Kogakusha, Tokyo.

123. Beard PC & Mills TH (1997) Characterization of post mortem arterial tissue using time-resolved photoacoustic spectroscopy at 436, 461 and 532 nm. Physics in Medicine and Biology 42: 177-198.

124. Hoelen CGA & de Mul FFM (1998) Imaging of cutaneaous blood vessels using photoacoustic tissue scanning (PATS). Proceedings of SPIE 3566: 134-142.

125. Hodgson P, Quan KM, MacKenzie HA, Freeborn SS, Hannigan J, Johnston EM, Greig F & Binnie TD (1995) Application of pulsed laser photoacoustic sensors in monitoring oil contamination in water. Sensors and Actuators B29: 339-344.

126. Agrawal GP (1989) Nonlinear Fiber Optics. Academic Press, London.

127. Smith RG (1972) Optical power handing capacity of low loss optical fibers as determined by stimulated Raman and Brillouin scattering. Applied Optics 11: 2489-2494.

128. Stolen RH & Ippen EP (1973) Raman gain in glass optical waveguides. Applied Physics Letters 22: 276-278.

129. Hannigan J, Greig F, Freeborn SS & MacKenzie HA (1999) A pulsed photocaoustic system for the spectroscopy and monitoring of hydrocarbon liquids using stimulated Raman scattering in a silica fibre as a near-infrared source. Measurement Science and Technology 10: 93-99.

130. Svelto O (1998) Principles of Lasers. Plenum Press, New York.

131. MacKenzie HA, Ashton HS, Spiers S, Shen Y, Freeborn SS, Hannigan J, Lindberg J & Rae P (1999) Advances in photoacoustic noninvasive glucose testing. Clinical Chemistry 45: 1587-1595.

132. Shen Y, Lu Z, Spiers S, MacKenzie HA, Ashton HS, Hannigan J, Freeborn SS, & Lindberg J (2000) Measurement of the optical absorption coefficient of a liquid by use of a time-resolved photoacoustic technique. Applied Optics 39: 4007-4012.

133. Köstli KP, Frenz M & Weber HP (2000) Optoacoustic infrared spectroscopy of soft tissue. Journal of Applied Physics 88: 1632-1637.

134. Hodgson P (1994) The detection of oil in water by near infrared pulsed photoacoustic spectroscopy. Herlot-Watt University, DX180532.

135. Zhan X, Kauppi E & Halonen L (1992) High-resolution photoacoustic Ti:sapphire/dye ring laser spectrometer. Review of Scientific Instruments 63: 5546-5551.

136. Fu SW, Wu ZS, Zhang XR, Zhang SY, Zhang Z & Chen HL (1995) Ultrasonic transducer study for photoacoustic calorimetry. IEEE 1995 Ultrasonics Symposium Proceedings, 859-862.

137. Monchalin J-P (1986) Optical detection of ultrasound, IEEE Transaction on Ultrasonics, Ferroelectrics and Frequency Control 33: 485-499

111

138. March DM (1973) Methods of visualizing ultrasound. Research Techniques in Non-destructive Testing 2: 281-327.
139. Fleury PA (1970) Light scattering as a probe of phonons and other excitations. Physical Acoustics 6:1-64.
140. Paltauf G & Schmidt-Kloiber H (1997) Measurement of laser-induced acoustic waves with a calibrated optical transducer. Journal of Applied Physics 82: 1525-1531.
141. Paltauf G, Schmidt-Kloiber H & Guss H (1996) Optical detection of laser-induced stress waves for measurement of the light distribution in living tissue. Proceedings of SPIE 2923: 127-135.
142. Calder CA & Wilcox WW (1980) Noncontact material testing using laser energy deposition and interferometry. Materials Evaluation 38: 86-91.
143. Hutchins DA & Nadeau F (1983) Non-contact ultrasonic waveforms in metals using laser generation and interferometric detection. IEEE 1983 Ultrasonics Symposium Proceedings, 1175-1177.
144. Suemune I, Yamamoto H & Yamanishi M (1985) Noncontact photoacoustic measurement of semiconductors with Michelson interferometry. Journal of Applied Physics 58: 615-617.
145. Hoyes JB, Shan Q & Dewhurst RJ (1991) A non-contact scanning system for laser ultrasonic defect imaging. Measurement Science and Technology 2: 628-634.
146. Jacques SL, Andersen PE, Hanson SG & Lindvold LR (1998) Non-contact detection of laser-induced acoustic waves from buried absorbing objects using a dual-beam common-path interferometer. Proceedings of SPIE 3254: 307-318.
147. Bead PC, Hurrell A & Mills TN (2000) An optical detection system for biomedical photo-acoustic imaging. Proceedings of SPIE 3916: 100-109.
148. Beard PC, Perennes F & Mills TN (1999) Transduction mechanisms of the Fabry Perot polymer film sensing concept for wide band ultrasonic detection. IEEE Transactions on Ultrasonics, Ferroelectrics and Frequency Control 46: 1575-1582.
149. Bead PC, Hurrell A & Mills TN (2000) The characterisation of a polymer film optical fiber hydrophone for the measurement of ultrasound fields for use in the range 1-20 MHz: a comparison with PVDF needle and membrane hydrophone. IEEE Transactions on Ultrasonics, Ferroelectrics and Frequency control 47: 256-264.
150. Ahola O (1999) Licentiate thesis, University of Oulu, Oulu, Finland.
151. Antila P (1973) Occurrence of certain trace elements in cow's milk. Helsinki, Finland.
152. Liu Y, Hering P and Scully MO, (1992) An integrated optical sensor for measuring glucose concentration. Applied Physics B54: 18-23.
153. Weast RC (1989) CRC Handbook of Chemistry and Physics. 70th edition, CRC, Cleveland, Ohio.
154. Knüttel A & Boehlau-Godau M (2000) Spatially confined and temporally resolved refractive index and scattering evaluation in human skin performed with optical coherence tomography. Journal of Biomedical Optics 5: 83-92.